BIO-INSPIRED LOCOMOTION USING OSCILLATING ELASTIC PLATES

A Dissertation
Presented to
The Academic Faculty

By

Ersan Demirer

In Partial Fulfillment
of the Requirements for the Degree
Doctor of Philosophy in the
George W. Woodruff School of Mechanical Engineering

Georgia Institute of Technology

May 2021

BIO-INSPIRED LOCOMOTION USING OSCILLATING ELASTIC PLATES

Approved by:

Dr. Alexander Alexeev, Advisor
George W. Woodruff School of Mechanical Engineering
Georgia Institute of Technology

Dr. Alper Erturk
George W. Woodruff School of Mechanical Engineering
Georgia Institute of Technology

Dr. David Hu
George W. Woodruff School of Mechanical Engineeringg
Georgia Institute of Technology

Dr. Ramiro Godoy-Diana
Physique et Mécanique des Milieux Hétérogène
École supérieure de physique et de chimie industrielles de la Ville de Paris

Dr. Kai Schneider
Institut de Mathématiques de Marseille
Aix-Marseille Université, France

Date Approved: April 12, 2021

To my parents, Burhan and Candan, my siblings Ceylin and Volkan, and my better half Daniela.

Without you, this work would have not been possible.

ACKNOWLEDGEMENTS

I first want to thank my advisor Dr. Alexander Alexeev, not only for the great opportunity he offered me but even more so for the continuous support throughout these four years. Thank you for creating such a positive work environment where scientific critical thinking can be shared and discussed freely with peers in a spirit of camaraderie. I would also like to thank members of my reading committee, Dr. Alper Erturk, Dr. David Hu, Dr. Ramiro Godoy-Diana and Dr. Kai Schneider for their encouragements and comments which allowed to widen the scope of my work and challenge my views.

In addition, I want to thank all my fellow labmates, Yaro, Nick, Ki Tae, Yueyi, Fatima and Sam. I had a great four years in this lab because of you, thank you for laughing at most of my terrible jokes and distractions and for the help you gave me on an academic and personal level. I would like to thank as well undergraduate research assistants, Fikayo, Royce and fellow collaborators, David, Yu-Cheng, Eetu and Herit. A lot of this work would not have been possible without your support.

Finally, I want to give a special acknowledgement to my family. First and foremost to my parents Burhan and Candan who gave me all the resources and tools to arrive where I am now. My siblings, Ceylin and Volkan, whose support throughout the years has made this complex task much simpler. Finally, I want to particularly thank Daniela, who not only has been my better half and emotional support throughout this whole PhD but also my compass. Had I not met you, I would not have been able to finish this work but more importantly I would not be the person that I am now. Thank you for your unwavering love, patience and support.

TABLE OF CONTENTS

LIST OF TABLES

LIST OF FIGURES

SUMMARY

Fish swimming is characterized by its astonishing versatility: from fast bursts and sharp turns to fast and efficient cruising. By adjusting their flexible body and tail through muscle activation, fish are capable of harnessing various changing flow conditions. Motivated by this adaptability, researchers and engineers have striven to apply the same principles to their robotic fish designs. Robotic fish have historically started as intricate designs comprised of complex networks of actuators and relatively rigid surfaces. More recently, simpler swimmers consisting of flexible heaving or pitching plates have emerged. These moving elastic plates represent fish locomotion to a certain level of abstraction. In spite of the apparent simplicity of such bio-inspired swimmers, their motion inherently depends on a complex interplay between the three-dimensional elastic plate motion and the flow of the surrounding viscous fluid.

In this work, we numerically investigate the problem of bio-mimetic locomotion using a fully-coupled three-dimensional fluid-structure interaction computational framework. The bio-inspired propulsor is modeled as a thin elastic plate oscillating in a Newtonian fluid. The computational model consists of the lattice Boltzmann method coupled to either finite differences or the lattice spring method. We systematically explore the impact of several design parameters on the propulsor's swimming performance, including the effects of non-uniform properties, flow regime, aspect and mass ratios as well as the actuation mechanism itself.

We find that the driving mechanism and frequency of the elastic swimmer is a key design parameter. When comparing conventional heaving with more recent muscle-like actuation, we find critical differences in bending patterns. These critical differences in bending patterns in turn are associated with an improved performance of conventional heaving over muscle-like actuation. Although conventional heaving is

found to outperform muscle-like actuation, we find that the swimming performance can be further enhanced by combining novel and conventional. This hybrid actuation strikes a formidable balance between propulsion and energetic performance. Moreover, we demonstrate that the hybrid actuation can easily regulate various swimming metrics as needed in real life *scenarii*.

As illustrated by the diversity of fin mechanical properties observed in nature across species, the thickness, and ultimately the distribution of bending stiffness in the fin, is primordial to generate highly efficient propulsion. Thickness distribution is also a key concept in understanding various types of swimming adopted by different types of aquatic animals. Using arguments based on wave theory, we show that tapered swimmers display particularly advantageous features over a wide range of driving frequencies. Furthermore, we demonstrate that plate metrics known *a priori* accurately allow to estimate the propulsive performance of the swimmer without recurring to computationally intensive simulations. This estimation is achieved with an evolutionary approach based on simple principles such as mating pools, mutations and survival of the fittest.

CHAPTER 1
INTRODUCTION

1.1 Background

Fish are capable of reaching and maintaining efficient and fast swimming under severely changing conditions as well as performing quick turning manoeuvres. To propel, fish pass waves down their elastic body and fins. As a consequence, the motion of individual fins is inherently complex and three-dimensional [1]–[4]. Natural selection and millions of years of evolution have resulted in highly efficient, if not optimal, mechanical systems. This incredible performance has inspired researchers and scientists to incorporate fish-like motion in their designs. Such designs are particularly tailored for autonomous underwater vehicles (AUVs) for which autonomy, and therefore efficiency, is primordial. Sample applications of AUVs include marine exploration, *in-vivo* study of fish populations, remote sensing, among others.

Most fish generate propulsion by bending their body to create a backward-travelling or standing wave extending to their caudal fin. This swimming type is referred to as body and/or caudal fin (BCF) mode. Other types of fish rely on the motion of their median and/or paired fins (MPF) [5]. BCF mode is generally associated to higher swimming velocities while MPF mode results in slower swimming but enhanced manoeuvring. Most fish use the BCF mode for general cruising while MPF mode serves as stabilization and precise manoeuvring. We illustrate the fin nomenclature in figure 1.1. Both BCF and MPF swimming modes can be further sub-categorized into undulating or oscillating swimming modes; however, we will mainly focus on BCF modes. Indeed, when considering bio-mimetic design, the multiple fins involved in the MPF mode result in a significant complexity when compared to the BCF mode. Thus, the

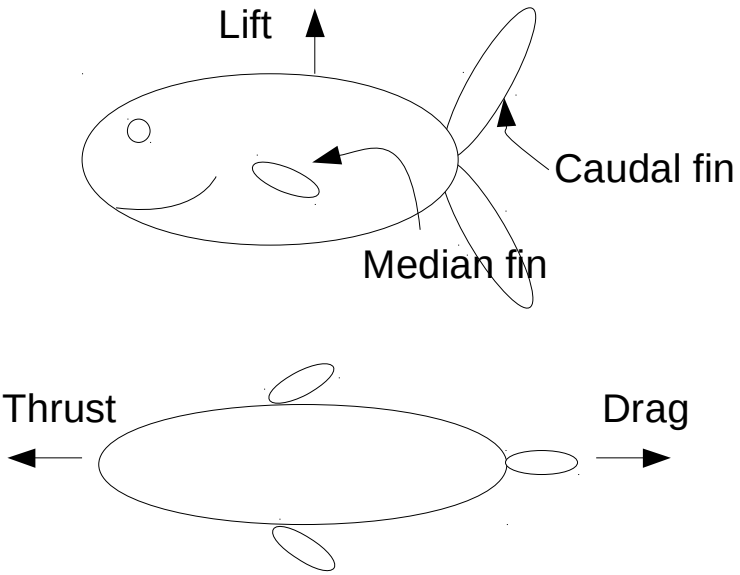

Figure 1.1: Generic fin and force nomenclature.

BCF mode reduces the number of degrees of freedom of the robotic design.

Various types of BCF swimming can be categorized by the extent to which the body is involved in generating the propulsion. On the left-most part of this spectrum as shown in figure 1.2, undulatory BCF is best illustrated by anguilliform types of fish such as eels. In anguilliform swimming, the entire body bends to generate a travelling wave. Directly next to anguilliform mode, subcarangiform and carangiform modes also rely on significant bending of the body to generate a mix of travelling and standing waves to generate thrust. However, the fraction of the body used is reduced when compared to anguilliform mode. On the right-most side of BCF swimming diagram, thunniform and ostraciiform modes are associated with almost rigid bodies and standing waves generated by the caudal fin. Thunniform mode of swimming is particularly characterized by high swimming velocity and efficiency in calm water.

As demonstrated by the thunniform swimming mode, it is necessary to understand the underlying physics of a single fin oscillating in a viscous fluid [6]–[15]. As the fin oscillates in a viscous fluid, its deformation is subjected to inertia, elastic and hydrodynamic forces, resulting in complex dynamic bending patterns. In turn, the

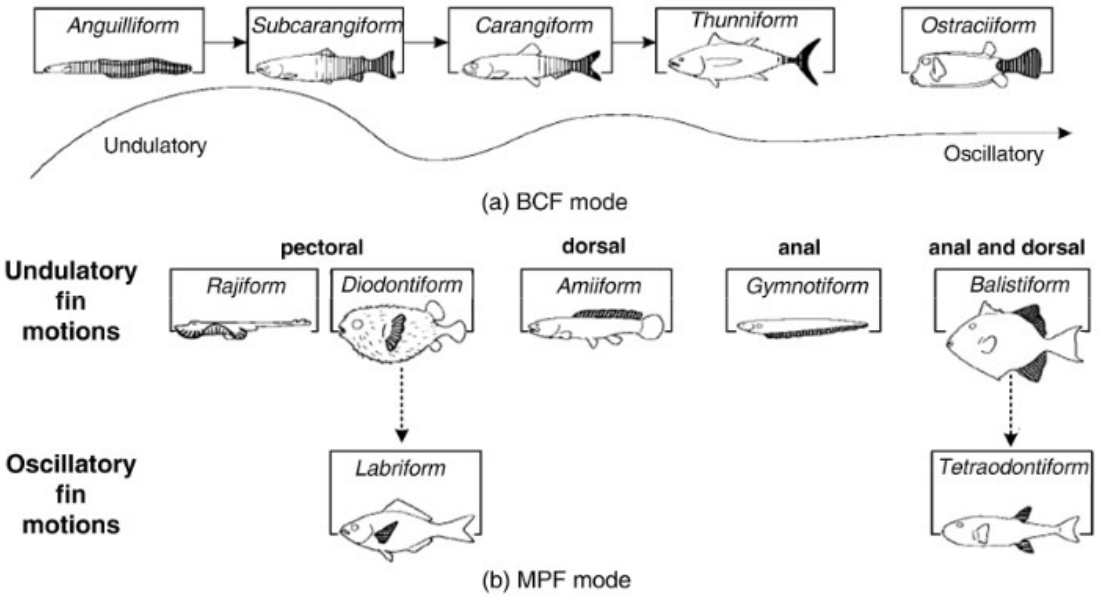

Figure 1.2: Categorization of fish swimming. Adapted from [5]. ©1999 IEEE.

fin imposes its own motion on the surrounding fluid resulting in complex vortex structures. This interplay leads to a challenging coupling between the fin deformation and the unsteady hydrodynamic loading. The fin bending strongly depends on the oscillation frequency and its proximity to the resonance frequencies. At resonance, the fin deformation is amplified which may potentially result in higher swimming performance.

Early designs of bio-inspired robotic fish include passive rigid to moderately elastic caudal fins actuated by a complex set of strings and servomotors [16], [17]. More recent designs successfully incorporated flexibility through sets of linked rigid parts coupled to servomotors [18]–[21]. However, such designs not only lack in manoeuvring and swimming efficiency [12], [13] but also result in high design complexity.

Recently, smart material have been gaining traction for their use in bio-inspired design and particularly their capacity to implement robotic fish designs to higher levels of bio-mimicry without the cumbersome complexity of conventional motor-based designs [14], [15], [22]. Smart materials include, but are not limited to, ionic-

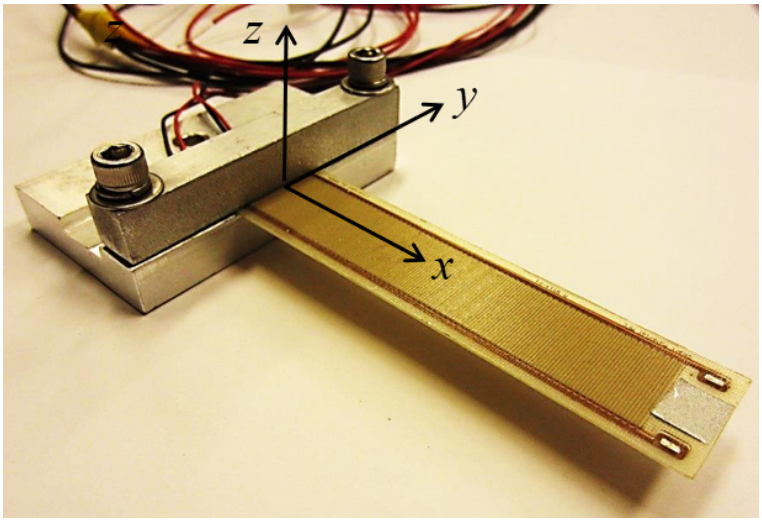

Figure 1.3: Macro-fiber composite material (SSDSL group at Georgia Tech)

polymer metal composites (IPMC) [22]–[26], shape-memory alloys (SMA) [27]–[29], and piezoelectric materials [30]–[32]. Among smart materials, piezoelectric materials have gained increasing interest. In particular, macro-fiber composites (MFC) strike a balance between deformation and actuation levels. Furthermore, MFCs (figure 1.3 tremendously simplify designs as well as offer noiseless operation [33]. Despite their promising features, there is not systematic work on understanding their hydrodynamic performance. Therefore the hydrodynamic regime at which such materials should be used to yield efficient locomotion is yet unclear.

Given the intrinsic complexity of bio-mimetic locomotion, researchers turned to simplified models to investigate the performance of fins oscillating in a fluid. Lighthill [34]–[36] and Wu [37] independently laid out the analytical foundation of elongated and slender body theory. Their work is based on the two-dimensional inviscid flow induced by oscillating beams. Lighthill suggested that the mean thrust generated by a swimmer depends solely on the tip kinematics and mass ratio of the body. More recent work [38], [39] constructs approximate solutions of cantilevered beams oscillating in inviscid fluids. These analytical solutions provide tremendous insight on the hydrodynamic of elastic fins actuated under water. However, viscosity effects

cannot be neglected for fins of moderate sizes. Therefore, it is necessary to rely on experiments and numerical simulations to thoroughly investigate the hydrodynamics of such fins. For instance, Ramananarivo et al. [40] experimentally studied the free swimming of anguilliform swimming and related the swimming mode to the hydrodynamic damping. However, experimental investigations are typically limited by equipment and cost. In turn, numerical simulations are an attractive solution for exploring the wide parameter space of oscillating swimmers and understanding the underlying physics.

Aureli et al. [41] used a two-dimensional numerical model to probe the effects of viscosity on the resonance oscillations of a cantilevered beam. They found that increasing the driving frequency and amplitude results in a vortex shedding which in turn is responsible for non-linear hydrodynamic damping. Moreover, the authors used the results from their parametric study to derive a reduced order model. However, this work is not able to capture three-dimensional vortex shedding which accounts for a significant part of the drag acting on the swimmer. By comparing a numerical model to experimental data, Facci [42] extended Sader's model to three-dimensional fluid-solid coupling for small deformations and relatively low Reynolds number ($Re < 100$). They performed a thorough parametric study on dimensionless numbers such as the Reynolds and Keulegan-Carpenter number as well as the aspect ratio for a cantilevered plate. They found that three-dimensional effects are not negligible for plates of low aspect ratio (wide). This is due to a change in distribution of added mass forces resulting from vortex shedding. Conversely, they found that three-dimensional considerations have very limited impact on the hydrodynamic damping. With this approach, they suggested enhancing the reduced order model developed by Aureli et al. by integrating three-dimensional effects. With the help of experiments and a high Reynolds number model, Alben et al. [9] proved the existence of resonance peaks in the free swimming velocity of an elastic oscillating plate. In addition, their

model predicts that the plate velocity is proportional to the plate length to the power $-1/3$ and plate flexibility to the power $2/15$. Using experiments, Quinn et al. [43] demonstrated that for constrained plates, these resonance peaks in free swimming velocity occur for discrete values of the effective flexibility which is defined as a dimensionless number measuring the ratio of added mass to bending forces. Hoover et al. [44] further confirmed these findings with three-dimensional simulations of free swimming flexible plates.

Borazjani et al. [45] investigated the hydrodynamics of carangiform locomotion by simulating experimentally-measured prescribed kinematics of a three-dimensional mackerel-like body in a viscous fluid. They showed that for this configuration the propulsive efficiency is an increasing function of the Reynolds number. Their work suggested that the topology of the wake is principally a function of the Strouhal number. More recently, Bhalla et al. [46] developed an adaptive grid mathematical framework for the simulation of rigid, deforming or elastic bodies in a Newtonian fluid. They showcase several test cases, including the three-dimensional flow around a knifefish with prescribed kinematics. Representing the fish locomotion through a single fin is a common level of abstractions to probe the fully-coupled hydrodynamics of elastic plates with substantial deformation. Previous work showed that resonance oscillations result in enhanced propulsion as well as demonstrated that elasticity is a key parameter to optimize fin performance. For instance, Dai et al. [47] showed that an elastic plate generates significantly more thrust than a rigid plate at the same Strouhal number. Eloy [48] developed an optimization procedure based on a reduced order model to argue that undulatory swimming is, from an evolutionary stance, a logic consequence of minimizing energy cost. Yeh et al. [49]–[51] used fully-coupled three-dimensional simulations to show that elastic swimmers could be operated at a regime of maximum propulsion near the first natural frequency or maximum efficiency away from the resonance. Moreover, the authors considered the impact of tapered

structures which were shown to outperform fins with uniform thickness in terms of efficiency for a wide range of actuation frequencies.

1.2 Research Objectives

Due to the daunting size of the parameter space, researchers have focused on particular aspects of fish swimming in order to improve the design of existing and future underwater vehicles. While these studies provide tremendous insights for understanding efficient underwater swimming, there is still uncharted territory that is to be explored. For instance, most of aforementioned work focuses on a form of heaving, pitching or combination of the two at the leading edge of the swimmer. Although heaving or pitching is a valuable level of abstraction to represent fish swimming, the diversity of fish locomotion is rather broad. The need to understand other forms of actuation source is particularly valuable due to the development of new smart materials which allow to increase the level of bio-mimicry. As a consequence of their recent development, the impact of resulting kinematics on robotic fish swimming is not fully understood and the literature lacks a systematic investigation on the impact of aforementioned "conventional" actuation methods such as heaving in comparison to the actuation of smart materials such as MFCs.

While fish in nature display anisotropic inhomogeneous fin properties, the majority of previous studies have only considered flexible plates with homogeneous mechanical properties. Conversely, plates with inhomogeneous properties have not yet been systematically studied and specifically their impact on the swimming performance. Furthermore, the relationship between mechanical properties and fish swimming mode remains unclear.

Experimental work is usually limited by the equipment itself and cost. As a consequence, numerical simulations are of particular interest to understand the underlying physics of bio-inpired swimmers. Despite the progress in computational modeling,

the simulation of a three-dimensional fish in a viscous fluid remains a tremendous challenge. A various amount of simplifications are generally used including but not limited to inviscid flow, rigid or quasi-rigid geometry or prescribed body kinematics. Accordingly, the amount of work using fully-coupled three-dimensional numerical simulations in the literature is limited.

This work aims to investigate three different aspects of bio-inspired locomotion applicable to robotic swimmers : (1) to systematically quantify how smart material based actuation performs versus conventional external actuation and their effect on the hydrodynamics of elastic plates; (2) to probe the effects of combining internal and external actuation patterns; (3) to understand the effects of non-uniform mechanical properties on the swimming mode and its impact on propulsion performance. To answer these questions, we develop and validate a fully-coupled three-dimensional fluid-structure interaction (FSI) model of an elastic plate plunging in a viscous fluid. The fluid solver is based on the lattice Boltzmann method (LBM) while the solid solver uses finite differences (FD) or the lattice spring method (LSM). The solvers are fully-coupled through dynamic and kinematic boundary conditions at the interface.

1.3 Thesis Structure

The rest of this dissertation is organized as follows. Chapter 2 describes the FSI model as well as presents validation for several test cases. Chapter 3 presents the results of the systematic investigation of an internal versus an external actuation method. In chapter 4, we present the results of combining previously opposed actuation methods. Chapter 5 describes the impact of non-uniform mechanical properties on the swimming performance. Finally, chapter 6 summarizes the results laid out in this work as well as discusses the outlook of this research.

CHAPTER 2

FLUID–STRUCTURE INTERACTION (FSI) MODEL

Our computational model is based on a fully coupled solver simulating the three-dimensional hydrodynamics of an elastic plate submerged into an incompressible Newtonian fluid. On the fluid side, we capture the mechanics using the Lattice–Boltzmann Method (LBM), while the solid mechanics is solved using a finite differences (FD) or lattice spring method (LSM) formulation. LBM and FD/LSM are fully coupled at the fluid-solid boundaries using a two-way coupling procedure [52], [53]. Our coupling procedure is highly parallelizable, scalable, and time efficient when compared to traditional FSI procedures. While LBM does not require slow matrix inversions, FD and LSM allow simple and elegant modeling of complex solid behavior.

2.1 Lattice–Boltzmann Method (LBM)

The lattice Boltzmann method is based on the solution of the discrete Boltzmann equation. The computational domain is discretized using a cubic lattice of equally spaced nodes. At each node, the flow is characterized by a velocity distribution function $f_i(\underline{r}, t)$ that represents the density of fluid particles at position $\underline{r}$ propagating at velocity $\underline{c}$ in the direction i at time t. The macroscopic quantities characterizing the flow, such as the density ρ, momentum $\rho\underline{u}$ and stress $\underline{\underline{\Pi}}$ are retrieved by taking moments of the distribution functions given by

$$\rho = \sum_i f_i \ , \ \rho\underline{u} = \sum_i f_i \underline{c_i} \ , \ \underline{\underline{\Pi}} = \sum_i f_i \underline{c_i} \otimes \underline{c_i} \ . \tag{2.1}$$

We use D3Q19 lattices that maintains 19 directions of the distribution functions in three spatial dimensions. The time evolution of the distribution functions is computed

by integrating the discrete Boltzmann equation

$$f_i(\underline{r} + \underline{c_i}\Delta t, t + \Delta t) = f_i(\underline{r}, t) + \Omega_i \ . \tag{2.2}$$

Here Ω_i is the collision operator and represents the change in f_i due to instantaneous fluid "particle" collisions at each node. We use a dual relaxation time collision operator [54] which increases the accuracy at the fluid-solid boundaries and stability for a larger range of Reynolds numbers compared to single relaxation time collision operators. The post-collision distribution function is computed as

$$f_i(\underline{r}, t) + \Omega_i = a_i \left[\rho + \frac{\rho \underline{u} \cdot \underline{c_i}}{c_s^2} + \frac{\left(\rho \underline{u} \otimes \underline{u} + \underline{\underline{\Pi}}^*_{neq} \right) : \left(\underline{c_i} \otimes \underline{c_i} - c_s^2 \underline{\underline{I}} \right)}{2 c_s^4} \right] \ . \tag{2.3}$$

Here $c_s = \frac{\Delta x}{\sqrt{3}\Delta t}$ is the speed of sound and the non-equilibrium momentum flux $\underline{\underline{\Pi}}^*_{neq}$ is given by

$$\underline{\underline{\Pi}}^*_{neq} = \underbrace{(1+\lambda)\, \underline{\underline{\Pi}}^d_{neq}}_{\text{deviatoric}} + \underbrace{\frac{1}{3}(1+\lambda_\nu) \left(\underline{\underline{\Pi}}_{neq} : \underline{\underline{I}} \right) \underline{\underline{I}}}_{\text{spherical}} \tag{2.4}$$

where $\underline{\underline{\Pi}}^d_{neq}$ is the traceless part of $\underline{\underline{\Pi}} - \underline{\underline{\Pi}}_{eq}$ and λ and λ_v are the two relaxation parameters in the LBM closure. They relate to the shear and bulk viscosities respectively as

$$\mu = -\rho c_s^2 \Delta t \left(\frac{1}{\lambda} + \frac{1}{2} \right) \tag{2.5}$$

$$\zeta = -\rho c_s^2 \Delta t \left(\frac{2}{3\lambda_\nu} + \frac{1}{3} \right) \ . \tag{2.6}$$

Furthermore the weights a_i depend on the distribution velocity $|\underline{c_i}|$ as

$$a_i = \begin{cases} 1/3, & \text{if } |\underline{c_i}| = 0 \\ 1/18, & \text{if } |\underline{c_i}| = 1 \\ 1/36, & \text{if } |\underline{c_i}| = \sqrt{2} \end{cases} . \tag{2.7}$$

The LBM algorithm elegantly consists in two steps : collision and advection.

1. At each lattice node we compute the post-collision distribution function;

2. Based on the respective velocity direction $\underline{c_i}$ we propagate the function to the neighboring lattice node.

2.1.1 Turbulence modeling

In order to model the flow accurately at higher Re at reasonable computational cost, we adopt a large eddy simulation (LES) approach. In the LES approach, eddy motions of fluid with length scales bigger than the computational grid are computed while subgrid scales are modeled. One of the most popular subgrid model is the Smagorinsky subgrid scale (SGS) model. The filtered LBM equation for LES is written as

$$\overline{f}_i(\underline{r} + \underline{c_i}\Delta t, t + \Delta t) = \overline{f}_i(\underline{r}, t) + \overline{\Omega}_i \tag{2.8}$$

where $\bar{\cdot}$ indicates grid filtering. The effect of the subgrid scales is captured by an eddy viscosity

$$\nu_t = C\overline{\Delta}^2|\underline{\overline{S}}| \tag{2.9}$$

where $\overline{S}_{ij} = \frac{1}{2}\left(\frac{\partial \overline{u}_i}{\partial x_j} + \frac{\partial \overline{u}_j}{\partial x_i}\right)$ is the strain rate tensor, $|\underline{\overline{S}}| = \sqrt{2\overline{S}_{ij}\overline{S}_{ij}}$, $\Delta = \Delta_x = \Delta_y = \Delta_z$ is the filter width equal to the lattice spacing and C is the Smagorinsky constant. The filtered strain rate tensor can be evaluated by taking finite differences of the

velocity field or from non-equilibrium moments [55]. It relates to the non-equilibrium stress tensor $\overline{\Pi}_{ij,neq}$ as

$$\overline{S}_{ij} = -\frac{1}{2\rho c_s^2 \tau_w} \overline{\Pi}_{ij,neq} \tag{2.10}$$

$$\overline{\Pi}_{ij,neq} = \sum_k c_{ki} c_{kj} \left(\overline{f}_k^{\text{neq}} \right) \tag{2.11}$$

where $\tau_w = \frac{1}{2} + \frac{1}{c_s^2 \Delta t} (\nu_t + \nu_0)$ is the total relaxation time, ν_0 and ν_t are the molecular and turbulent viscosity respectively. By combining these equations we can compute τ_w as

$$\tau_w = \frac{1}{2} + \frac{1}{c_s^2 \Delta t} \left[\nu_0 + \frac{c_s^2}{2} \left(\sqrt{\tau_0^2 \Delta t^2 + \frac{2\Delta t C^2 \Delta^2 |\overline{\overline{\Pi}}_{neq}|}{c_s^4}} \right) - \tau_0 \Delta t \right] \tag{2.12}$$

2.2 Thin Plate Model

2.2.1 Finite Differences (FD)

2.2.1.1 Isotropic Homogeneous Plate

In this subsection we consider an istropic homogeneous plate. The plate elastic deformation is modeled using the Kirchhoff-Love assumptions [56] with the x, y, and z components of plate displacement respectively defined as

$$\begin{aligned} u(x,y,z) &= -z \frac{\partial w}{\partial x}(x,y) \ , \\ v(x,y,z) &= -z \frac{\partial w}{\partial y}(x,y) \ , \\ w(x,y,z) &= w(x,y,0) = w(x,y) \ . \end{aligned}$$

For a differential plate element of size dx and dy, the forces and moments acting on the element are given by

$$\frac{\partial M_x}{\partial x} + \frac{\partial M_{xy}}{\partial y} = Q_x \ , \tag{2.13}$$

$$\frac{\partial M_{xy}}{\partial x} + \frac{\partial M_y}{\partial y} = Q_y \ , \tag{2.14}$$

$$\frac{\partial Q_x}{\partial x} + \frac{\partial Q_y}{\partial y} + q(x,y,t) = \rho_s h \frac{\partial^2 w}{\partial t^2} \ . \tag{2.15}$$

Here, Q_x, Q_y and M_x, M_y are the shear forces and bending moments in the respective direction, M_{xy} is the twisting moment and q is the transverse load acting on the plate. For an isotropic material, the bending moments are given by

$$M_x = -D\left(\frac{\partial^2 w}{\partial x^2} + \nu \frac{\partial^2 w}{\partial y^2}\right) \ , \tag{2.16}$$

$$M_y = -D\left(\frac{\partial^2 w}{\partial y^2} + \nu \frac{\partial^2 w}{\partial x^2}\right) \ , \tag{2.17}$$

$$M_{xy} = -D(1-\nu)\frac{\partial^2 w}{\partial x \partial y} \ . \tag{2.18}$$

where $D = \frac{Eh^3}{12(1-\nu^2)}$ is the bending stiffness of the plate, which is constant considering an isotropic plate with constant thickness. By combining Eqs. 2.13–2.18, we obtain an equation for the transverse displacement of the elastic plate

$$\rho_s h \frac{\partial^2 w}{\partial t^2} = q(x,y,t) + \left(N_x \frac{\partial^2 w}{\partial x^2} + N_y \frac{\partial^2 w}{\partial y^2} + N_{xy} \frac{\partial^2 w}{\partial x \partial y}\right) - D\nabla^4 w - \gamma \nabla^4 \frac{\partial w}{\partial t} \ . \tag{2.19}$$

Here, ∇^4 is the bilaplacian operator, $\gamma \geq 0$ is the Kelvin-Voigt damping coefficient N_x, N_y, N_{xy} are the in-plane shearing forces and ν is the Poisson ratio. In discretized form (with $\gamma = 0$), with explicit central finite differences in time and space, equation

2.19 yields

$$\begin{aligned}\frac{\rho h}{\Delta t^2}\left(w_{i,j}^{n+1}-2w_{i,j}^{n}+w_{i,j}^{n-1}\right) = q_{i,j}^{n} &+ w_{i+2,j}^{n}\left(\frac{-D}{\Delta x^4}\right)+w_{i-2,j}^{n}\left(\frac{-D}{\Delta x^4}\right)+w_{i,j+2}^{n}\left(\frac{-D}{\Delta y^4}\right)+w_{i,j-2}^{n}\left(\frac{-D}{\Delta y^4}\right)\\ &+w_{i+1,j+1}^{n}\left(-\frac{2D}{\Delta x^2\Delta y^2}+\frac{N_{xyi,j}^{n}}{4\Delta x\Delta y}\right)+w_{i-1,j+1}^{n}\left(-\frac{2D}{\Delta x^2\Delta y^2}-\frac{N_{xyi,j}^{n}}{4\Delta x\Delta y}\right)\\ &+w_{i+1,j-1}^{n}\left(-\frac{2D}{\Delta x^2\Delta y^2}-\frac{N_{xyi,j}^{n}}{4\Delta x\Delta y}\right)+w_{i-1,j-1}^{n}\left(-\frac{2D}{\Delta x^2\Delta y^2}+\frac{N_{xyi,j}^{n}}{4\Delta x\Delta y}\right)\\ &+w_{i,j}^{n}\left[-D\left(\frac{6}{\Delta x^4}+\frac{8}{\Delta x^2\Delta y^2}+\frac{6}{\Delta y^4}\right)-\frac{2N_{xi,j}^{n}}{\Delta x^2}-\frac{2N_{yi,j}^{n}}{\Delta y^2}\right]\\ &+w_{i+1,j}^{n}\left[4D\left(\frac{1}{\Delta x^4}+\frac{1}{\Delta x^2\Delta y^2}\right)+\frac{N_{xi,j}^{n}}{\Delta x^2}\right]\\ &+w_{i-1,j}^{n}\left[4D\left(\frac{1}{\Delta x^4}+\frac{1}{\Delta x^2\Delta y^2}\right)+\frac{N_{xi,j}^{n}}{\Delta x^2}\right]\\ &+w_{i,j+1}^{n}\left[4D\left(\frac{1}{\Delta y^4}+\frac{1}{\Delta x^2\Delta y^2}\right)+\frac{N_{yi,j}^{n}}{\Delta y^2}\right]\\ &+w_{i,j-1}^{n}\left[4D\left(\frac{1}{\Delta y^4}+\frac{1}{\Delta x^2\Delta y^2}\right)+\frac{N_{yi,j}^{n}}{\Delta y^2}\right]\ .\end{aligned} \tag{2.20}$$

To constrain the plate stretching during the deformation we impose the inextensibility condition. This condition is enforced numerically by introducing a differential arc-length $ds^2 = dx^2 + dw^2$ that is numerically approximated as

$$x_{i+1} = x_i + \sqrt{\Delta s^2 - (w_{i+1} - w_i)^2}\ . \tag{2.21}$$

The PDE can be rewritten as

$$\rho_s h\frac{\partial^2 w}{\partial t^2} = q(x,y,t)+\left(N_x\frac{\partial^2 w}{\partial x^2}+N_y\frac{\partial^2 w}{\partial y^2}+N_{xy}\frac{\partial^2 w}{\partial x\partial y}\right)+\mathcal{L}\left(w,D\right)(x,y,t)-\mathcal{L}\left(\frac{\partial w}{\partial t},\gamma\right)(x,y,t)\ . \tag{2.22}$$

Here $\mathcal{L}$ is an operator defined as $\mathcal{L} : (u_1, u_2) \longmapsto -u_2\nabla^4 u_1$. The PDE is completed with appropriate boundary conditions on the displacement, moments and forces.

$$
\begin{aligned}
&w(0,y,t) = B \wedge \frac{\partial w}{\partial x}(0,y) = 0 : \text{ clamped root,}\\
&M_x(L,y) = 0 \wedge V_x(L,y) = 0 : \text{ free tip,}\\
&M_y(x,0) = 0 \wedge V_y(x,0) = 0 : \text{ free side,}\\
&M_y(x,w) = 0 \wedge V_y(x,w) = 0 : \text{ free side.}
\end{aligned}
$$

Here, $B = A(t)$ for the externally actuated plate, whereas in the case of the internally actuated plate, $B = 0$. Furthermore, $V_x(x,y) = Q_x(x,y) + \frac{\partial M_{xy}}{\partial y}(x,y)$ is the equivalent shear force, which was introduced by Kirchhoff [57] to reduce the number of boundary conditions to two. The corner reaction is defined as

$$
R = 2M_{xy}(x,y) = -2D(1-\nu)\frac{\partial^2 w}{\partial x \partial y}\bigg|_{x,y} . \tag{2.23}
$$

2.2.1.2 Isotropic Inhomogeneous Plate

For an inhomogeneous isotropic material the PDE modeling the behavior of the plate is identical to eq. (2.22) with the exception of the operator $\mathcal{L}$ defined as

$$
\begin{aligned}
\mathcal{L} : (u_1,u_2) \longmapsto &- u_2\nabla^4 u_1 - \left(\frac{\partial^2 u_2}{\partial x^2} + \nu\frac{\partial^2 u_2}{\partial y^2}\right)\frac{\partial^2 u_1}{\partial x^2} - \left(\frac{\partial^2 u_2}{\partial y^2} + \nu\frac{\partial^2 u_2}{\partial x^2}\right)\frac{\partial^2 u_1}{\partial y^2}\\
&- 2\frac{\partial^3 u_1}{\partial x^3}\frac{\partial u_2}{\partial x} - 2\frac{\partial^3 u_1}{\partial y^3}\frac{\partial u_2}{\partial y} - 2\frac{\partial^3 u_1}{\partial x \partial y^2}\frac{\partial u_2}{\partial x} - 2\frac{\partial^3 u_1}{\partial x^2 \partial y}\frac{\partial u_2}{\partial y}\\
&- 2(1-\nu)\frac{\partial^2 u_2}{\partial x \partial y}\frac{\partial^2 u_1}{\partial x \partial y} .
\end{aligned} \tag{2.24}
$$

Here the thickness, stiffness and Kelvin-Voigt damping factor are functions of x and y. We solve the plate equation of motion with relevant boundary conditions using finite differences. The time and space discretization is based on a central finite dif-

ference scheme with ghost nodes at the boundaries. This choice of the discretization results in a 13 points stencil for the displacement and 9 points stencil for the stiffness/damping. The undamped ($\gamma(\underline{x},t) = 0$) PDE for the isotropic inhomogeneous plate 2.24 discretized with central finite differences gives

$$
\begin{aligned}
&\frac{\rho_{i,j}h_{i,j}}{\Delta t^2}\left(w_{i,j}^{n+1} - 2w_{i,j}^{n} + w_{i,j}^{n-1}\right) = \; w_{i+2,j}^{n}\left(\frac{D_{i-1,j} - 2D_{i,j} - D_{i+1,j}}{2\Delta x^4}\right) + w_{i-2,j}^{n}\left(\frac{D_{i+1,j} - 2D_{i,j} - D_{i-1,j}}{2\Delta x^4}\right) \\
&+w_{i,j+2}^{n}\left(\frac{D_{i,j-1} - 2D_{i,j} - D_{i,j+1}}{2\Delta y^4}\right) + w_{i,j-2}^{n}\left(\frac{D_{i,j+1} - 2D_{i,j} - D_{i,j-1}}{2\Delta y^4}\right) \\
&+w_{i+1,j}^{n}\left[4D_{i,j}\left(\frac{1}{\Delta x^4} + \frac{1}{\Delta x^2\Delta y^2}\right) - \frac{D_{i+1,j} - 2D_{i,j} + D_{i-1,j}}{\Delta x^4}\right. \\
&\quad \left. -\nu\frac{D_{i,j+1} - 2Di,j + D_{i,j-1}}{\Delta x^2\Delta y^2} + (D_{i+1,j} - D_{i-1,j})\left(\frac{1}{\Delta x^4} + \frac{1}{\Delta x^2\Delta y^2}\right)\right] \\
&+w_{i-1,j}^{n}\left[4D_{i,j}\left(\frac{1}{\Delta x^4} + \frac{1}{\Delta x^2\Delta y^2}\right) - \frac{D_{i+1,j} - 2D_{i,j} + D_{i-1,j}}{\Delta x^4}\right. \\
&\quad \left. -\nu\frac{D_{i,j+1} - 2Di,j + D_{i,j-1}}{\Delta x^2\Delta y^2} + (D_{i-1,j} - D_{i+1,j})\left(\frac{1}{\Delta x^4} + \frac{1}{\Delta x^2\Delta y^2}\right)\right] \\
&+w_{i,j+1}^{n}\left[4D_{i,j}\left(\frac{1}{\Delta y^4} + \frac{1}{\Delta x^2\Delta y^2}\right) - \frac{D_{i,j+1} - 2D_{i,j} + D_{i,j-1}}{\Delta y^4}\right. \\
&\quad \left. -\nu\frac{D_{i+1,j} - 2Di,j + D_{i-1,j}}{\Delta x^2\Delta y^2} + (D_{i,j+1} - D_{i,j-1})\left(\frac{1}{\Delta y^4} + \frac{1}{\Delta x^2\Delta y^2}\right)\right] \\
&+w_{i,j-1}^{n}\left[4D_{i,j}\left(\frac{1}{\Delta y^4} + \frac{1}{\Delta x^2\Delta y^2}\right) - \frac{D_{i,j+1} - 2D_{i,j} + D_{i,j-1}}{\Delta y^4}\right. \\
&\quad \left. -\nu\frac{D_{i+1,j} - 2Di,j + D_{i-1,j}}{\Delta x^2\Delta y^2} + (D_{i,j-1} - D_{i,j+1})\left(\frac{1}{\Delta y^4} + \frac{1}{\Delta x^2\Delta y^2}\right)\right] \\
&+w_{i+1,j+1}^{n}\left[-\frac{2D_{i,j}}{\Delta x^2\Delta y^2} + \frac{D_{i-1,j} - D_{i+1,j} + D_{i,j-1} - D_{i,j+1}}{2\Delta x^2\Delta y^2} \; -(1-\nu)\frac{D_{i+1,j+1} - D_{i+1,j-1} - D_{i-1,j+1} + D_{i-1,j-1}}{8\Delta x^2\Delta y^2}\right] \\
&+w_{i-1,j+1}^{n}\left[-\frac{2D_{i,j}}{\Delta x^2\Delta y^2} + \frac{D_{i+1,j} - D_{i-1,j} + D_{i,j-1} - D_{i,j+1}}{2\Delta x^2\Delta y^2} \; +(1-\nu)\frac{D_{i+1,j+1} - D_{i+1,j-1} - D_{i-1,j+1} + D_{i-1,j-1}}{8\Delta x^2\Delta y^2}\right] \\
&+w_{i+1,j-1}^{n}\left[-\frac{2D_{i,j}}{\Delta x^2\Delta y^2} + \frac{D_{i-1,j} - D_{i+1,j} + D_{i,j+1} - D_{i,j-1}}{2\Delta x^2\Delta y^2} \; +(1-\nu)\frac{D_{i+1,j+1} - D_{i+1,j-1} - D_{i-1,j+1} + D_{i-1,j-1}}{8\Delta x^2\Delta y^2}\right] \\
&+w_{i-1,j-1}^{n}\left[-\frac{2D_{i,j}}{\Delta x^2\Delta y^2} + \frac{D_{i+1,j} - D_{i-1,j} + D_{i,j+1} - D_{i,j-1}}{2\Delta x^2\Delta y^2} \; -(1-\nu)\frac{D_{i+1,j+1} - D_{i+1,j-1} - D_{i-1,j+1} + D_{i-1,j-1}}{8\Delta x^2\Delta y^2}\right] \\
&+w_{i,j}^{n}\left[-D_{i,j}\left(\frac{6}{\Delta x^4} + \frac{8}{\Delta x^2\Delta y^2} + \frac{6}{\Delta y^4}\right) \; +2\left(D_{i+1,j} - 2D_{i,j} + D_{i-1,j}\right)\left(\frac{2}{\Delta x^4} + \frac{2\nu}{\Delta x^2\Delta y^2}\right)\right. \\
&\quad \left. +2\left(D_{i,j+1} - 2D_{i,j} + D_{i,j-1}\right)\left(\frac{2}{\Delta y^4} + \frac{2\nu}{\Delta x^2\Delta y^2}\right)\right].
\end{aligned}
\tag{2.25}
$$

2.2.2 Lattice Spring Method (LSM)

Just as FD is an efficient discretization of PDEs on regular geometries, it becomes significantly more complex to use this framework on complex geometries. On the other hand, the lattice spring method (LSM) is tailored to study the solid mechanics of complex geometrical shapes. It has been widely used to model large deforma-

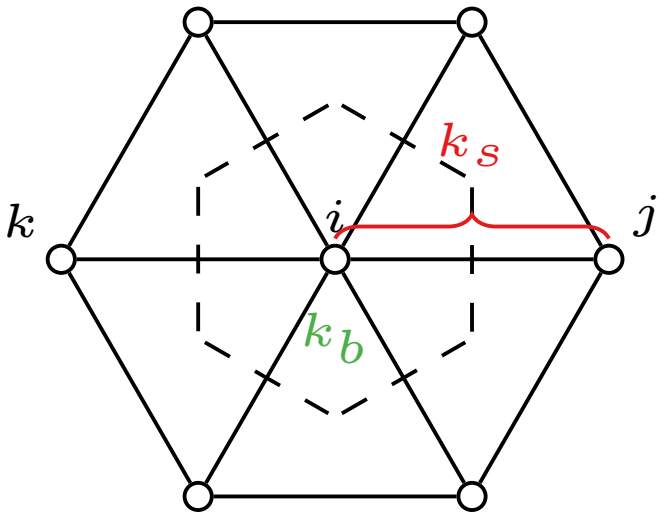

Figure 2.1: Schematics of a triangular lattice in LSM. The mass node i is connected to neighboring nodes $j, k \in [\![1; 6]\!]$ by a series of stretching and torsional springs with respective constants k_s and k_b. Stretching springs connect every ij pair while torsional springs are placed at node i are defined for every colinear triplet kij (6 stretching springs and 3 torsional springs for this unit cell). The dashed contour delimits the Voronoi region of the element.

tions of elastic materials. One of the main advantages of LSM when compared to the finite elements method (FEM) is its inherent simplicity in both formulation and computation. While FEM require the inversion of large matrices, LSM requires significantly less computational effort. In LSM, instead of discretizing solid mechanics equations directly on elements, volumes or points, a continuous solid is discretized by a network of masses and springs. The mapping of the discrete network properties (mass and stiffness constant) to macroscopic quantities (total mass, bending stiffness, etc.) depends intrinsically on the type of lattice network used. For instance, it has been shown that discrete triangular lattices recover the macroscopic properties of an isotropic material. Additional springs or forces can be added to modify the macroscopic behavior of the network. Applying the conservation of momentum to the mass points gives a set of differential equations modeling the motion of the nodes.

Figure 2.1 illustrates a triangular lattice unit. Node i is linked to $\mathcal{N}(i) = 6$ regularly spaced neighboring nodes by Hookean springs with spring constant k_s. The

dashed contour delimits the Voronoi region of the element associated to node i. The energy due to stretching at node i is given by

$$U_s = \frac{k_s}{2} \sum_{j=1}^{\mathcal{N}(i)} \left(\left\| \underline{r}_i - \underline{r}_j \right\| - r_{eq} \right)^2 \tag{2.26}$$

where $\underline{r}_i$ is the position of node i, r_{eq} is the equilibrium length of the spring connecting nodes i, j, $\|\cdot\|$ is the Euclidian norm and $\mathcal{N}(i)$ is the direct neighborhood to node i (here $\mathcal{N}(i) = 6$). The total stretching force acting on node i can be found by taking the gradient of the energy with respect to node i

$$\underline{F}_{\text{stretch},i} = \frac{\partial U_s}{\partial \underline{r}_i} = -k_s \sum_{j=1}^{\mathcal{N}(i)} \frac{\left\| \underline{r}_i - \underline{r}_j \right\| - r_{eq}}{\left\| \underline{r}_i - \underline{r}_j \right\|} \left(\underline{r}_i - \underline{r}_j \right) . \tag{2.27}$$

Such an equilateral triangular network with constant spring constants leads to isotropic mechanical properties. Young's modulus E can be retrieved from the network properties as $E = \frac{2}{\sqrt{3}} k_s$ and the Poisson ratio ν is constant $\nu = \frac{1}{3}$ [58]. This constant Poisson ratio is one of the limitation of "vanilla" LSM but it is easily overcome by changing the shape of the network or adding springs. To model the bending of the plate, torsional springs are added at node i.

A bending unit is defined as a colinear triplet ijk where nodes j and k are symmetric with respect to node i. For instance, on figure 2.1 there are three bending units ijk. A torsional spring is placed for each bending unit in a unit cell. Once more, assuming a constant torsional spring constant k_b, the energy due to bending can be computed as

$$U_b = \frac{k_b}{2} \sum_{j,k=1}^{\mathcal{B}(i)} \left[\cos\theta_{ijk} - \cos\theta_0 \right] \tag{2.28}$$

where $\mathcal{B}(i)$ are the bending units associated to the unit cell at node i, $\theta_0 = \pi$ is the equilibrium angle and θ_{ijk} is the angle between edges ij and ik. Once more, the force

can be found by taking the gradient of the bending energy and we have

$$\underline{F}_{\text{bend},j} = -\frac{k_b}{\left\|\underline{r}_i - \underline{r}_j\right\| \left\|\underline{r}_i - \underline{r}_k\right\|} \left[\underline{r}_i - \underline{r}_k - \frac{\cos\theta_{ijk}}{\left\|\underline{r}_i - \underline{r}_j\right\|^2} \left(\underline{r}_i - \underline{r}_j\right)\right], \tag{2.29}$$

$$\underline{F}_{\text{bend},k} = -\frac{k_b}{\left\|\underline{r}_i - \underline{r}_j\right\| \left\|\underline{r}_i - \underline{r}_k\right\|} \left[\underline{r}_i - \underline{r}_j - \frac{\cos\theta_{ijk}}{\left\|\underline{r}_i - \underline{r}_k\right\|^2} \left(\underline{r}_i - \underline{r}_k\right)\right], \tag{2.30}$$

$$\underline{F}_{\text{bend},i} = -\left(\underline{F}_{\text{bend},j} + \underline{F}_{\text{bend},k}\right) \ . \tag{2.31}$$

For a triangular lattice, such torsional springs lead to a constant bending stiffness $D = \frac{3\sqrt{3}}{4} k_b$ [58]. In addition to the stretching and torsional springs, the LSM network is completed with dashpots between each node in order to mitigate high mode oscillations that might destabilize the FSI coupling. The damping force is proportional to the relative velocity between nodes so that the overall momentum is conserved. This force can be expressed as

$$\underline{F}_{\text{damping},i} = \frac{\alpha_d}{\left\|\underline{r}_i - \underline{r}_j\right\|^2} \left[\left(\underline{v}_i - \underline{v}_j\right) \cdot \left(\underline{r}_i - \underline{r}_j\right)\right] \left(\underline{r}_i - \underline{r}_j\right) \tag{2.32}$$

where α_d is a damping coefficient that can be tuned to stabilize computations. The sum of stretching, bending and damping forces can be regrouped as the internal forces acting on the network $\underline{F}_{\text{int}}$. Therefore the total force acting on node i is given by $\underline{F}_{\text{tot},i} = \underline{F}_{\text{int},i} + \underline{F}_{\text{ext},i}$, where $\underline{F}_{\text{ext},i}$ is the sum of external forces acting on node i such as the fluid forces. By applying Newton's second principle, the equation of motion for node i is defined as

$$m_i \frac{d\underline{v}_i}{dt} = \underline{F}_{\text{tot},i} \tag{2.33}$$

where m_i is the mass of node i. The equations of motion can be integrated in time explicitly or implicitly. The explicit integration is significantly less computationally intensive however explicit integration with LSM has many shortcomings with regards

to FSI. The explicit integration leads to a condition on the time step $\Delta t < \frac{\Delta x^{LSM}}{c_p}$ where Δx^{LSM} is the lattice spacing, $c_p = \sqrt{\frac{K+4G}{3\rho_s}}$ is the celerity of P-waves, K and G are the bulk and shear modulus respectively. In addition to the conditional stability, explicit LSM suffers from spurious instability when $\Delta x^{LSM} < \Delta x^{LBM}$. The latter condition is specially detrimental for the spatial accuracy of the solid solver. Another important shortcoming of explicit LSM comes from a limit in density ratios. Indeed, a weak coupling between the fluid and solid solver leads to poor stability for higher density ratios.

On the other hand, an implicit integration of the equation of motion overcomes both shortcomings of the explicit integration. However, the implicit integration is not trivial and can be computationally intensive as it necessarily involves the inversion of a matrix at each time step. Let us rewrite the equation of motion discretized in time with a first order implicit scheme

$$\frac{\underline{r}_i^{n+1} - \underline{r}_i^n}{\Delta t} = \underline{v}_i^{n+1} \tag{2.34}$$

$$m_i \frac{\underline{v}_i^{n+1} - \underline{v}_i^n}{\Delta t} = \underline{F}_{\text{tot},i}^{n+1} \ . \tag{2.35}$$

Equations 2.34 and 2.35 form a set of non-linear equations which can be solved using the Newton-Raphson method or a quasi-Newton method. Fortunately this problem can be simplified by adopting a semi-implicit stance where the linear part of the stretching force and the fluid forces are integrated implicitly while the non-linear part of the stretching and the bending forces are integrated explicitly. This semi-implicit approach does not lead to an unconditional stability however it alleviates significantly the limitations of the explicit integration [59], [60]. A straightforward manipulation of 2.27 shows that the total stretching force at node i can be split in a

linear and non-linear part as

$$\underline{F}_{\text{stretch},i} = -k_s \sum_{j=1}^{\mathcal{N}(i)} \left(\underline{r}_i - \underline{r}_j\right) - k_s \sum_{j=1}^{\mathcal{N}(i)} \frac{r_{eq}}{\left\|\underline{r}_i - \underline{r}_j\right\|} \left(\underline{r}_i - \underline{r}_j\right) = \underline{F}^{\text{linear}}_{\text{stretch},i} + \underline{F}^{\text{non-linear}}_{\text{stretch},i} \ . \tag{2.36}$$

Therefore we can rewrite equation (without damping for simplicity) 2.35 as

$$\underline{v}_i^{n+1} = \underline{v}_i^n + \frac{\Delta t}{m_i} \left(\underline{F}^{\text{linear},n+1}_{\text{stretch},i} + \underline{F}^{\text{non-linear},n}_{\text{stretch},i} + \underline{F}^{n}_{\text{bending},i} + \underline{F}^{n+1}_{\text{fsi},i}\right) \ . \tag{2.37}$$

The linear part of the stretching force a step $n+1$ can be computed with a first-order Taylor expansion $\underline{F}^{\text{linear},n+1}_{\text{stretch},i} = \underline{F}^{\text{linear},n}_{\text{stretch},i} + \frac{\partial \underline{F}}{\partial \underline{r}_i} \Delta \underline{r}_i^{n+1}$ where $\Delta \underline{r}_i^{n+1} = \underline{r}_i^{n+1} - \underline{r}_i^n = \left(\underline{v}_i^n + \Delta \underline{v}_i^{n+1}\right) \Delta t$. The matrix $\underline{\underline{H}} = \frac{\partial \underline{F}}{\partial \underline{r}_i}$ can be seen as a Jacobian (with respect to the force) or Hessian matrix (with respect to the energy). The computation of $\underline{\underline{H}}$ is straightforward [61], [62]

$$H_{ij} = k_{s,ij} \ , \ i \neq j \tag{2.38}$$

$$H_{ii} = -\sum_{j=1}^{\mathcal{N}(i)} k_{s,ij} \ . \tag{2.39}$$

The Hessian matrix can also be seen as the discretization of the Laplace-Beltrami operator on an equilateral triangular mesh [63]. We can now regroup terms in eq. 2.37

$$\left(\underline{\underline{I}} - \frac{\Delta t^2}{m_i} \underline{\underline{H}}\right) \Delta \underline{v}_i^{n+1} = \frac{\Delta t}{m_i} \left(\underline{F}^n_{\text{int},i} + \underline{F}^{n+1}_{\text{fsi},i} + \underline{\underline{H}} \ \underline{v}_i^n \Delta t\right) \ . \tag{2.40}$$

Equation 2.40 now forms a system of linear equations which can be solved directly or iteratively. This is an expensive problem as $\underline{\underline{H}}$ is a $3N \times 3N$ matrix where N is

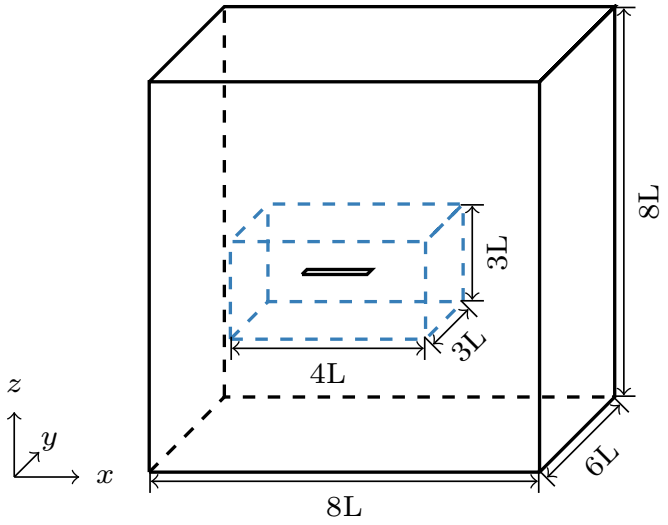

Figure 2.2: Computational setup schematics. Both the coarse (black) and fine (blue) boxes enclose the solid plate which lies into the fine mesh.

the total number of nodes. Fortunately, as long as the network parameters m_i and k_s are constant, the matrix $\left(\underline{\underline{I}} - \frac{\Delta t^2}{m_i}\underline{\underline{H}}\right)$ stays constant throughout the computation. Therefore, the matrix and its inverse can be computed once at the start of the computation. Besides, due to the structure of the network, $k_{s,ij}$ the spring constant between nodes i and j is non-zero if and only if $j \in \mathcal{N}(i)$ therefore $\left(\underline{\underline{I}} - \frac{\Delta t^2}{m_i}\underline{\underline{H}}\right)$ is sparse. The matrix inversion is carried out iteratively by using the conjugate gradient method for sparse matrices from the Eigen framework [64].

2.3 Computational Setup

The computational domain consists into two boxes centered around the plate. The solid plate lies into the inner most box, referred to as the fine grid where the spacing is $\Delta_{x,f} = \Delta_{y,f} = \Delta_{z,f} = 1$. The outer most box, referred to as the coarse grid where the grid spacing is $\Delta_{x,c} = \Delta_{y,c} = \Delta_{z,c} = 2$, encloses both the fine grid and the solid plate. The swimmer of length $L = 50$ LBM units lies one body-length away from the fine mesh's $-x$–plane and equidistant from the y and z planes. The computational domain is made large enough so that the wake dissipates before reaching the boundaries.

2.4 Boundary Conditions

The coarse and fine grids are coupled through a multi-step procedure. The boundary conditions on the coarse grid are either periodic or a pressure boundary condition. At the fluid-solid boundary we apply no-slip and no-penetration conditions using a linearly interpolated bounce-back scheme. The distribution functions propagating into the plate are reflected back into the opposite direction while taking into account the position and velocity of the intersecting point on the solid surface. The momentum resulting from the reflection of the distribution function is then transferred to the plate. This momentum transfer is represented by an equivalent force redistributed to the surrounding solid nodes using a weighted average based on distances while conserving normal and tangential forces on the boundary. This fluid-solid coupling procedure has been previously extensively validated and used to study diverse fluid-structure interaction problems [49], [65]–[70].

When integrating the equation of motion discretized with either FD or LSM, the treatment of $\underline{F}_{\text{fsi}}$ is critical for the stability and computational cost of the model. For instance, an explicit integration also known as weak coupling results in a lesser computational load at the cost of stability. A weak coupling falls short when the structure is too light compared to the fluid. On the other hand, an implicit (or strong) coupling results in a significantly more stable model at the cost of a heavier computational load [71]–[73].

2.5 Validation

2.5.1 Homogeneous Plate

We validate the FD solid solver by modeling static deflection of a cantilevered plate due to a load applied at the free end. The numerical solution is compared with the deflection of an Euler-Bernoulli beam with a bending stiffness EI described using the

following boundary-value problem

$$\forall s \in]0;1[,\ \theta''(s) = -\frac{q_0 L^2}{EI}\cos\theta(s)\ , \tag{2.41}$$

$$\theta(0) = 0\ , \theta'(1) = 0\ . \tag{2.42}$$

Here, q_0 is the load, s is the arc length coordinate, L is the length of the beam and θ is the beam angle. The equation is solved using a fourth-order Runge-Kutta scheme.

In figure 2.3, the beam solution is compared to our FD solution for various loads. We find close agreement between the finite differences results and the Runge-Kutta solution with tip deflections reaching up to 70% of the beam length for a mesh of 20 nodes in the length and 11 nodes in the width.

2.5.2 Inhomogeneous Beam & Plate

We mirror the same approach to validate the tapered plate solver. We first consider a beam of varying thickness $h : x \longmapsto \left[r_h + (1 - r_h)\frac{x}{L}\right]\frac{h_0}{r_h}$ and therefore bending stiffness $EI : x \longmapsto \frac{Eh^3(x)w}{12}$. Here h_0 and $r_h = h_0/h_L$ are respectively the thickness at the root and the ratio of the thickness at the root and the tip, called tapering ratio. The PDE modelling the deflection of an end-loaded inhomogeneous beam then becomes

$$\forall s \in]0;1[,\ \left(\frac{EI(s)}{EI_0}\theta'(s)\right)' = -\frac{q_0 L^2}{EI_0}\cos\theta(s)\ , \tag{2.43}$$

$$\theta(0) = 0\ , \theta'(1) = 0\ . \tag{2.44}$$

Here EI_0 is the bending rigidity at the root and q_0 is the load. In order to compare our plate solver to a beam solution we set the Poisson ratio $\nu = 0$. Even though the

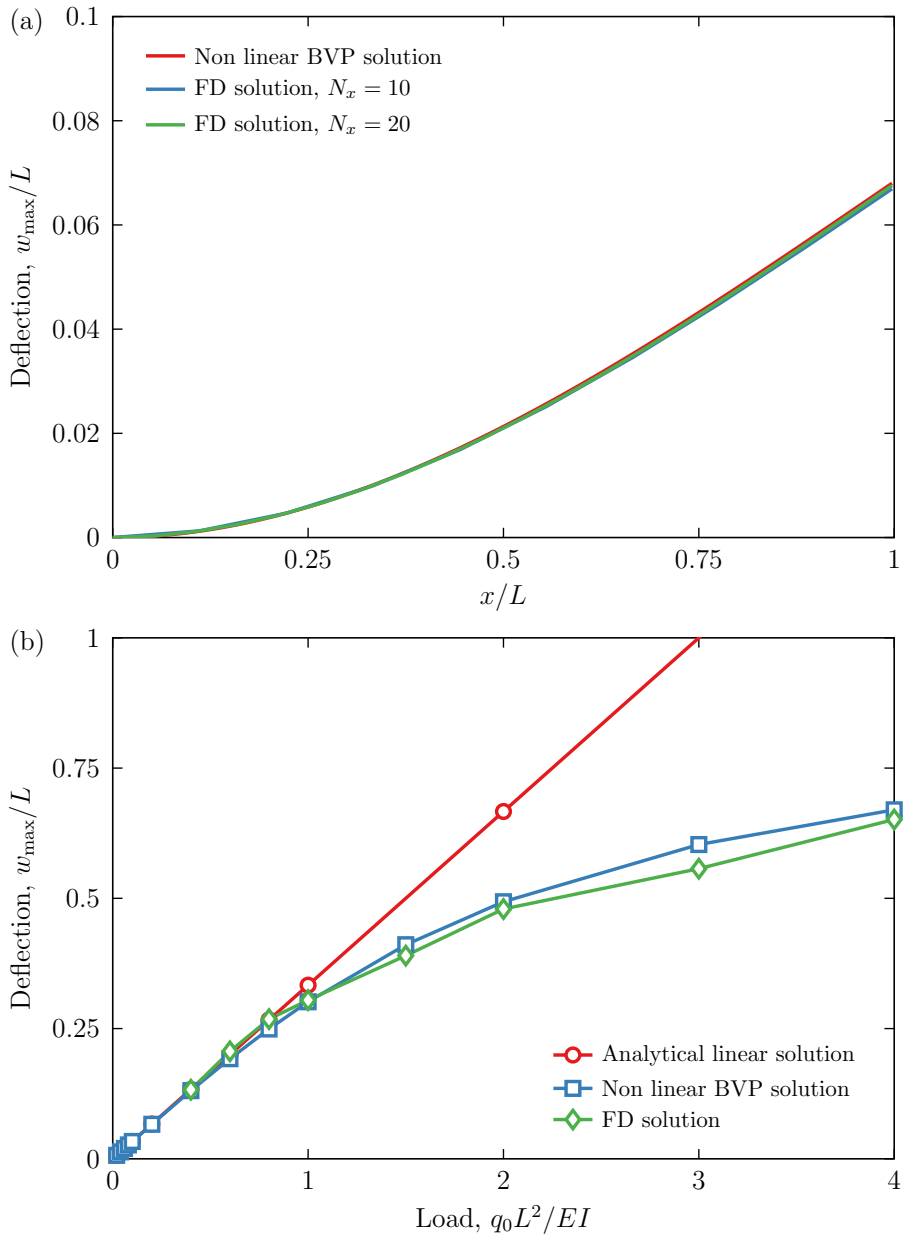

Figure 2.3: (a) Bending deformation of the end-loaded cantilevered plate with aspect ratio $\mathcal{A}_\mathcal{R} = 2$ and a non-dimensional load $q_0L^2/EI = 0.2$. The finite difference solution using 20 node mesh deviates less than 1% from the non-linear BVP solution. (b) Static deflection of the end-loaded cantilevered plate with aspect ratio $\mathcal{A}_\mathcal{R} = 2$ as a function of the non-dimensional load q_0L^2/EI. The comparison between the non-linear Runge–Kutta and the finite differences solutions shows good agreement including for moderate to high deformation levels. The linear analytical solution only valid for relatively small loads.

beam is inhomogeneous, as it is clamped at the root and under a concentrated load at the tip, we expect the bending moment to vary linearly from the root to zero at the tip. Once again the FD solution shows good agreement with the Runge-Kutta solution for moderate tip deflection (up to 10% of the length), including the bending moment following the linear analytic profile as can be seen in figure 2.4a.

We also compare the FD scheme to an actual 3D simulation using Comsol, a commercial software based on the finite elements (FE) method. In the plate setup, the bending stiffness becomes $D = \frac{Eh^3}{12(1-\nu^2)}$ and we define D_0 the stiffness at the tip. Once more, we show good agreement between the FD and FE solutions for both the deflection and bending moment (figure 2.4b). However, in the 3D case, i.e. with a non-zero Poisson ratio, the evolution of the bending moment near the root ($x = 0$) shows that there are non-negligible 2D effects due to the clamped boundary condition.

2.5.3 Trapezoidal Plate

To validate LSM, we consider the static deflection of a non-rectangular cantilevered plate of length L and stiffness D under a load $q_0 L/D_0 = 0.15$. The LSM results are once more compared to Comsol. The trapezoidal geometry is characterized by the ratio of the width at the root and tip of the plate $\frac{w_r}{w_t} = 0.25$ as well as the aspect ratio $\mathcal{A}_R = \frac{L}{w_r} = 2.5$. The plate is discretized in LSM with $N = 231$ nodes and a equilibrium length $r_{eq} = 2.325$ LBU. In Comsol, the plate is discretized with $N_e = 2623$ elements and quadratic polynomials. The resulting centerline deflection is shown in figure 2.5. We find good agreement between LSM and Comsol for the trapezoidal plate with less than 2% deviation which demonstrates LSM's capability to model elastic plates of various shape.

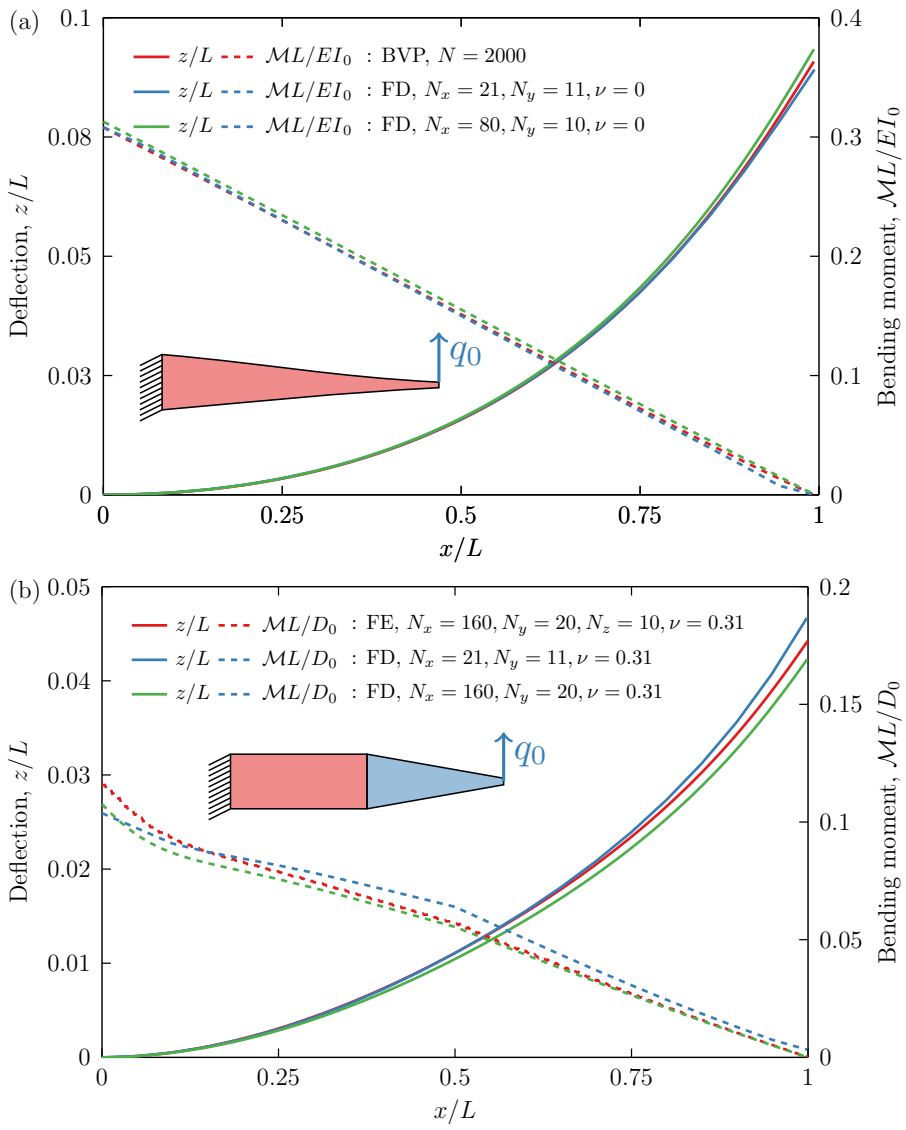

Figure 2.4: Static deflection under a non-dimensional load (a) $q_0L^2/EI_0 = 0.1$ of a fully tapered end-loaded cantilevered beam ($\nu = 0$) using finite differences and a Runge-Kutta scheme and (b) hybrid uniform and tapered cantilevered plate ($\nu = 0.31$) under a non-dimensional load $q_0L^2/D_0 = 0.1$ using finite differences and Comsol.

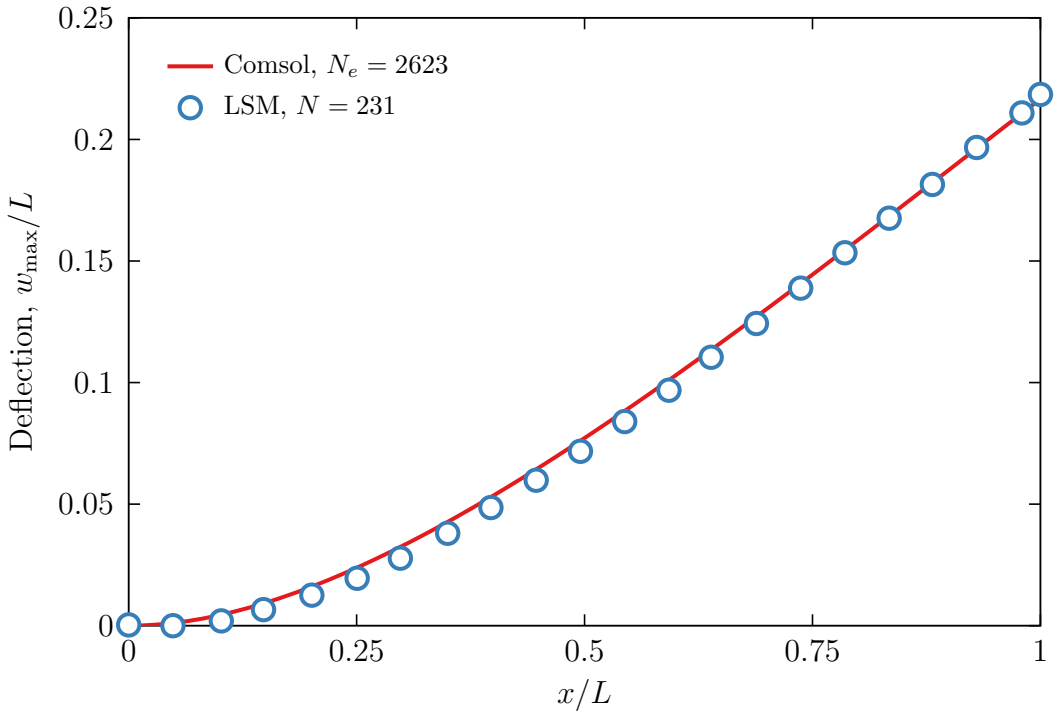

Figure 2.5: Centerline static deflection under a non-dimensional load $q_0 L/D_0 = 0.15$ of a trapezoidal cantilevered plate using LSM and Comsol.

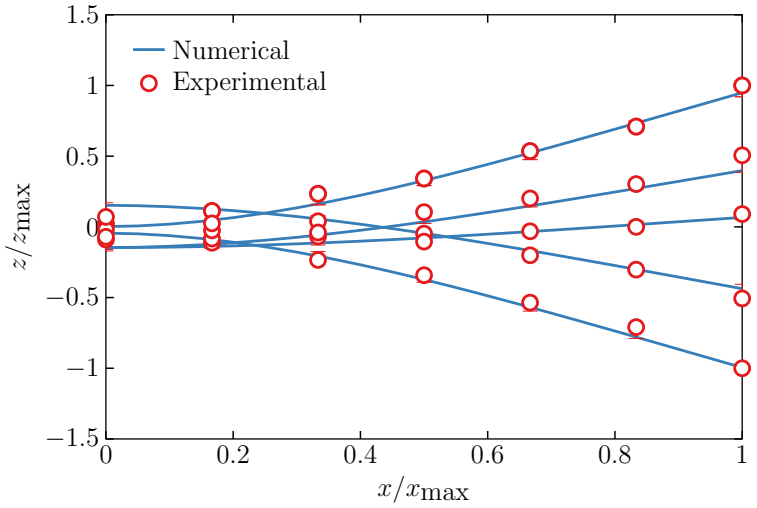

Figure 2.6: Externally (base excited) actuated plate bending patterns at resonance. Numerical results are shown by the solid lines, whereas experimental data is shown by the symbols. The plate tip displacement is $\delta_t = 0.01L$, the aspect ratio is $\mathcal{A}_\mathcal{R} = 2$, and $Re = 1000$.

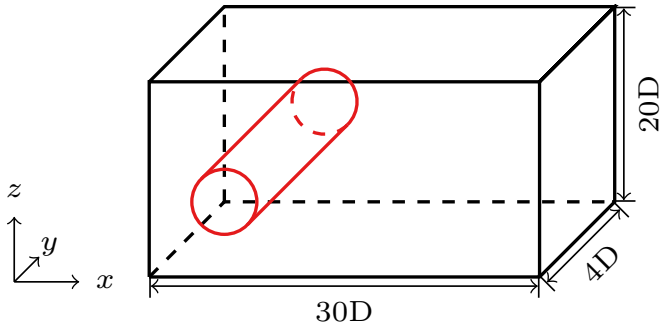

Figure 2.7: Oscillating cylinder computational setup schematics. Here, only the fine grid is represented.

2.5.4 Coupled FSI

2.5.4.1 Laminar flow

To further quantify the accuracy of our model we compare our numerical solution to underwater experiments. In this configuration the plate is homogeneous and actuated at the root with an external harmonic amplitude $A(t) = A_0 \sin(\omega t)$ leading to a tip deflection $\delta_t/L = 0.01$. We perform the computation for 20 periods to reach a steady state and compare to the experimental measurements. In figure 2.6 we show good agreement between the numerical solution and experiments with little discrepancy.

2.5.4.2 Turbulent flow

We validate the LES turbulence model by comparing the draft an lift coefficients of an oscillating cylinder of diameter D and length L in an external flow. The cylinder oscillates harmonically in the direction transverse to the flow with an amplitude $A_0 = 0.3D$ and period τ so that the motion of the cylinder w is given by $w(t) = A_0 \sin \frac{2\pi t}{\tau}$. The physics of this problem is governed by the Reynolds number $Re_D = \frac{U_0 D}{\nu} = 10^4$ where U_0 is the free stream velocity, the Strouhal number $St_D = \frac{D}{\tau U_0}$ and the cylinder blockage ratio $\beta = \frac{D}{L} = 0.1$. The domain represented in figure 2.2 consists of a fine grid of size $30D \times 20D \times 4D$ and a coarse grid of size $60D \times 10D \times 2D$. It is periodic in the direction of the cylinder's length to model an infinite cylinder.

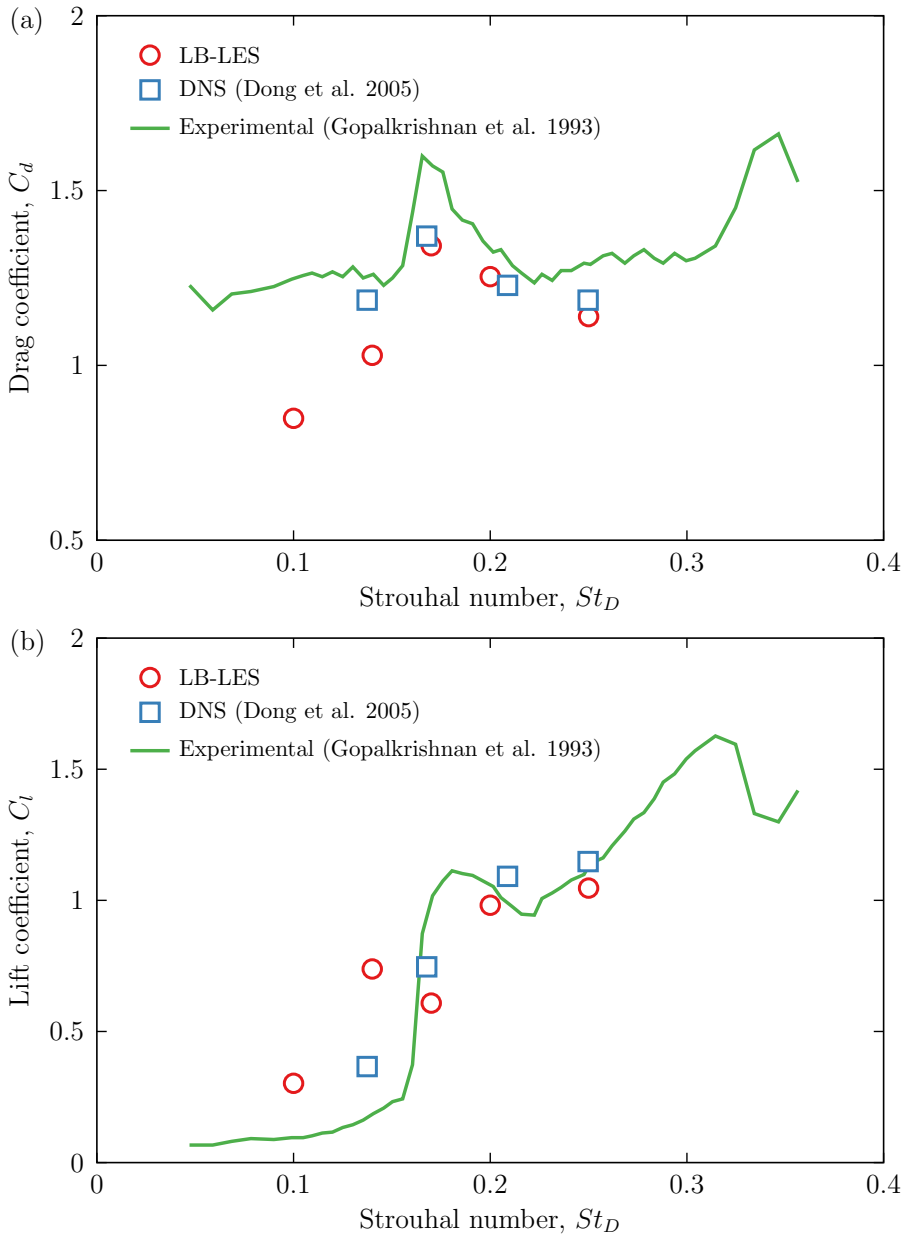

Figure 2.8: Evolution of the (a) mean drag and (b) magnitude of lift coefficients for an oscillating cylinder with amplitude $A_0 = 0.3D$ and $Re = 10^4$.

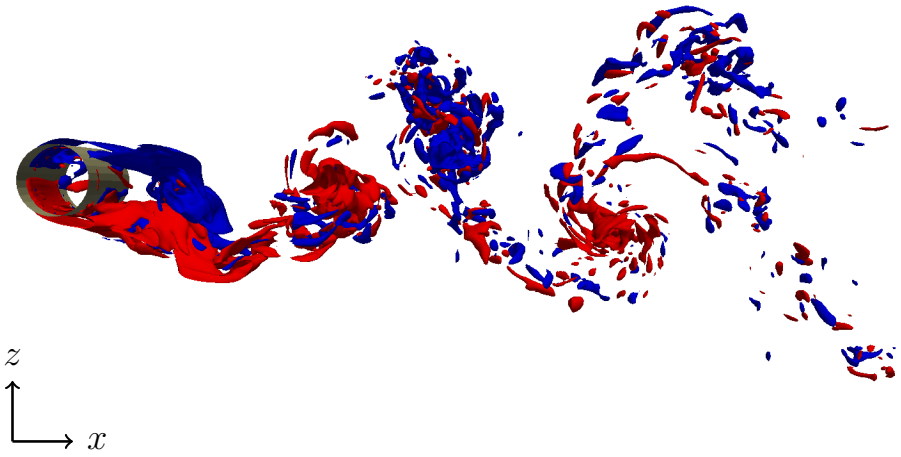

Figure 2.9: Vorticity contours for $\omega\tau = \pm 20$ for an oscillating cylinder with amplitude $A_0 = 0.3D$, $St_D = 0.17$ and $Re = 10^4$.

To benchmark our model, we compare the mean drag and magnitude of lift coefficient $C_d = \frac{F_x}{\frac{1}{2}\rho U_0^2 D}$ and $C_l = \frac{F_z}{\frac{1}{2}\rho U_0^2 D}$ to DNS [74] and experimental results [75] for a set of St_D. Gopalkrishnan [75] showed that both the drag and lift coefficients present a sharp increase for $St_D \sim 0.2$. In figure 2.8a we show that the results from our LB-LES model captures the global trend of the experimental data. The LES is able to capture the local increase in C_d near $St_D = 0.2$ however it underestimates the mean drag for lower St_D. Similarly, in figure 2.8b our results show that the LB-LES model can capture the global trend of the lift coefficient specially near $St_D = 0.2$ but it tends to overestimate the lift at lower St_D.

In figure 2.9 we show the vortex structure generated in the wake of the cylinder. As expected in this configuration the wake is made of alternating rotating and counter-rotating vertices shedding away from the cylinder. Overall, the agreement between the LES and experimental measurements demonstrates the model's capacity to capture turbulent effects with moving boundaries.

2.6 System Parameters

Let us consider a thin elastic plate with length L, width W, and uniform thickness $h \ll L$ yielding an aspect ratio $\mathcal{A}_\mathcal{R} = L/W$. The plate oscillates periodically in an incompressible Newtonian fluid of density $\rho = 1$ LB units and dynamic viscosity μ. In every study the plate is actuated at a constant period $\tau = 2000$ LB units and therefore constant angular frequency ω. The fluid regime is characterized by the Reynolds number $Re = \frac{\rho U_c L_c}{\mu}$. Here, we choose the length of the plate as the characteristic length $L_c = L$ and the characteristic velocity $U_c = \frac{L}{\tau}$. Furthermore, the dynamic response of the submerged structure heavily depends on the mass ratio $\chi = \frac{\rho W}{\rho_s h}$. Additionally, we define a characteristic force $F_c = \frac{1}{2}\rho W L U_c^2$ and power $P_c = \frac{1}{2}\rho W L U_c^3$.

The dynamic response of an oscillating elastic plate is a function of the proximity of the driving frequency to the plate resonance frequency. The resonance frequency depends on the properties of the plate material as well as the fluid surrounding the plate. In vacuum and by neglecting internal dissipation (structural damping), small deflections of a beam with bending rigidity D and mass per length $M_l = \rho_s W h$ can be modelled by

$$M_l \frac{\partial^2 w}{\partial t^2} + D \frac{\partial^4 w}{\partial x^4} = 0 \ . \tag{2.45}$$

This problem can be solved using Fourier decomposition [76] yielding the natural frequencies $\omega_{n,\text{vac}}$ given by

$$\omega_{n,\text{vac}} = \frac{\lambda_n^2}{L^2}\sqrt{\frac{D}{M_l}} \ , \tag{2.46}$$

where λ_n is an eigenvalue of the problem, $n \in \mathbb{N}^*$ and the first vibration mode, $n = 1$, is of interest in this work. The natural frequency, corresponding to the condition when the response and excitation are in quadrature of phase, yields the maximum tip

deflection. In the lightly damped problem, such as the vacuum case, the resonance frequency is approximately the natural frequency. Fluid displaced by the oscillating plate acts as an additional mass altering the dynamics of the plate. When the added mass is significantly greater than the plate mass, the effective linear mass due to the displaced fluid can be used instead of the plate mass. This leads to a dimensionless effective flexibility $D^* = (\rho W f^2 L^5/D)^{\frac{1}{2}}$ representing the ratio of added mass forces to internal bending forces [43].

When the plate is driven to oscillate in a fluid, the resonance frequency defines the oscillation regime maximizing the tip deflection. Fluid viscosity affects the forced resonance frequency, although for low fluid damping the resonance frequency overlays with the natural (undamped) frequency. Note that [43] and [44] have shown for elastic plates that the maxima of the thrust and tip deflection occur for the same effective flexibility. Thus, the values of D^* corresponding to the maximum thrust match the forced resonance frequency. We also note that experimentally the frequency sweep is performed by varying the actuation frequency. In our numerical simulations, however, the actuation frequency is constant, whereas the stiffness is varied to alter the proximity of the oscillating plate to the resonance frequency.

To quantify the variation of the stiffness (equivalent to a varying frequency) we define the stiffness ratio $r = \sqrt{\frac{D_1}{D}}$ which to the first order approximates the frequency ratio $r \simeq \frac{\omega}{\omega_{1,\text{vac}}}$, where D_1 is the bending stiffness that yields the first natural frequency. Therefore, for $r = 1$ the plate is actuated at its first natural frequency.

In the case where the plate is constrained horizontally to oscillate in place, we characterize the performance of the plate by computing the period-averaged forces $\overline{F}_i$ and power $\overline{P}$ as $\overline{F}_i = \frac{1}{\tau}\int_t^{t+\tau} \underline{F}(t) \cdot \underline{e}_i dt$ and $\overline{\mathcal{P}} = \frac{1}{\tau}\int_t^{t+\tau} \mathcal{P}(t) dt$. Here $\underline{e}_i$ is the orthonormal basis vector, $\mathcal{P}(t) = \underline{F}(t) \cdot \underline{v}(t)$ is the instantaneous power and $\underline{v}$ is the instantaneous velocity. We then define a propulsion efficiency as $\eta = \frac{\overline{F}_x/F_c}{\overline{\mathcal{P}}/P_c}$.

When the plate is let free swimming, the period-averaged thrust is null by def-

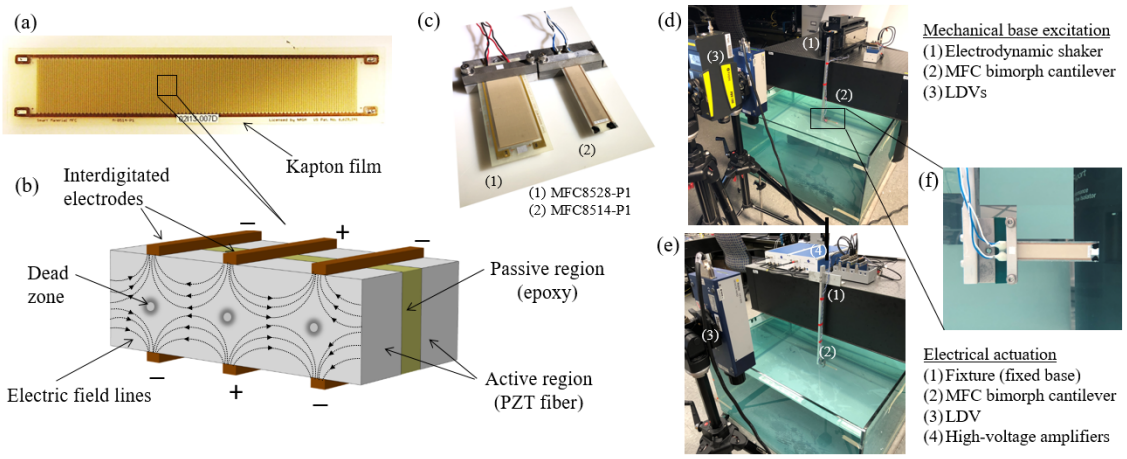

Figure 2.10: Picture of (a) an MFC laminate and (b) close-up schematic of a representative volume element showing the interdigitated electrodes, piezoelectric fibers, and epoxy matrix embedded in Kapton film. (c) Bimorph cantilevers with two different aspect ratios (each made from two MFC laminates for bending actuation). (d) Mechanical base excitation (external actuation) setup and (e) electrical (internal) actuation setup. (f) Close-up view of an MFC bimorph cantilever.

inition. Therefore we characterize the swimming performance by computing the period-averaged swimming velocity $\overline{U}$ and power $\overline{\mathcal{P}}$. We then define an economy $\varepsilon = \frac{\overline{U}/U_c}{\overline{\mathcal{P}}/P_c} = \frac{\overline{U}F_c}{\overline{\mathcal{P}}}$. The higher the economy, the further the plate travels for the same power input.

2.7 Experimental Setup

The experimental test samples, setup details and pictures are provided by Dr. Alper Erturk's SSDSL group at Georgia Tech.

The experimental test samples (piezoelectric cantilevers) and the overall setup details are shown in figure 2.10 along with close-up views of the relevant components. The flexible piezoelectric structures were built by vacuum bonding a pair of the identical custom-made waterproof MFC laminates using high strength epoxy (3M DP460) to fabricate bimorph structures. Electrical wires were soldered to the electrodes of the MFCs and the joint was fully waterproofed by multiple layers of liquid electrical tape (Star Brite Liquid Electrical Tape). Two different excitation mechanisms of

input energy are applied to create persistent oscillations of the cantilevers: electrical (internal) actuation and mechanical (external) base excitation.

First, in the piezoelectric actuation, the bimorphs were placed into an aluminum clamp attached to a rigid mount to create a cantilevered structure and electrically connected to a pair of high voltage amplifiers (Trek PA05039). Linear electrical actuation experiments were conducted with the sample in a vacuum chamber to characterize the dynamics of the structure in the absence of fluid loading. To do so, electrical noise bursts were sent to the piezoelectric bimorphs while the mechanical response at the tip of the cantilever was measured using a Laser Doppler Vibrometer (LDV) (OFV-5000 with an OFV-505 sensor head). Once the linear response was well characterized along with in vacuo structural damping, frequency sweeps were conducted around the first resonant frequency to measure the amplitude-dependence between the piezoelectric bimorph and the surrounding fluid. Later, the structure was submerged underwater to a depth of 25 centimeters to avoid surface effects. Linear electrical actuation experiments were repeated under water, being careful to divide the measured tip velocity underwater by the index of refraction of water to determine the true velocity of the structure. By comparing the dynamics of the structural modes from the in vacuo and underwater experiments, empirical linear inertia coefficients were extracted from the data. Once the linear tests were complete, the nonlinear response of the structure was again measured via frequency sweeps underwater centered around the first resonant frequency of the underwater structure.

For mechanical external actuation experiments, the bimorphs (along with the aluminum clamps) were fixed onto the testing platform of an APS-113 long-stroke shaker which was connected to an APS-125 amplifier. For the sake of the characterization of the dynamic response of the bimorphs under mechanical external actuation, linear vacuo tests were again conducted in a vacuum chamber to have a reference for obtaining the inertia coefficient. An LDV was used for obtaining the absolute tip velocity

$\mathcal{A}_\mathcal{R}$	$L(mm)$	$W(mm)$	$h(mm)$	$\rho_s(kg.m^{-3})$	$EI(N.m^2)$	χ
2	88.5	43.5	6.1	360	0.0163	20
4	83.5	21.5	6.1	360	0.087	10

Table 2.1: Experimental parameters

of the bimorphs, and at the same time, another LDV was implemented to collect the velocity-to-actuation voltage input frequency response from the fixed-end of the bimorphs. After the in vacuo reference experiments, the bimorphs were immersed in water along with an aluminum bar that one of its ends was attached to the shaker. Similarly, linear mechanical actuation tests were done to characterize the dynamics of the bimorphs to characterize fluid loading effects. Finally, large-amplitude frequency sweeps were conducted in the frequency range centered around the first resonant frequency obtained from the prior tests. Note that to keep the oscillation level at the fixed-end of the bimorphs constant within the entire range of frequency sweeps, the velocity signals obtained from the second LDV were sent into a controller to create a closed-loop feedback control system as required in nonlinear vibration experiments. Typical characteristic velocities lead to a Reynolds number in the range between 10^2 and 10^4.

CHAPTER 3
EFFECTS OF ACTUATION METHODS

3.1 Introduction

In this chapter, we investigate the fundamental effects of two different actuation methods on the hydrodynamics of an elastic plate. We consider two different configurations of the plate actuation. In the first configuration, referred to as an externally actuated plate, the elastic plate is actuated at its root with a harmonic plunging pattern given by $A(t) = A_0 L \sin \omega t$, where ω is the angular velocity, A_0 is the dimensionless root displacement amplitude, and t is time as shown in figure 3.1. In the second configuration, referred to as an internally actuated plate, the plate is driven by a harmonic internal bending moment given by $M(t) = M_0 DL/W \sin \omega t$ with M_0 being the dimensionless moment amplitude in the y direction. In the internally actuated configuration the plate root is clamped and fixed in place. Furthermore, the plate is actuated at resonance $r = 1$ to yield the highest tip deflection. We systematically investigate the kinematics, forces and flow patterns for both actuation methods. We show that the different actuation methods yield different kinematics that in turn results in significantly different hydrodynamic loading and performance. We show that the performance of the actuation methods drastically differs between low and high tip deflections. We demonstrate that, particularly at high tip deflection, externally actuated plates outperform internally actuated plates in both thrust and efficiency. In this chapter, $Re = 1000$ unless specified otherwise.

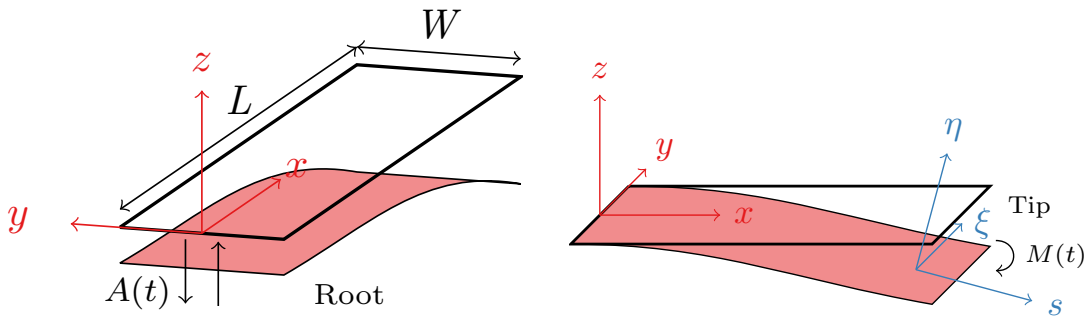

Figure 3.1: Schematics of rectangular elastic plates with (a) external and (b) internal actuation methods in the global and local reference frames. The externally actuated plate is driven at the root by harmonic oscillations with an amplitude $A(t)$. The internally actuated plate is driven by a time-dependent distributed internal bending moment $M(t)$.

3.2 Frequency Response

In figures 3.2 and 3.3, we present simulation results and experimental data for internally and externally actuated plates oscillating in water with a moderate tip deflection $\delta_t/L = 0.01$. Close agreement between the simulations and experiments confirms the ability of our coupled FSI solver to properly model such oscillations. Figure 3.2 shows the Bode diagrams for plates with external and internal actuation. The phase $\Delta\theta$ is computed as the lag between the root and tip displacements for the externally actuated plate. In the case of the internally actuated plate, $\Delta\theta$ is computed as the lag between the tip displacement and the input internal moment.

As the driving frequency approaches the resonance frequency of the plate, the tip velocity magnitude and, therefore, tip displacement reach a maximum (figure 3.2a). The resonance frequency can therefore be identified by inspecting the root mean square tip velocity V_{tip} frequency response. On the other hand the natural frequency can be identified by investigating the phase difference between the driving source (root displacement or internal moment) and the tip deflection. At the natural frequency the driving source and tip displacement are in quadrature of phase (figure 3.2b). For relatively small amplitude $\delta_t/L = 0.01$, the natural and resonance frequency coincide,

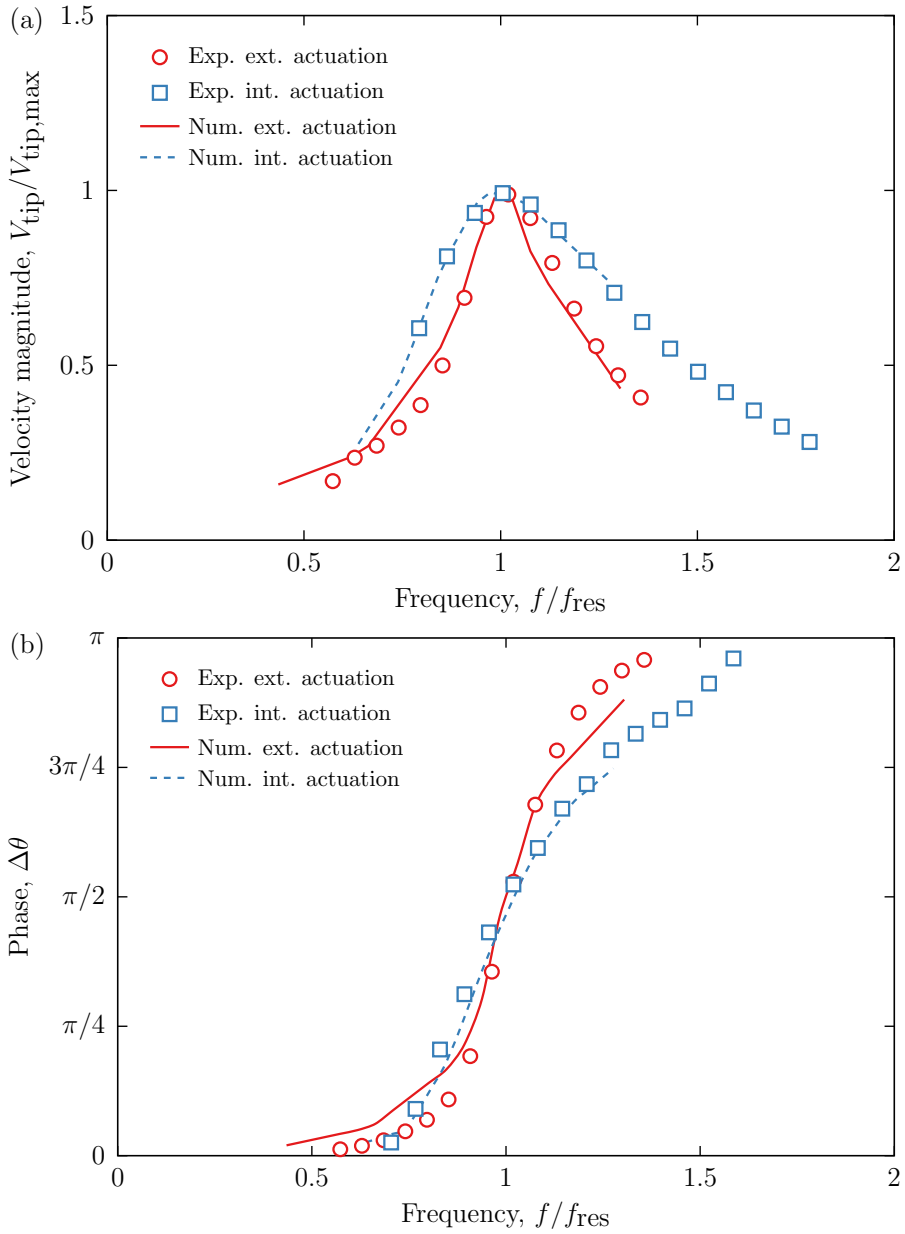

Figure 3.2: Frequency response function for (a) the tip velocity V_{tip} and (b) the phase for $\delta_t/L = 0.01$, $\chi = 5$ and $\mathcal{A}_{\mathcal{R}} = 2$. The numerical results are shown by the lines, whereas the experimental data is shown by the symbols. The resonance is characterized by a quadrature of phase $\Delta\theta = \pi/2$ between the root and the tip.

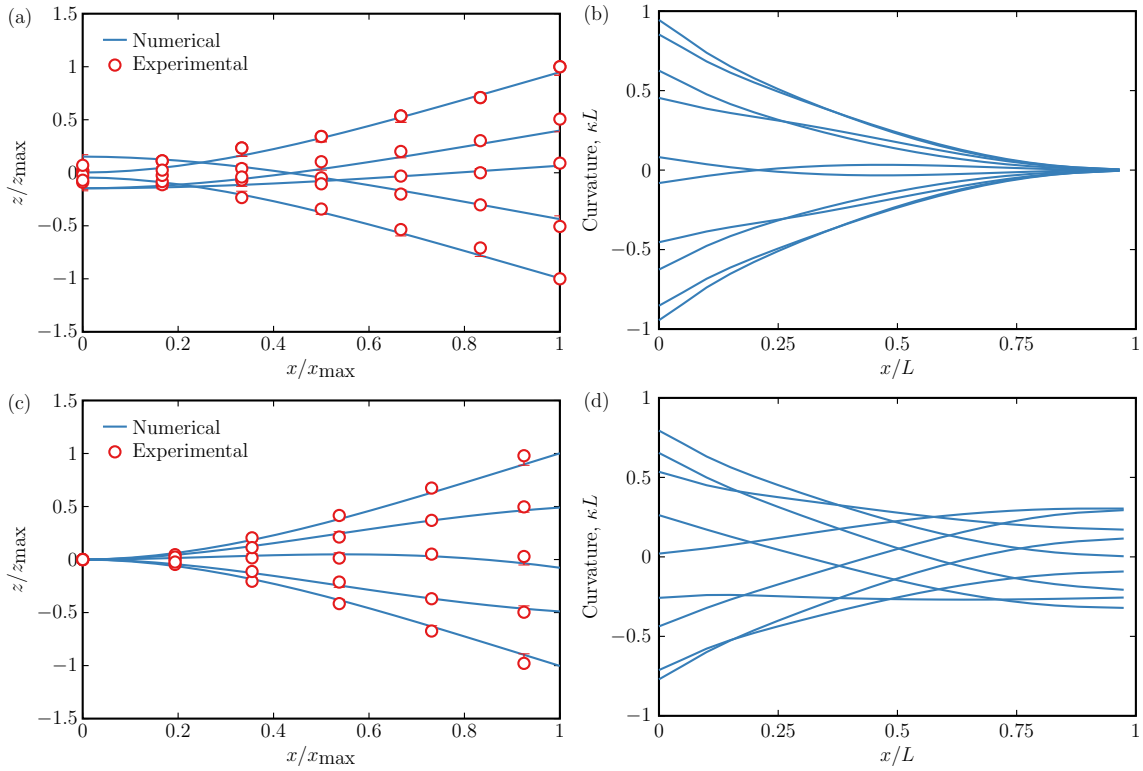

Figure 3.3: (a) Plate bending pattern and (b) bending curvature κ for the externally actuated plate at resonance. (c) Plate bending pattern and (d) bending curvature κ for the internally actuated plate at resonance. Numerical results are shown by the solid lines, whereas experimental data is shown by the symbols. The plate tip displacement is $\delta_t/L = 0.01$, the aspect ratio is $\mathcal{A}_\mathcal{R} = 2$, $\chi = 5$ and $Re = 1000$.

confirming that the plate oscillates in the linear regime.

3.3 Plate Deformation

We focus on the hydrodynamics of resonance oscillations. In figure 3.3, we show experimental and computational snapshots illustrating the plate bending pattern and corresponding plate curvature $\kappa(x) = z''(x)/\left[1 + z'^2(x)\right]^{3/2}$ for the internally and externally actuated plates. The plate aspect ratio is $\mathcal{A}_\mathcal{R} = 2$ and the actuation in both cases yields $\delta_t/L = 0.01$. In the case of an external actuation, the plate deformation in the z–direction grows monotonically along the plate length with the maximum at the plate free end (figure 3.3a). Such deformation is typical for resonance oscillations. This is confirmed by inspecting the plate curvature (figure 3.3b). The

curvature monotonically decreases towards the plate tip from the maximum value at the root. The application of the external force at the root yields the most significant plate bending that gradually decreases towards the tip where the curvature is zero, indicating that near the tip the plate remains straight during the entire oscillation cycle.

The resonance deformation of an internally actuated plate (figure 3.3c) is noticeably different from that of an externally actuated plate. In the case of the internal actuation, the tip of the plate displays a non-zero curvature during most of the oscillation cycle (figure 3.3d). Interestingly the maximum curvature occurs at the plate root for both types of actuation. As we discuss below, the difference in the deformation patterns between externally and internally actuated plates have a drastic effect on the plate hydrodynamics and the generated hydrodynamic forces.

We further compare the plate bending patterns for the two actuation methods in figure 3.4, where we show the simulated time histories of the plate deflection, the plate rotational angle and the plate curvature. The instantaneous tip deflection $d_t(t)$ and center of mass displacement $d_{cg}(t)$ are shown in figure 3.4a. The solid lines refer to the externally actuated case while the dotted lines refer to the internally actuated plate. The maximum tip deflection occurs at about $t/\tau = 0.5$ for both the plates, since the plates oscillate at resonance. In the case of the externally actuated plate the center of mass and the tip displacement have a phase lag of $\Delta\theta = \pi/4$, while the internally actuated plate center of mass and tip are in phase.

In figure 3.4b, we present the time history of the local plate angle α at the plate center of mass and tip. For the external actuation, we find that the angle is in phase at both locations. Therefore at the maximum tip displacement, the angle is positive yielding a slope that effectively transfers the fluid backwards and minimizes the relative motion between the plate and the fluid. On the other hand, for the internally actuated plate, the local angle shifts along the length of the plate so that

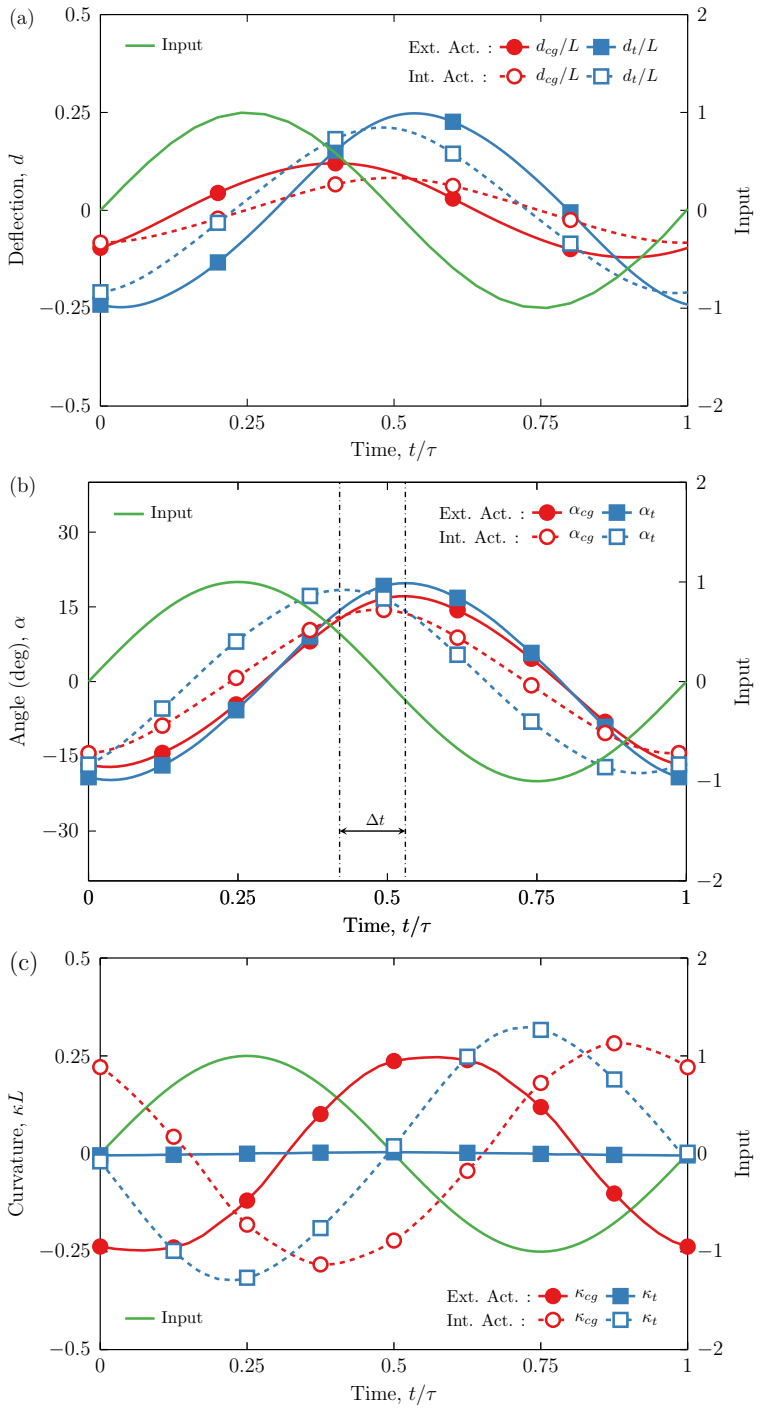

Figure 3.4: Time history of (a) the instantaneous deflection at the tip d_t and at the center of mass d_{cg}, (b) the angle at the tip α_t and at the center of mass α_{cg}, and (c) the curvature at the tip κ_t and at the center of mass κ_{cg} for numerically simulated internally and externally actuated plates with aspect ratio $\mathcal{A}_\mathcal{R} = 2$, $\chi = 5$ and $Re = 1000$ at resonance.

at the tip the angle and the deflection are out of phase. This change along the length results in relative motion between the plate and the fluid leading to a greater vorticity generation as we discuss below.

In figure 3.4c, we show the time history of the plate local curvature κ at the center of mass and at the tip. The externally actuated plate maintains zero curvature at the tip during the entire oscillation period, whereas the curvature at the center of mass is maximized at the maximum plate deflection. For the internal actuation case, the magnitude of the curvature does not decrease with the distance from the root as it happens for the externally actuated plate. Figure 3.4c shows that the curvature magnitude changes insignificantly between the center of mass location and the trailing edge. Furthermore, the maximum curvature at the tip coincides with the maximum input bending moment to satisfy the respective boundary condition.

3.4 Flow Field

In figure 3.5, we show surfaces of constant vorticity magnitude generated at resonance by externally and internally actuated plates as predicted by our simulations. Vorticity is generated as a result of the relative motion of the plate with respect to the surrounding fluid and, therefore, is the most significant along the trailing edge (TEVs) and the side edges (SEVs) of the plate. During each stroke the combination of SEVs and TEVs forms a characteristic horseshoe shaped set of vortices that are periodically shed from the oscillating plate. The horseshoe vortices sharing common features are generated by plates with both modes of actuation. However, there are also important differences in the emerging flow structures associated with their distinct bending patterns.

Several theoretical and experimental studies highlight the key role of reverse Karman streets for propulsion [77]–[79]. Both actuation patterns lead to the generation of sets of vortices with opposite rotation direction. In both instances, counterclockwise

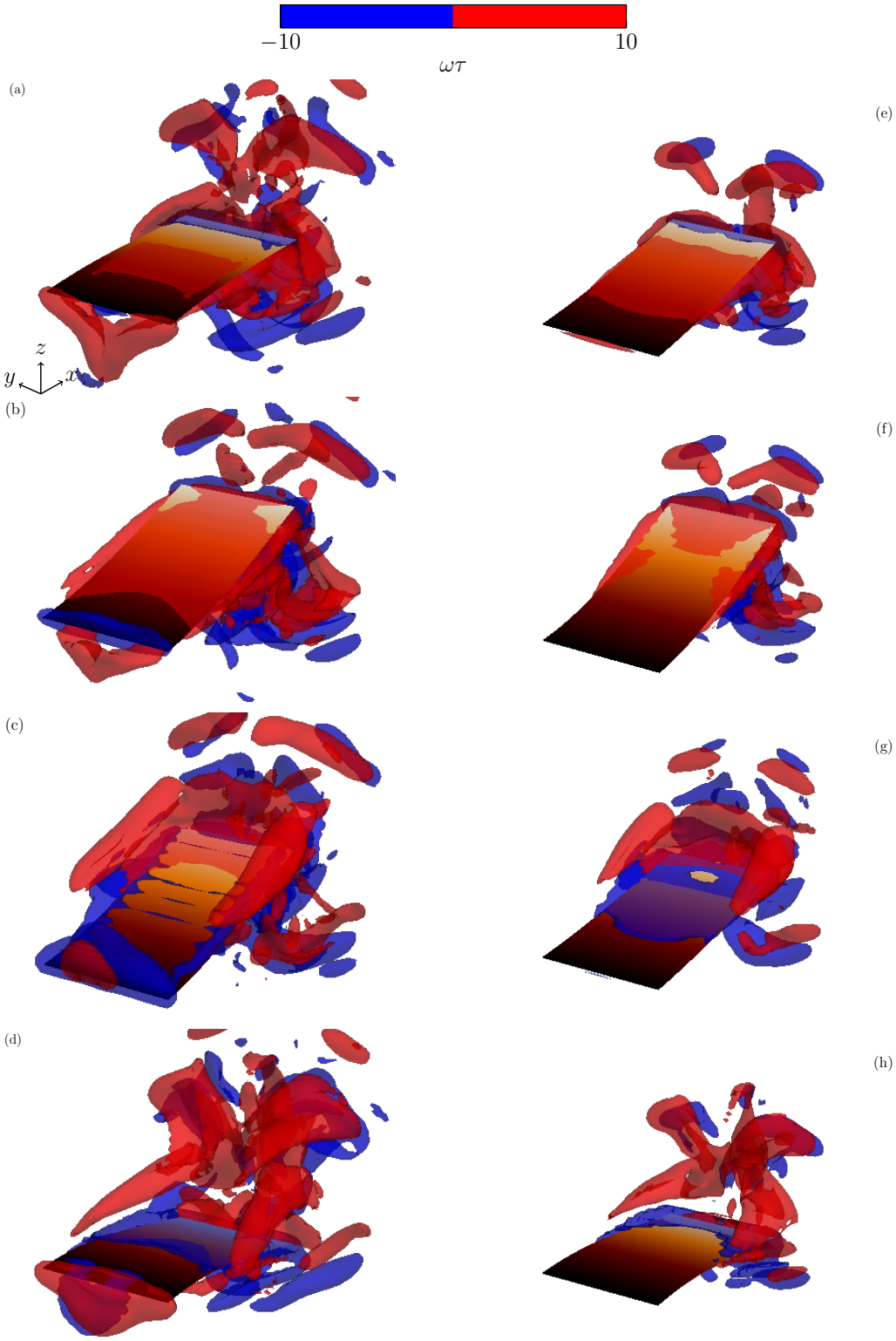

Figure 3.5: Contours of normalized vorticity $\omega\tau = \pm 10$ of the numerically simulated (a-d) externally actuated plate and (e-h) internally actuated plate with $\mathcal{A}_\mathcal{R} = 2$, $\chi = 5$, $Re = 1000$, and tip deflection $\delta_t/L = 0.25$ at resonance at times $t/\tau = 0.25, 0.5, 0.75, 1$, respectively. Vortices represented in red are rotating counterclockwise while vortices represented in blue are rotating clockwise.

vortices are shed at the top while clockwise rotating vortices are shed at the bottom. The sign of these vortices creates a jet flowing away from the tip of the plate. This configuration leads to the production of a net thrust. For the lowest actuation levels tested, the sign of these vortices flip which corresponds to a net drag force on the plate [17], [77]–[80].

When considering the external actuation, the plunging motion of the plate leading edge produces a leading edge vortex (LEV), however its strength is relatively weak compared to SEVs and TEV. Since the plate is actuated in a quiescent fluid, the LEVs shed close to the root and do not interact in the wake with TEVs and SEVs. Therefore, we do not anticipate they play an important role in the thrust production for this setup. Furthermore, SEVs extend along the entire plate length from the root to the tip. In the case of the internal actuation, the root is immobilized. As a result, the internally actuated plate does not produce LEVs, whereas significant SEVs develop only at halfway distance from the root to the tip. Thus, one can expect the externally actuated plate that displaces more fluid during each strokes would generate more vorticity compared to the internally actuated plate with comparable trailing edge displacement.

To further characterize the flow field, figure 3.6 shows simulation snapshots of the flow field around oscillating plates with different actuation types. The glyph demonstrates the alternating vortical structure shed at the tip of the plate. A downstroke generates counter-clockwise vortices, as shown in figures 3.6b, 3.6c, 3.6f, and 3.6g, whereas the upstroke generates clockwise vortices, as shown in figures 3.6a, 3.6d, 3.6e, and 3.6h. The interaction of the vortices creates a jet in the x-direction leading to a net thrust. We note that these flow structures are consistent with the literature [42].

We quantified the vorticity generated by each actuation method by computing the normalized enstrophy $\mathcal{E} = \underline{\omega} \cdot \underline{\omega}\ \tau^2$. Enstrophy is a measure of the intensity of

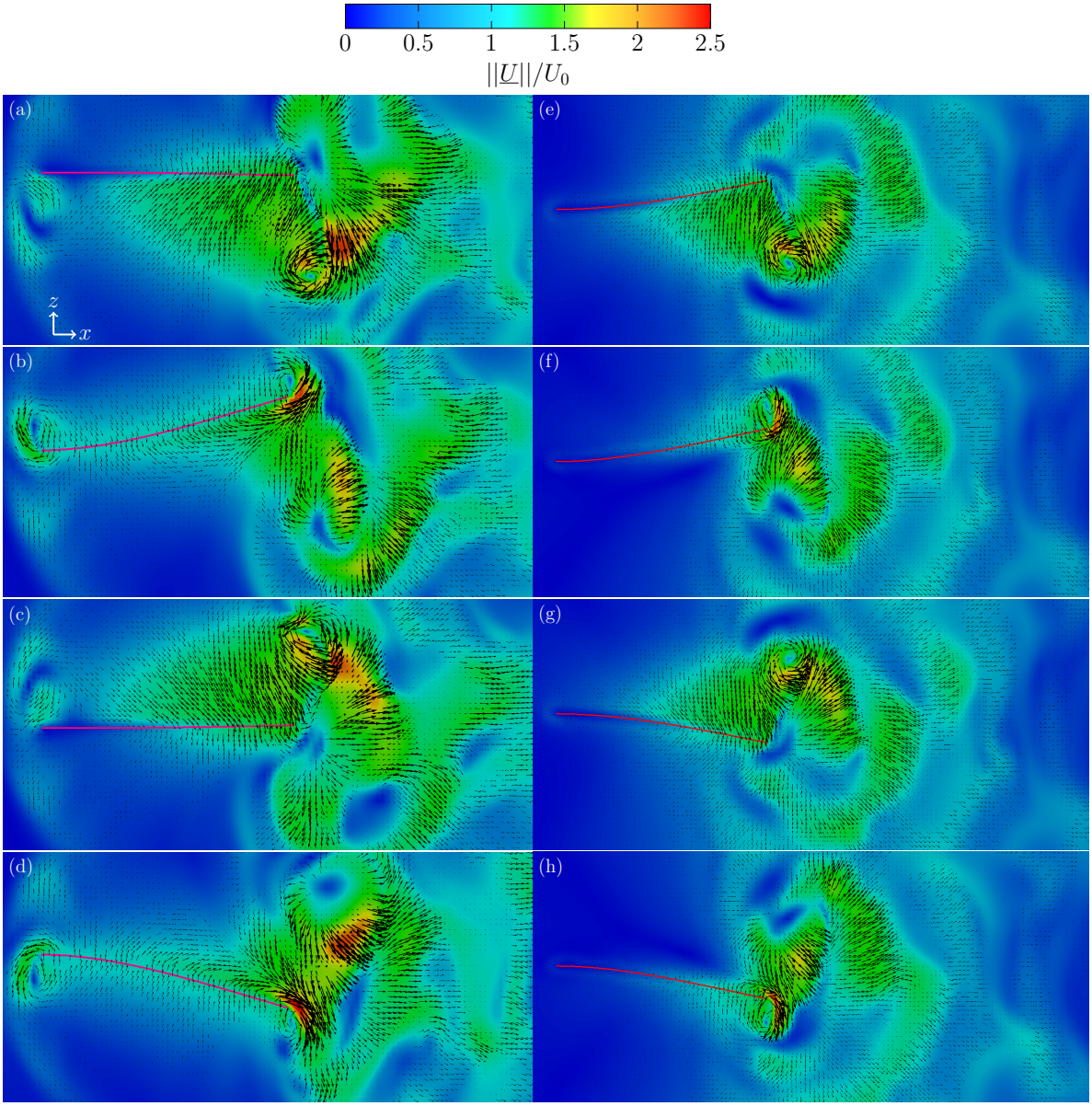

Figure 3.6: Normalized velocity magnitude $||\underline{U}||/U_0$ of the numerically simulated (a-d) externally and (e-h) internally actuated plate with $\mathcal{A}_\mathcal{R} = 2$, $\chi = 5$, $Re = 1000$, and tip deflection $\delta_t/L = 0.25$ at resonance at times (a-d) $t/\tau = 0.25, 0.5, 0.75, 1$, respectively.

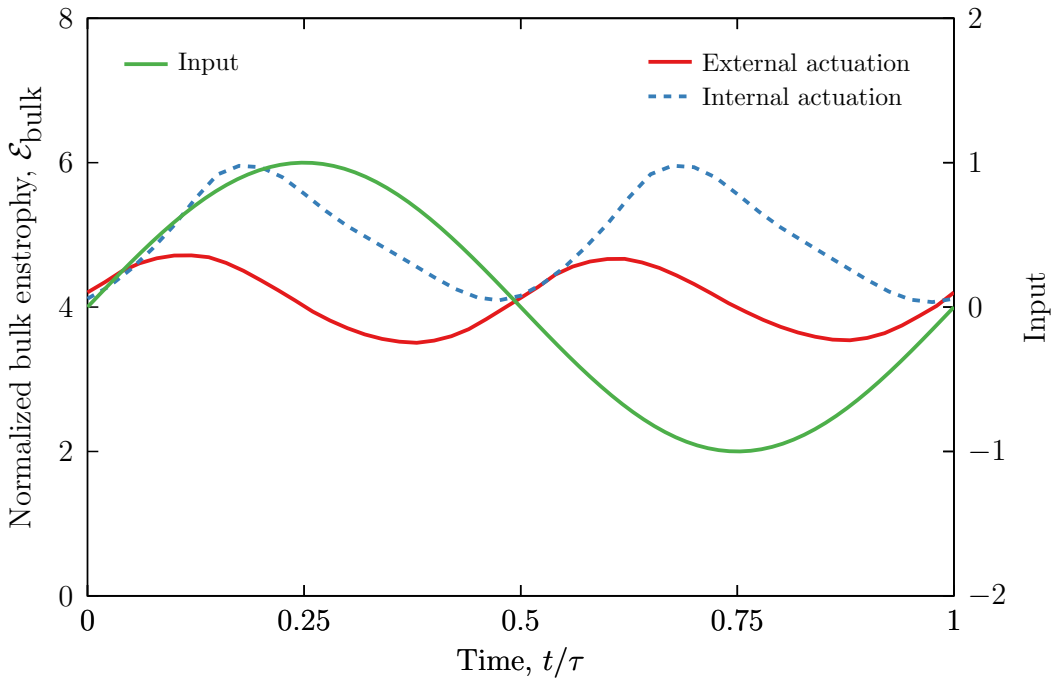

Figure 3.7: Time history of the normalized bulk enstrophy $\mathcal{E}_{\text{bulk}}$ for numerically simulated internally and externally actuated plates with $\mathcal{A}_{\mathcal{R}} = 2$, $\chi = 5$, $Re = 1000$, and tip deflection $\delta_t/L = 0.25$ at resonance.

viscous dissipation [81]. In figure 3.7, we show the time evolution of the volume averaged enstrophy over one period of plate oscillations. For both plates the enstrophy displays similar time dependent behavior with two peaks. However, the locations of the peaks are somewhat different. Compared to the plates with external actuation, the peaks for the internally actuated plate shifted towards the ends of the upstroke and the downstroke at, $t/\tau = 0.2$ and $t/\tau = 0.7$, respectively. Figure 3.7 also shows that throughout most of the oscillation period, the internally actuated plate generates noticeable greater enstrophy and, therefore, viscous dissipation compared to the externally actuated plate.

We find that, for the externally actuated plate, the maximum viscous dissipation coincides with the maximum tip deflection, whereas the minimum enstrophy corresponds to zero tip deflection (figure 3.4a). In the case of the internally actuated plate, however, enstrophy production is related to the plate curvature at the trailing edge.

Indeed, comparing figure 3.4c and figure 3.7, we find that the maxima of enstrophy are close to the maxima of tip curvature at $t/\tau = 0.25$ and $t/\tau = 0.75$, while the enstrophy minima coincide with zero tip curvature at $t/\tau = 0.5$ and $t/\tau = 1$. Thus, the "cupping" exhibited by the internally actuated plate is a major contributor causing the increased enstrophy production and, therefore, viscous dissipation.

3.5 Hydrodynamic Performance

To further investigate the difference between the two actuation methods, we examine time evolution of the hydrodynamic force generated by the plates. In figure 3.8a, we show the simulation results for the instantaneous lift force F_z over one oscillation period. The input refers to the prescribed motion at the root and the internal moment for the externally and internally actuated plates, respectively. We normalize the forces by the characteristic force based on the plate length. The externally and internally actuated plates yield comparable maximum lift. The maximum occurs close to $\pi/2$ coinciding with the phase of the maximum plate displacement at resonance. The mean lift force is zero due to the symmetry of the periodic oscillations.

The thrust force F_x generated by the plates is presented in figure 3.8b. The peak-to-peak amplitude of the thrust force is similar for both cases. The difference is, however, that the externally actuated plate generates a significantly greater period-averaged thrust compared to the internally actuated plate. The figure shows that there is almost a two fold difference in the value of the net thrust between the externally and internally plates. We relate this difference to the bending patterns shown in figure 3.3, where the negative angle at the tip or "cupping" of the internally actuated plate yields a plate shape that is ineffective for propelling fluid backwards. Thus, the externally actuated plate yields substantially greater thrust than the internally actuated plate with the same tip displacement.

To further validate our model, we show on figure 3.9 a comparison between the

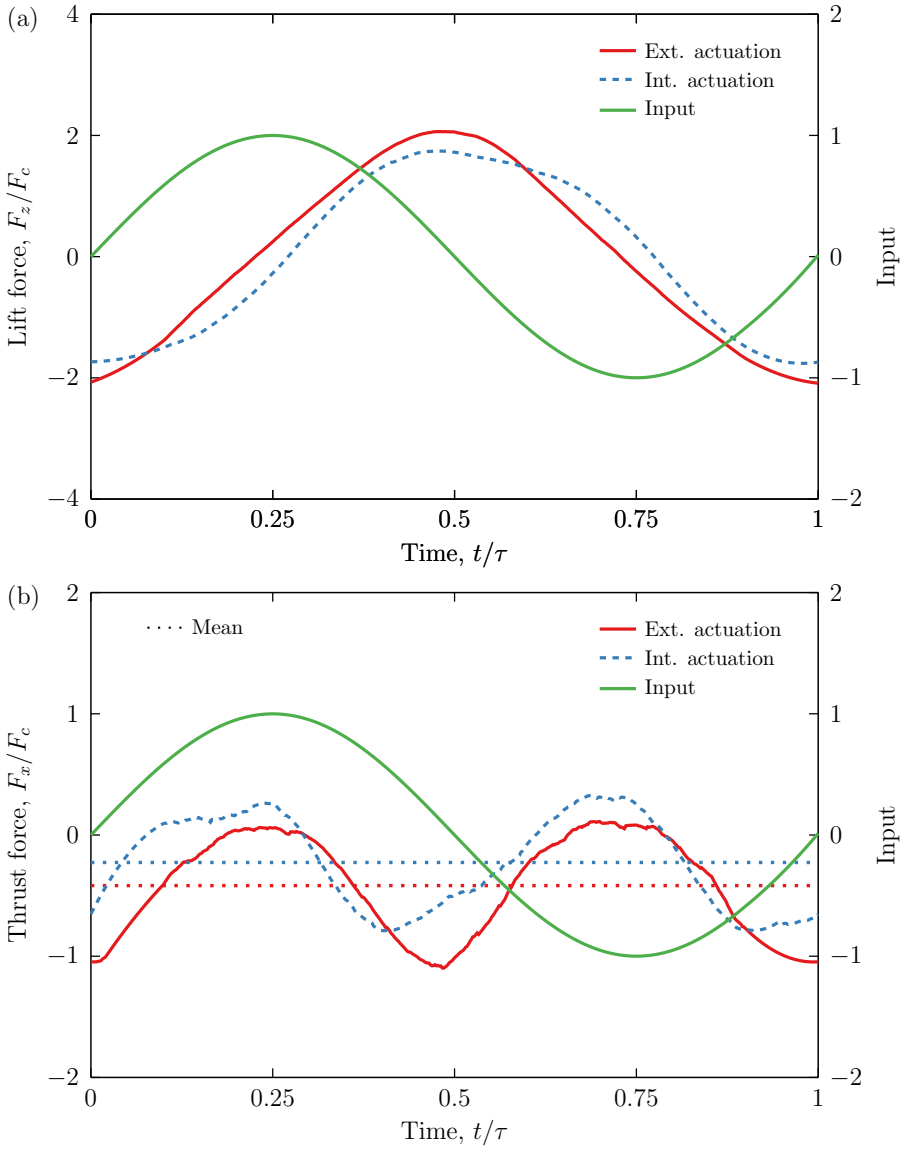

Figure 3.8: Time histories of (a) the lift force and (b) the thrust force for numerically simulated internally and externally actuated plates with $\mathcal{A}_\mathcal{R} = 2$, $\chi = 5$, $Re = 1000$ and tip displacement $\delta_t/L = 0.25$ at resonance.

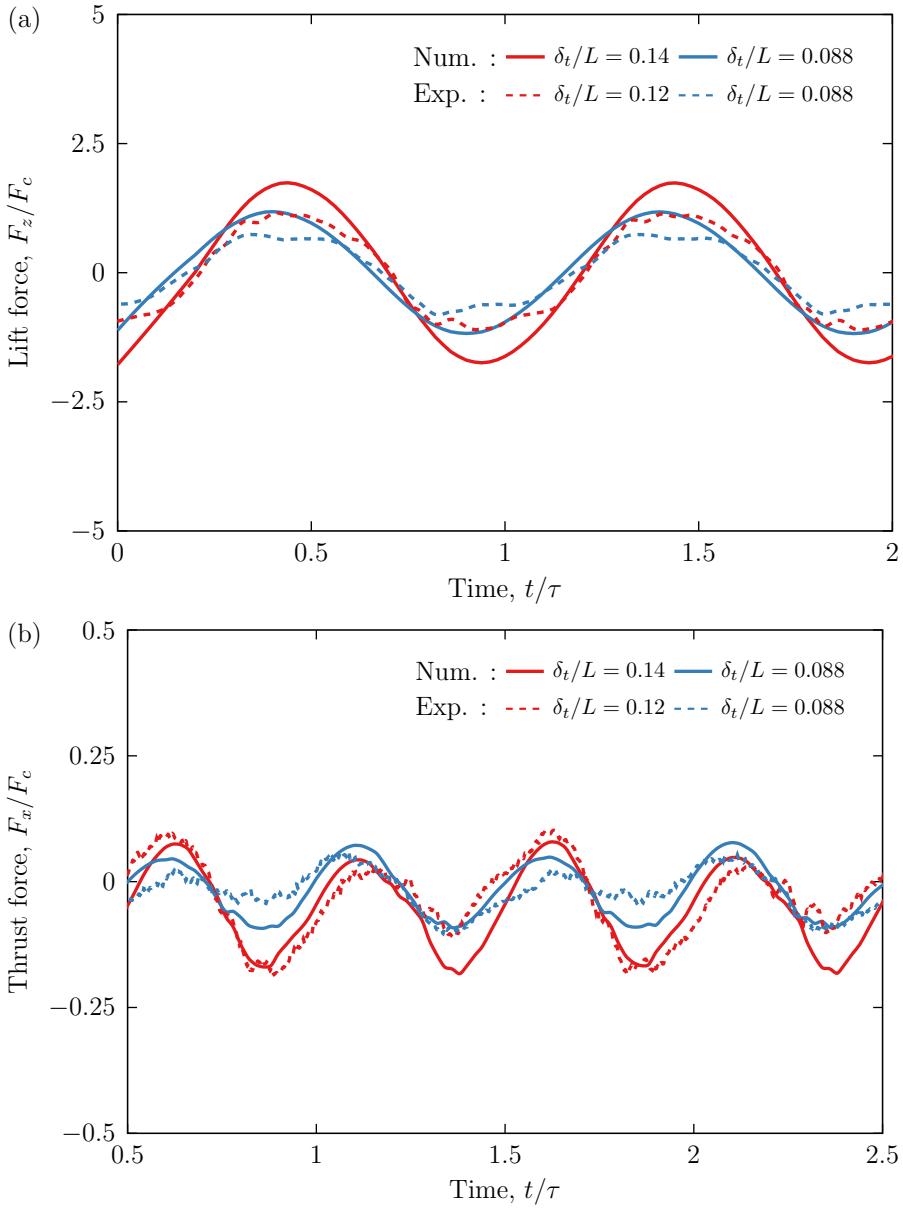

Figure 3.9: Time histories of (a) the lift force and (b) the thrust force measured numerically (solid lines) and experimentally (dashed lines) for internally actuated plates with $\mathcal{A}_\mathcal{R} = 2$, $\chi = 5$ and $Re = 1000$ at resonance.

instantaneous thrust and lift forces measured experimentally and numerically for internally actuated plates for $\delta_t/L = 0.14$ and $\delta_t/L = 0.088$. Although there is a slight deviation in the minimum thrust amplitude with experiments when $t/\tau \simeq 1.5$, we find good agreement between the experimental measurements and the numerical simulations for both the instantaneous lift and thrust.

In figure 3.10a, we plot the dependence of the mean thrust force on the tip deflection δ_t for the externally and internally actuated plates with two different aspect ratios. Overall, the normalized thrust increases with the tip deflection. Furthermore, we find good agreement with experimental results for several tip deflection tested. For relatively small δ_t/L (up to about 0.05) that roughly corresponds to the linear regime of the plate oscillations, the increase is almost linear with δ_t (see inset in figure 3.10a). For larger values of δ_t, the thrust scales as δ_t^3 indicating the influence of the non-linear effects. For the two aspect ratios tested, the externally actuated plates generate greater thrust compared to the internally actuated plates. This suggests that externally actuated plates outperform internally actuated plates independently of the aspect ratio given that they have similar trailing edge displacements.

Furthermore, for both the external and internal actuation methods, we find that wider plates with $\mathcal{A}_\mathcal{R} = 2$ produce greater thrust than more narrow plates with $\mathcal{A}_\mathcal{R} = 4$. This difference can be attributed to the effect of SEVs [51], [82]. It was shown using scaling arguments that SEVs increases with the tip displacement, but not the plate width. Therefore, for the same tip displacement a wider plate experiences a lower adverse effect of SEVs and generates more thrust per plate unit width.

The power consumption by the internally and externally actuated plates is shown in figure 3.10b as a function of the tip deflection δ_t. The power input increases monotonically with the tip deflection for both actuation methods. For small deflection amplitudes $\delta_t/L < 0.05$, the power $\overline{\mathcal{P}}$ increases proportionally to δ_t^2, whereas for larger δ_t, the power increases as δ_t^3 (see inset in figure 3.10b). We find that the wider

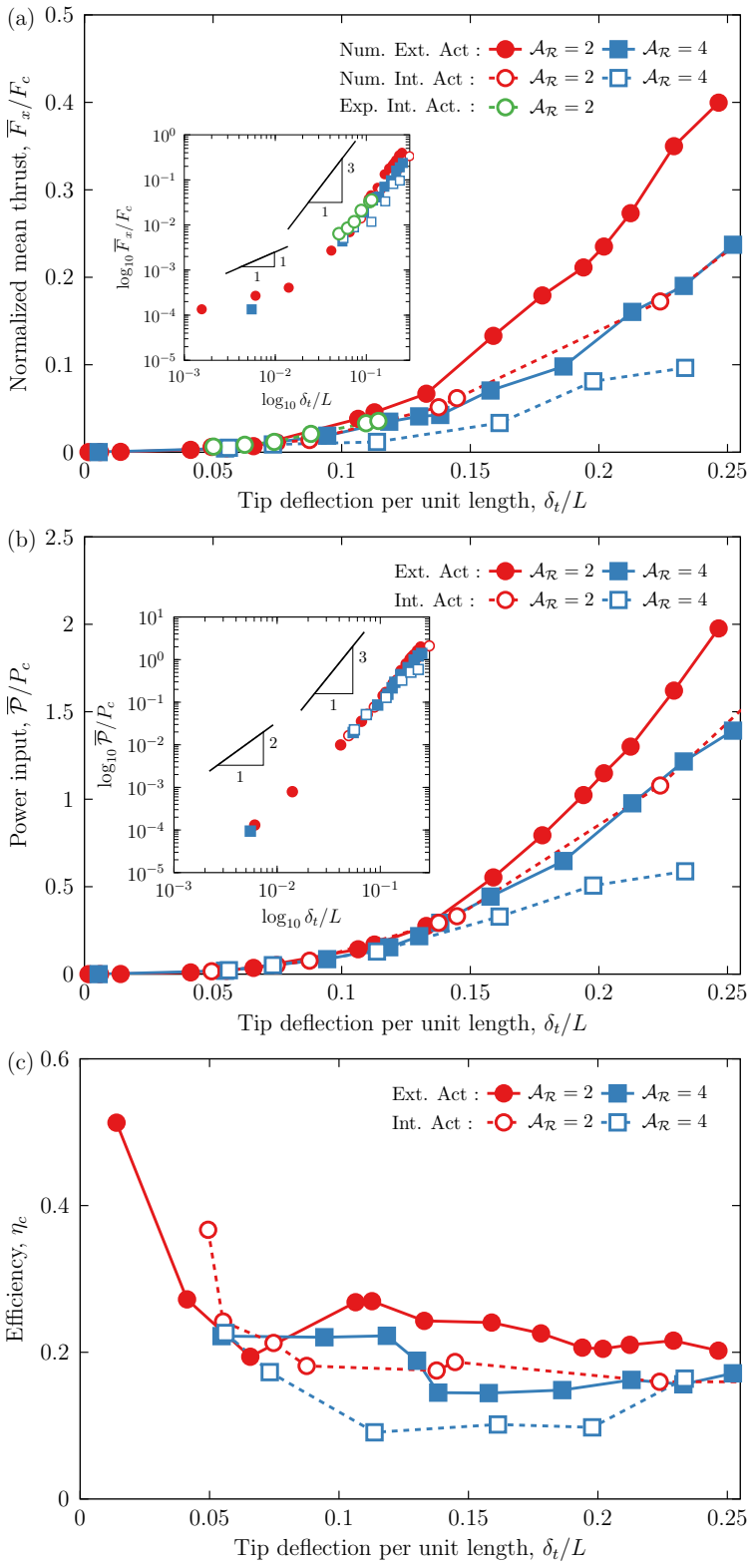

Figure 3.10: Dependence of (a) the normalized thrust $\overline{F}_x/F_c$, (b) input power $\overline{\mathcal{P}}/P_c$, and (c) efficiency η_c on the tip deflection magnitude δ_t. The simulation results are for $Re = 1000$, $\chi = 5$ and two aspect ratios $\mathcal{A}_\mathcal{R} = 2$ and $\mathcal{A}_\mathcal{R} = 4$.

plates require greater power input per unit width compared to the narrow plates independently of the actuation method. This is consistent with the higher thrust produced by the wider plates (figure 3.10a) and can be related to larger amount of fluid displaced by such plates per unit width. Furthermore, we find that externally actuated plates require greater input power to oscillate with the same tip deflection as internally actuated plates. This can be in part attributed to the additional power required by externally actuated plate to displace fluid near the oscillating plate root compared to the internally actuated plate with clamped root. Indeed, even at small levels of actuation the LEVs and SEVs have comparable sizes (figure 3.5).

To further characterize the hydrodynamic performance of oscillating plates, we compute the thrust efficiency $\eta = \frac{\overline{F}_x/F_c}{\overline{\mathcal{P}}/P_c}$ in figure 3.10c as a function δ_t. We find that the efficiency is maximized for smaller δ_t, but rapidly decreases with increasing δ_t within the linear regime. In the non-linear regime, the efficiency varies slightly with δ_t. Indeed, in the linear regime $\overline{F}_x \propto \delta_t$ and $\overline{\mathcal{P}} \propto \delta_t^2$ resulting in $\eta \propto 1/\delta_t$. For greater δ_t characterized by non-linear oscillations, both $\overline{F}_x$ and $\overline{\mathcal{P}}$ scale with δ_t^3, which in turn results in η nearly independent of δ_t. Comparing the externally and internally actuated plates, we find that the externally actuated plates exhibit higher efficiency than the internally actuated plates, except for the lowest tip deflection conditions. This is because at small δ_t the efficiency of the externally actuated plate is reduced due to the plunging motion at the root that dissipates energy but does not contribute to the thrust. For larger values of δ_t, externally actuated plates outperform internally actuated plates with the same aspect ratio. The reduced efficiency of internally actuated plates is associated with the trailing edge curvature disrupting the flow and generating an increased level of vorticity, as shown in figure 3.7. We also find that wider plates are more efficient than narrow plates for the entire range of δ_t. This is due to the lower contribution of SEVs into the overall energy budget of the wider plates.

3.6 Reynolds Number Effects

In figure 3.11, we use simulations to probe the effect of the flow regime by varying the Reynolds number for the two actuation methods. Here, we consider plates with two values of tip deflections and $\mathcal{A}_{\mathcal{R}} = 2$. In figure 3.11a, we show that the normalized thrust does not change significantly with Re. As demonstrated by [35], at high enough Re the thrust is mainly defined by the tip kinematics, supported by nearly constant thrust for higher Re. Conversely at lower Re, the tip kinematics do not fully define the thrust production. This trend persists for both types of actuation, although the externally actuated plates produce greater thrust.

In figure 3.11b, we show the evolution of the normalized power with Re. As the Reynolds number increases the normalized power decreases and remains constant at higher Re. This behavior can be attributed to the increase of viscous dissipation associated with a lower Re. To generate the same tip deflection, the plate requires more power when the viscous effects are more significant. For both tested tip deflections, the internally actuated plates consume less power compared to the externally actuated plates.

The change of the hydrodynamic efficiency of the plates with Re is shown in figure 3.11c. Over the entire range of Re we tested, the externally actuated plates outperform the internally actuated plates. The difference in efficiency is more significant for the lower tip deflection amplitude. This indicates that as the viscous effects become more important, the hydrodynamic efficiency is more sensitive to the difference in bending patterns of the internally and externally actuated plates. Conversely, at higher Reynolds number, the hydrodynamic efficiency converges to a constant value. This behavior is consistent with the potential flow solution predicting that the efficiency is set by the tip kinematics.

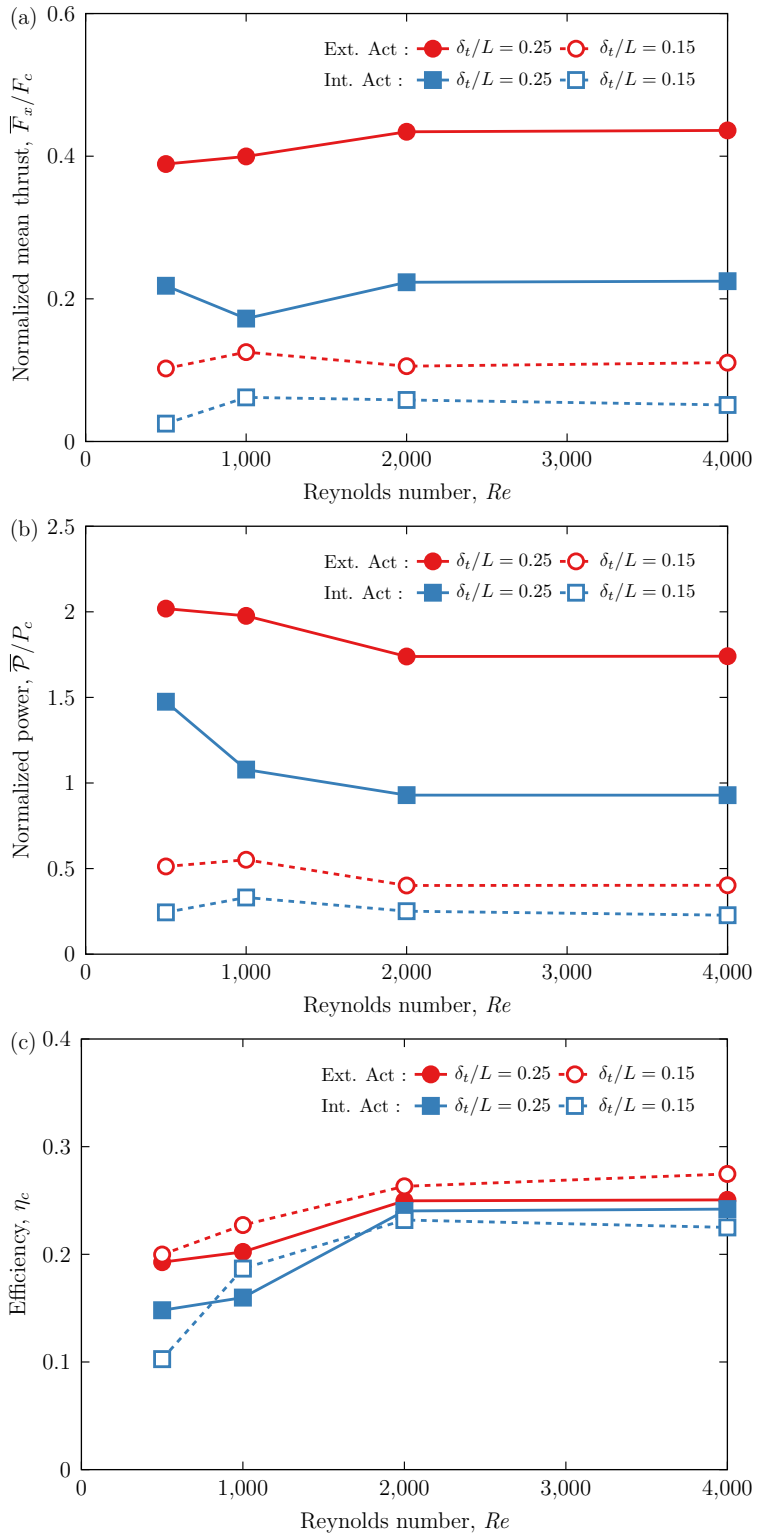

Figure 3.11: Dependence of (a) the normalized thrust $\overline{F}_x/F_c$, (b) input power $\overline{\mathcal{P}}/P_c$, and (c) efficiency η_c on the Reynolds number Re. The simulation results are for $\delta_t/L = 0.15$, $\delta_t/L = 0.25$, $\chi = 5$ and $\mathcal{A}_\mathcal{R} = 2$.

3.7 Inertia Coefficient

When the plate oscillates in fluid, the volume of displaced fluid acts as an additional mass altering the dynamics of the plate. This added mass shifts the natural frequency of the plate to lower values [83]. This effect can be characterized using an inertia coefficient $c_m = \frac{4}{\pi\chi}\left(\frac{\omega_{1,\mathrm{vac}}^2}{\omega_{1,\mathrm{f}}^2} - 1\right)$ [84]. For a given mass ratio, the inertia coefficient is a function of the frequency ratio alone. For small enough amplitudes, the inertia coefficient only depends on the plate aspect ratio, we refer to this regime as the linear regime. However, as the amplitude increases, non-linear hydrodynamic effects make the inertia coefficient a function of the aspect ratio and the tip amplitude [85]. We can rewrite equation 2.46 with an additional mass per area $\mathcal{M}$ due to the fluid moved by the plate as

$$\omega_{1,\mathrm{f}} = \frac{\lambda_1^2}{L^2}\sqrt{\frac{D}{\sigma_s + \mathcal{M}}} \ . \tag{3.1}$$

By comparing the two definitions, we can obtain

$$\frac{\omega_{1,\mathrm{vac}}^2}{\omega_{1,\mathrm{f}}^2} = 1 + \frac{\mathcal{M}}{\sigma_s} \ .$$

For plates with moderate and high aspect ratios, the added mass can be expressed as $\mathcal{M} = \frac{\pi}{4}\rho w c_m = \frac{\pi}{4}\chi\sigma_s c_m$, with c_m being the inertia coefficient. We therefore evaluate the inertia coefficient as follows

$$c_m = \frac{4}{\pi\chi}\left(\frac{\omega_{1,\mathrm{vac}}^2}{\omega_{1,\mathrm{f}}^2} - 1\right) \ . \tag{3.2}$$

In figures 3.12a and 3.12b, we show the inertia coefficient c_m for plates with, respectively, $\mathcal{A}_\mathcal{R} = 2$ and $\mathcal{A}_\mathcal{R} = 4$ as a function of the tip deflection δ_t. We find close agreement between the experiments and simulations in spite that they use different values of the mass ratio χ. As shown in the inset in figure 3.12a, the inertia coefficient

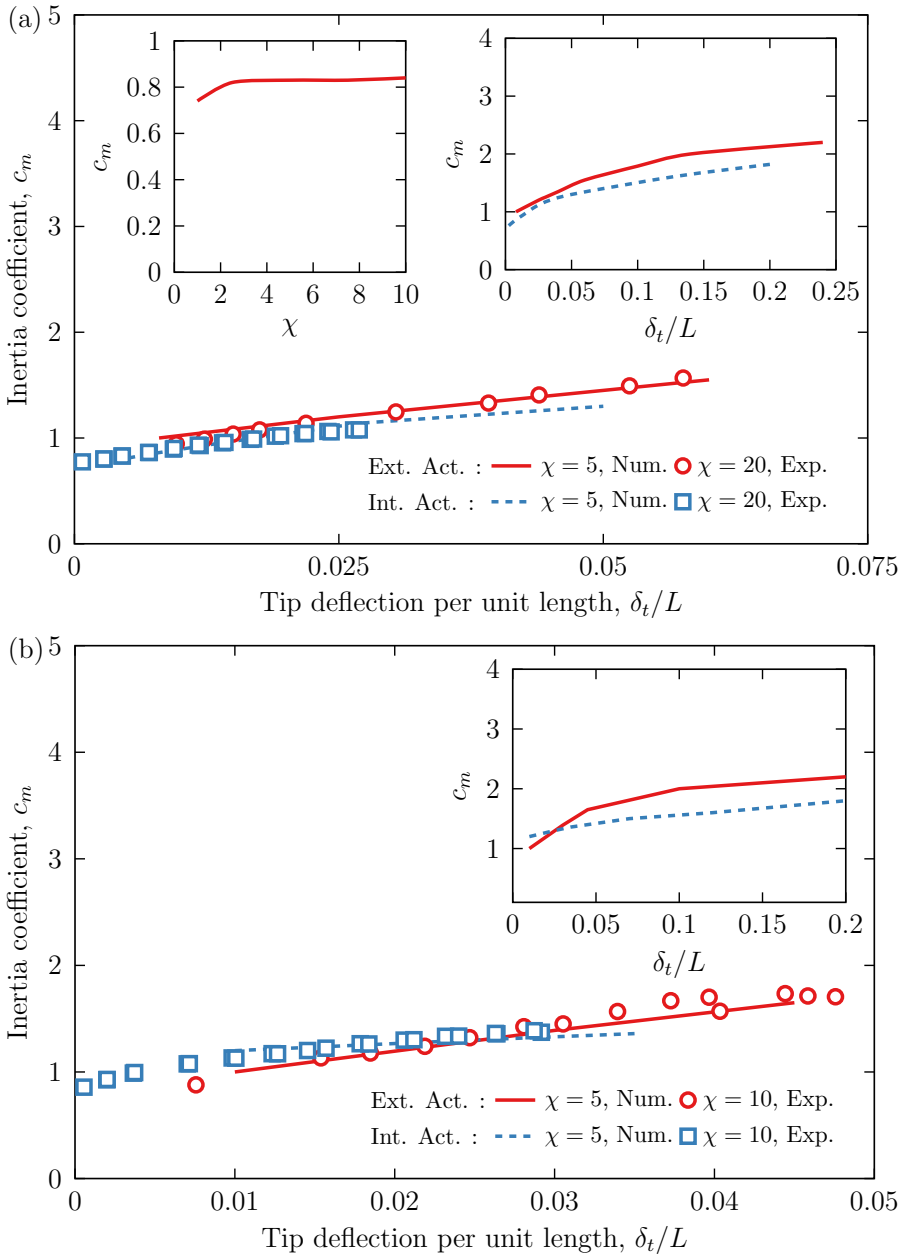

Figure 3.12: Dependence of inertia mass coefficient on the tip deflection in the linear oscillation regime of internally and externally actuated plates for $Re = 1000$, $\chi = 5$ and aspect ratios (a) $\mathcal{A}_\mathcal{R} = 2$ and (b) $\mathcal{A}_\mathcal{R} = 4$. The left inset in (a) shows the dependence of the inertia coefficient on the mass ratio for $\delta_t/L = 0.01$. The right inset in (a) and inset in (b) show the inertia coefficient for non-linear range of plate oscillations. In (a) and (b), the lines represent simulation results while the symbols represent experimental data.

is nearly independent of χ for $\chi > 2.5$. This explains good agreement between simulations and experiments in figures 3.12a and 3.12b, where the simulations are performed with $\chi = 5$, whereas the experimental plates are respectively characterized by $\chi = 20$ and $\chi = 10$.

Our experiments are limited to relatively small tip deflections about $\delta_t = 0.05$. In the simulations, we explore significantly wider range of δ_t shown in the insets in figures 3.12a and 3.12b. We find that the inertia coefficient plateaus with the increasing tip deflection, consistent for both types of actuation. Although it can be expected that the inertia coefficient is a sole function of the aspect ratio and the tip amplitude, our results show that the actuation method strongly affects c_m. Not only c_m increases with the tip amplitude, but also the difference between c_m for two actuation methods increases with δ_t. For larger δ_t, the inertia coefficient for the externally actuated plate systematically exceeds c_m of the internally actuated plate. This result is in agreement with the hydrodynamic loading acting on the plate shown in figure 3.10. The externally actuated plate produces greater hydrodynamic forces and, therefore, is characterized by a higher inertia coefficient than the internally actuated plate.

In figure 3.13, we show the inertia coefficient c_m and normalized mean thrust $\overline{F}_x/\overline{F}_{\text{Lighthill}}$ for the wider plate $\mathcal{A}_\mathcal{R} = 2$ in the non-linear regime ($\delta_t/L = 0.05$) as a function of Re. The dot-dashed line is drawn from potential flow theory. In this figure the mean thrust is normalized by the mean thrust predicted by the inviscid theory. Our results show that as Re increases the numerical results asymptotically approach the analytical inviscid solution. As Re increases viscous effects become less prominent and affect a region closer to the plate. Ultimately, in the limit of $Re \longrightarrow \infty$ the inertia coefficient asymptotically reaches unity.

Simulation results are compared to Lighthill's inviscid theory which relies solely on tip kinematics to predict the mean thrust. Mirroring the behavior of c_m, as Re increases simulation results approach the analytical prediction asymptotically. In

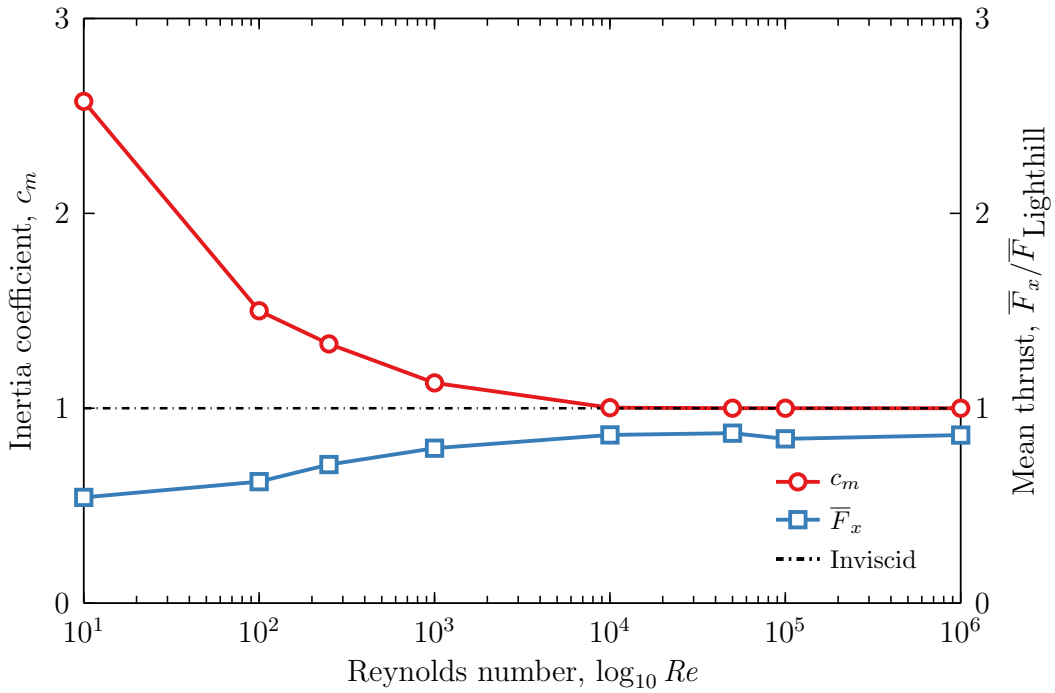

Figure 3.13: Dependence of the inertia coefficient and mean thrust on the Reynolds number for $\delta_t/L = 0.05$ and $\chi = 5$. The dot-dashed line represents the analytical results from Lighthill's theory in the inviscid limit.

agreement with Lighthill's prediction, simulation results show that in the inviscid limit, the tip kinematics almost completely characterize the thrust generated by the plate.

3.8 Summary

We systematically investigate and compare the hydrodynamics of elastic plates oscillating in an incompressible Newtonian fluid subjected to two distinct actuation methods. We probe the resonance oscillations in linear and non-linear regimes of an externally actuated plate and a plate with an internal actuation. We pinpoint the critical differences in their bending patterns leading to different hydrodynamics performances. Specifically, the internally actuated plates display "cupping" of the trailing edge due to a non-zero plate curvature induced by the internal bending moment. Furthermore, internally actuated plates exhibit a phase change of the

plate angle along the plate length. Conversely, externally actuated plates have a zero curvature at the tip and an in-phase plate angle along the entire plate length. We show that this difference in bending pattern between internally and externally actuated plates leads to greater vorticity production by internally actuated plates and therefore enhances the viscous dissipation.

We find that for the same level of trailing edge displacement externally actuated plates outperform internally actuated plates in terms of the generated thrust and consumed power. Furthermore, plates with external actuation are more efficient than plates with internal actuation with exception of the smaller tip amplitudes, in which the efficiency of the externally actuated plates is limited due to the root displacement. For both actuation methods, we find that wider plates outperform more narrow plates due to the adverse effects of the side edge vortexes. Additionally, we also probe the effect of the actuation method on the plate inertia coefficient and find that the inertia coefficient is insensitive to the mass ratio for ratios greater than 2.5. In the linear oscillation regime, both actuation methods are characterized by similar values of the inertia coefficient. However, for larger tip deflections, the inertia coefficient of the externally actuated plate significantly exceeds that of internally actuated plates, which is related to the greater hydrodynamic forces experienced by the externally actuated plates. Thus we show that the inertia coefficient is not only a function of the aspect ratio and tip deflection, but also the actuation pattern.

We show that in the range $500 < Re < 4000$, the Reynolds number has minor influence on the thrust generated by the plate. We find that the plate kinematics defining the thrust production does not change significantly in this Re range. Conversely, Re impacts the power and, therefore, hydrodynamic efficiency of the plate. At lower Re, viscous effects increase the input power that, in turn, negatively affects the efficiency. Increasing Re also leads to a decrease of the inertia coefficient that converges to unity for higher Re. This behavior is consistent with analytical

solution for an inviscid fluid. We find that these trends prevail for both actuation method. Nevertheless, for lower Re the dependence of the plate hydrodynamics on the actuation method is more critical.

The results of our study provide useful guidelines for designing efficient biomimetic underwater robotic vehicles that utilize internally actuated propulsors such as piezoelectric actuators. Piezoelectric actuators are highly attractive due to a high degree of control over the bending pattern including a combined twisting-bending motion, large amplitude actuation, silent operation, and the ease of interaction into robotic swimmers. Our study points to the need for improving the efficiency of internally actuated propulsors to match or exceed the efficiency achievable with externally actuated elastic fins.

CHAPTER 4
HYBRID ACTUATION

4.1 Introduction

In this chapter we investigate how simultaneously actuating a thin elastic plate internally and externally can improve the propulsion performance. The aspect ratio is fixed $\mathcal{A}_{\mathcal{R}} = 2.5$. The external actuation is imposed at the plate base leading to harmonic heaving oscillations $A(t) = A_0 L \sin(\omega t)$, where A_0 is the dimensionless heaving amplitude. The plate internal actuation is due to a distributed harmonic bending moment $M(t) = M_0 D \frac{L}{W} \sin(\omega t + \phi)$, where M_0 is the dimensionless moment amplitude and ϕ is the phase lag between the external and internal actuation (Figure 4.1). Note that M_0 represents the magnitude of static tip deflection of the plate due to the distributed bending moment. The external and internal actuation share the same angular frequency $\omega = 2\pi/\tau$. We set $\omega = \omega_{res}$ leading to a Reynolds number $Re = 1000$, with ω_{res} being the fundamental resonance frequency of the plate in fluid [76]. To explore the hydrodynamics of combined actuation, we fix the external actuation amplitude $A_0 = 0.1$ while varying the internal moment amplitude M_0 and the phase lag ϕ. As a reference configuration of the propulsor, we use an externally actuated plate with $A_0 = 0.1$ characterized by the constrained plate efficiency $\eta_{r,c} = 0.234$, free swimming efficiency $\eta_{r,f} = 0.632$, velocity $U_r/U_c = 0.6$, thrust $F_r/F_c = 0.312$, and power $\mathcal{P}_r/P_c = 1.333$. This reference configuration allows us to directly compare the performance of propulsors with combined actuation with that of an externally actuated propulsor.

We find that the hybrid combined actuation significantly outperforms either single actuation methods in both propulsion and efficiency. This enhanced performance is

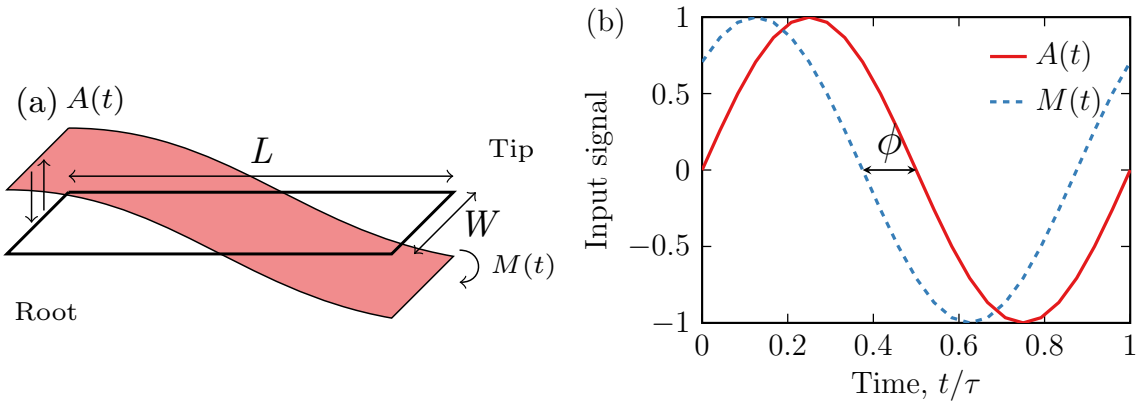

Figure 4.1: (a) Schematic of an oscillating elastic plate with length L, width w, and thickness $h \ll L$. The plate is actuated by a heaving motion at the base $a(t)$ and by a distributed internal bending moment $m(t)$. (b) Plate actuation signals with a phase lag ϕ.

due to the hybrid actuation's capacity to maintain relatively high thrust output while minimizing viscous losses. This balance is associated to moderately high tip displacement accompanied by a relatively low center of mass displacement. Furthermore, we show that the phase lag between the actuation signals allows to directly control the propulsion and energetic regimes.

4.2 Hydrodynamic Performance

Figure 4.2a shows the variation of the thrust $\overline{F}_x$ for the constrained plate and the swimming velocity $\overline{U}$ for the free swimming plate with the phase ϕ. We find that these two propulsion metrics are strongly correlated indicating that either can be used to characterize the plate propulsion. The propulsion is maximized when the external actuation and the internal actuation are nearly in phase at $\phi = \pi/12$, and is minimized when the actuation signals are in phase opposition about $\phi = 11\pi/12$. Compared to the externally actuated reference case, the combined actuation with $M_0 = 0.1$ doubles the propulsion, whereas using $M_0 = 0.05$ increases the propulsion by about 50%. The propulsion with combined actuation increases to nearly 7 times of the reference case with $M_0 = 0.65$ (see the inset in figure 4.2a). For $M_0 > 0.5$ the

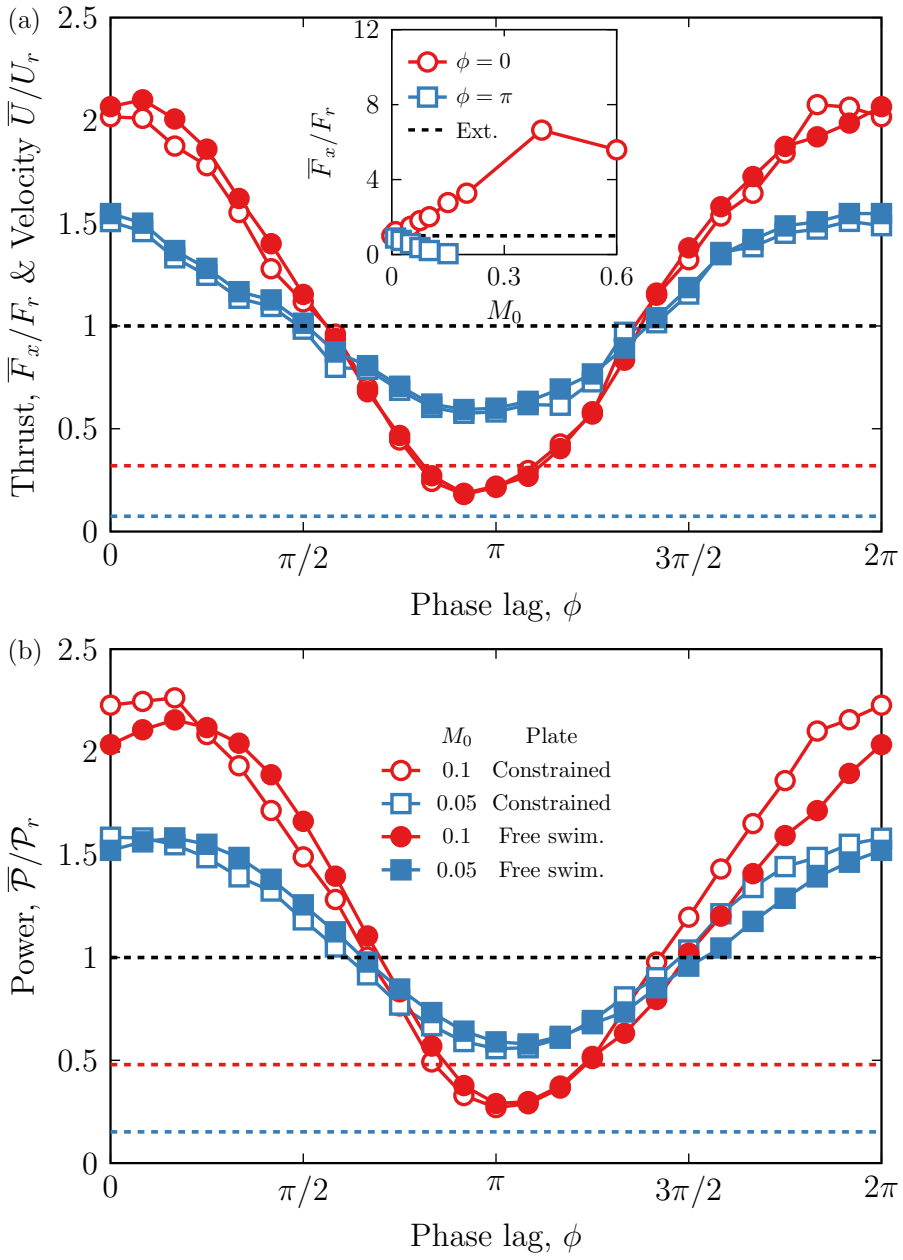

Figure 4.2: (a) Normalized thrust $\overline{F}_x/F_r$, velocity $\overline{U}/U_r$ and (b) power as a function of the phase difference between the internal and external actuation ϕ. The inset in (a) shows the maximum and minimum values of $\overline{F}_x/F_r$ as a function of M_0. The horizontal dashed lines show the (a) thrust and (b) power for internally actuated plates with $M_0 = 0.1$ (the red lines) and $M_0 = 0.05$ (the blue lines).

free end cupping negatively affects the swimming performance of combined actuation decreasing the propulsion. When the plate is actuated out of phase the combined actuation can reduce the propulsion to nearly zero. Note that the internal actuation alone with, respectively, $M_0 = 0.1$ and $M_0 = 0.05$ yields thrust that is only about 50% and 10% of that of the externally actuated plate. Thus, the combined actuation not only enables wide control over the propulsion, but can yield propulsion that significantly exceed the sum of the propulsion of the plates with separate external and internal types of actuation.

As shown in figure 4.2b the power exhibits dependence on ϕ that is similar to that of the propulsion. The combined plate yields up to twice as much power as the externally actuated plate for $M_0 = 0.1$ and up to 50% more for $M_0 = 0.05$. In comparison, the internally actuated plate yields 50% less power for $M_0 = 0.05$ and 80% less for $M_0 = 0.05$. Similarly to the propulsion, we can infer the power scales almost linearly with the internal moment when combined with the external actuation. The power is maximized at $\phi = \pi/6$ and minimized at $\phi = \pi$. The maximum power of the plate with combined actuation significantly exceeds the cumulative power of plates with separate external and internal actuation. Furthermore, the combined actuation can greatly reduce $\overline{\mathcal{P}}$ compared to the externally actuated plate.

The trailing edge displacement d_t is a major parameter that controls the plate propulsion [77]. Figure 4.3a shows the propulsion metrics as a function of d_t. We find that there is a direct relationship between the velocity and thrust data and the trailing edge displacement. This direct relationship between the propulsion and tip displacement explains the mechanism modulating the propulsion by the phase lag; when the external and internal actuation are in phase ($\phi = \pi/12$), the tip displacement and therefore the propulsion is maximized. Conversely when the internal actuation is countering the external actuation, the tip displacement ($\phi = 11\pi/12$) and therefore the propulsion is minimal. Interestingly, the data for externally actuated

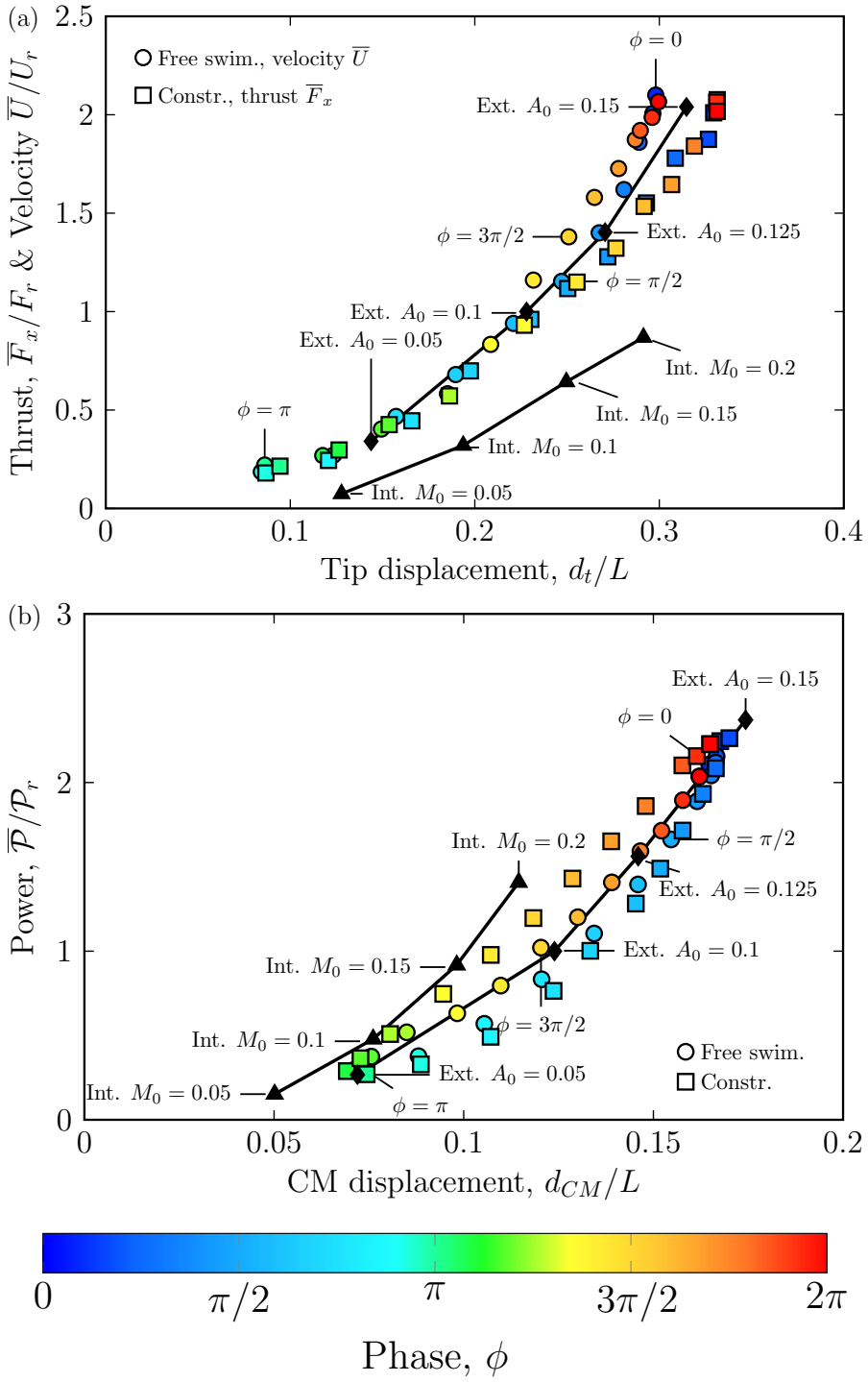

Figure 4.3: (a) Dependence of the thrust $\overline{F}_x$ and velocity $\overline{U}$ on the amplitude of the tip displacement d_t for $M_0 = 0.1$. (b) Dependence of the power $\overline{\mathcal{P}}$ on the amplitude of the plate center of mass displacement d_{CM} for $M_0 = 0.1$. The solid lines with symbols show the constrained external (diamonds) and internal (triangles) actuation with different amplitudes of A_0 and M_0.

plates with different actuation amplitudes closely matches the results for the plate with combined actuation. On the contrary, internally actuated plates with varying M_0 yield significantly lower performance than the combined actuation for comparable tip displacements. This is consistent with previous results [86] and can be attributed to the sub-optimal bending pattern of internally actuated plates. Thus, in the case of combined actuation the phase ϕ controls the tip displacement which in turn defines the propulsion characteristics.

As shown in figure 4.3b, the power $\overline{\mathcal{P}}$ scales with the displacement of the plate's center of mass d_{CM}. The power consumption is minimized with the reduced center of mass (CM) displacement and gradually increases with increasing d_{CM}. The plates with the combined actuation and the external actuation show similar dependencies, whereas the internally actuated plate requires a slightly greater power for the same CM deflection. At low center of mass displacement, the combined and single actuated plates yield minimal power consumption. Although the power consumption monotonically increases with the center of mass displacement in every case, the internal actuation once more stands out. For the same center of mass displacement the internally actuated plate consumes more power than both the external and combined actuation. The inherent difference once again lies in the slightly different kinematics generated by the internally and externally actuated plates [86]. The direct relationship between CM and power further clarifies the mechanism allowing the combined actuation to modulate the power consumption. Whenever the external and internal actuation are in phase, the combined actuation yields significantly more center of mass displacement which in turns translates into more power input. Conversely, when the actuation methods are in phase opposition, the center of mass displacement is minimized which in turn minimizes the power input. Note that d_t and d_{CM} for the plates with combined actuation are maximized when the external and internal actuation act in phase $\phi = 0$ and minimized when they are in phase opposition $\phi = \pi$.

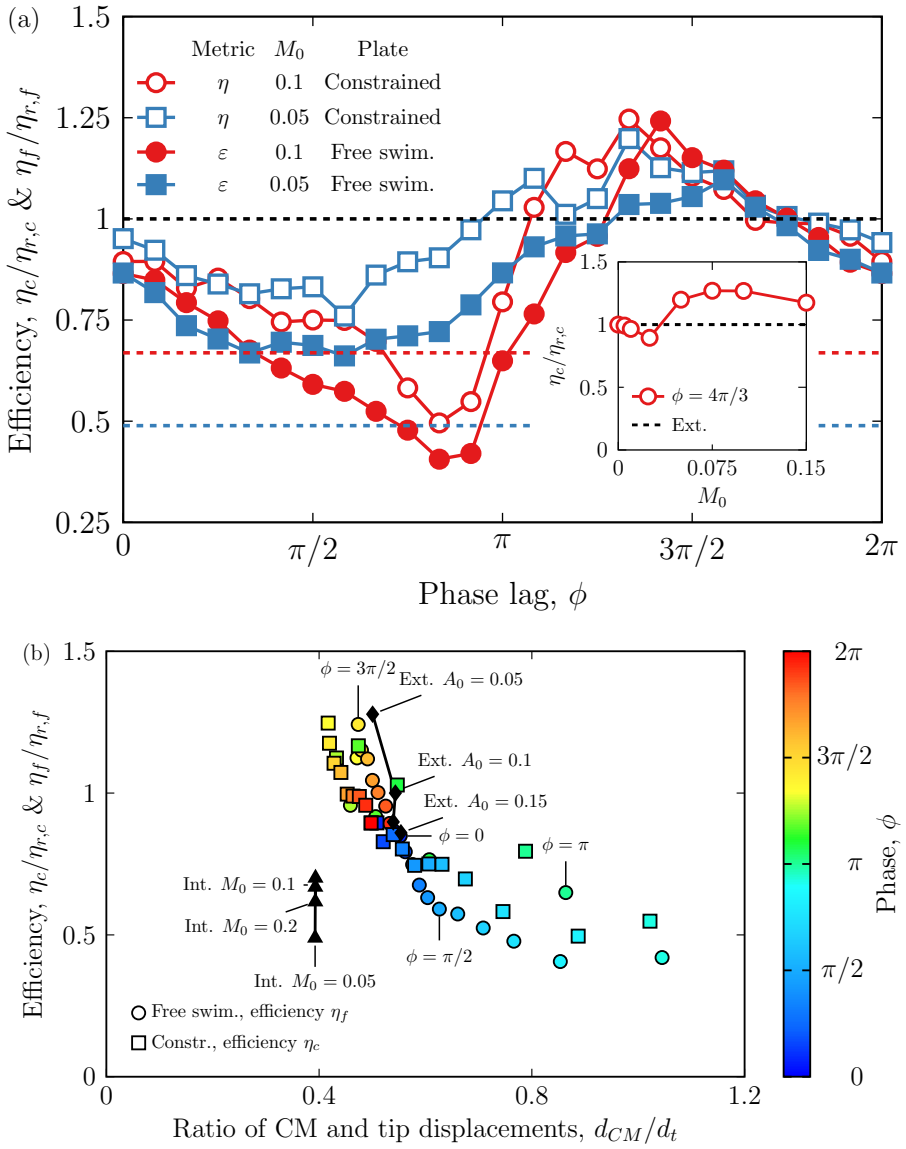

Figure 4.4: (a) Normalized constrained efficiency $\eta_c/\eta_{c,r}$ and free swimming efficiency $\eta_f/\eta_{f,r}$ as a function of the phase difference ϕ. The inset shows the maximum efficiency as a function of M_0. The horizontal dashed lines show the efficiency of internally actuated plates with $M_0 = 0.1$ (the red lines) and $M_0 = 0.05$ (the blue lines). (b) Dependence of the efficiencies η_c and η_f on the ratio between the center of mass and tip deflections d_{CM}/d_t for $M_0 = 0.1$. The solid lines with symbols in (b) show the constrained external (diamonds) and internal (triangles) actuation with different amplitudes of A_0 and M_0.

In figure 4.4a we show the efficiencies η_c and η_f for, respectively, constrained and free swimming plates with combined actuation. Both these parameters reveal a similar dependence on ϕ. More importantly, the efficiency can significantly exceed the value characterizing the plate with the external actuation. The maximum efficiency of the combined actuation is about 25% greater than that of the externally actuated plate. The phase difference $\phi = 4\pi/3$ leading to this actuation regime is nearly independent of M_0. The enhancement of the efficiency is maximized when $M_0 \simeq 0.075$ as shown in the inset in figure 4.4a. When $M_0 < 0.04$, the efficiency decreases below the reference value. In this M_0 range, the increased power due to the internal actuation outweighs its benefit for the propulsion. For greater M_0, the internal actuation translates into a significant increase of the plate efficiency up to $M_0 \simeq 0.1$. Further increase of M_0 yields a less efficient propulsion due to the tip cupping.

The efficiency represents the ratios of the propulsion metrics and the power. Since the propulsion and the power are proportional to, respectively, d_t and d_{CM}, in figure 4.4b we plot η_c and η_f as a function of d_{CM}/d_t. Indeed we find that the data for the plates with combined actuation clusters closely showing a decreasing trend with increasing d_{CM}/d_t. Thus, for an efficient propulsion the bending patterns need to have low d_{CM} and high d_t, whereas plate oscillations in which d_{CM} increases with respect to d_t result in less efficient propulsion. For plates with independent internal and external actuation, we find that d_{CM}/d_t changes only slightly with the amplitude since at resonance the bending pattern weakly depends on the oscillation amplitude.

Note that for the plates with internal actuation only, d_{CM}/d_t is relatively small compared to externally actuated plates and about the same value as the lowest d_{CM}/d_t obtained with the hybrid actuation. Nevertheless, these propulsors show a low efficiency due to the sub-optimal tip bending. Thus, having low d_{CM}/d_t is insufficient for efficient locomotion. In figure 4.5, we show the efficiency as a function of the ratio θ/β between the tip angle at the maximum velocity θ and the base angle $\beta = \arctan \frac{\omega A_0 L}{U}$.

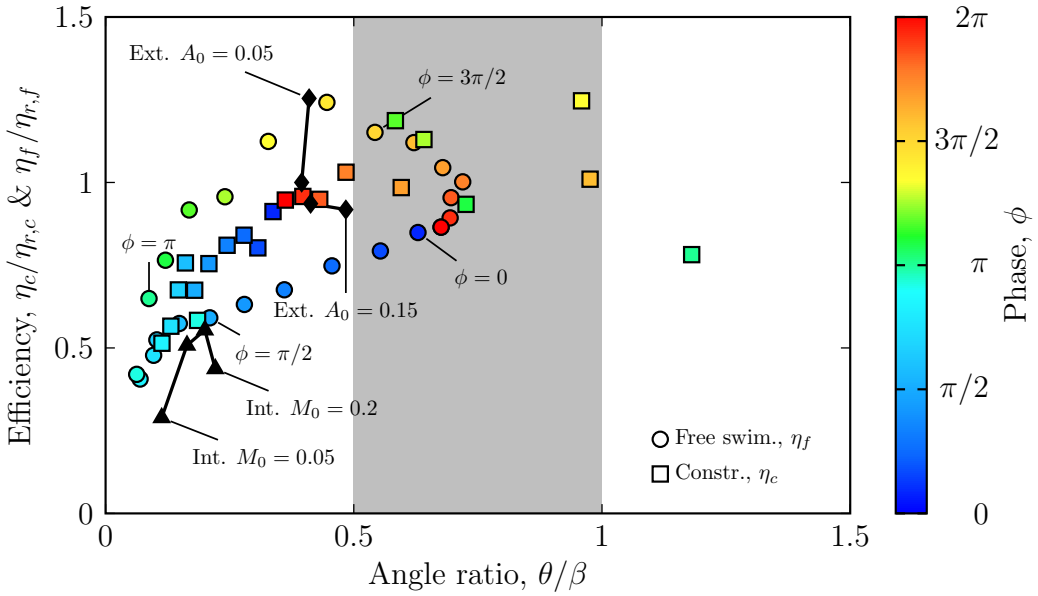

Figure 4.5: Normalized constrained $\eta_c/\eta_{c,r}$ and free swimming $\eta_f/\eta_{f,r}$ efficiency as a function of the angle ratio θ/β.

Note that for the constrained plate, β is ill-defined since $U = 0$, therefore we assume that the cruising velocity can be approximated by the tip velocity $U \simeq V_t$ and as a consequence $\beta = \arctan \frac{\omega A_0 L}{V_t}$. For efficient swimming, θ/β should be in the range between 0.5 and 1 [87]. Indeed, as θ/β increases, the tip of the plate aligns with the flow which in turn leads to a more favorable distribution of the hydrodynamic forces. Conversely when $\theta > \beta$, propulsion turns inefficient due to flow separation occurring before the plate's tip. We find that the externally actuated plates and the plates with hybrid actuation showing high efficiency are indeed close to the efficient $\theta \simeq \beta$ range. The internally actuated plates, on the other hand, have θ/β that are much lower than the optimum range confirming that the low efficiency is due to the bending pattern with a sub-optimum tip angle.

Overall, the propulsor performance is enhanced when both the efficiency and propulsion are maximized. In figure 4.6 we show the relationship between the efficiency and the propulsion. For the plate with the external actuation, the efficiency decreases with increasing propulsion. Thus, one needs to compromise with either hav-

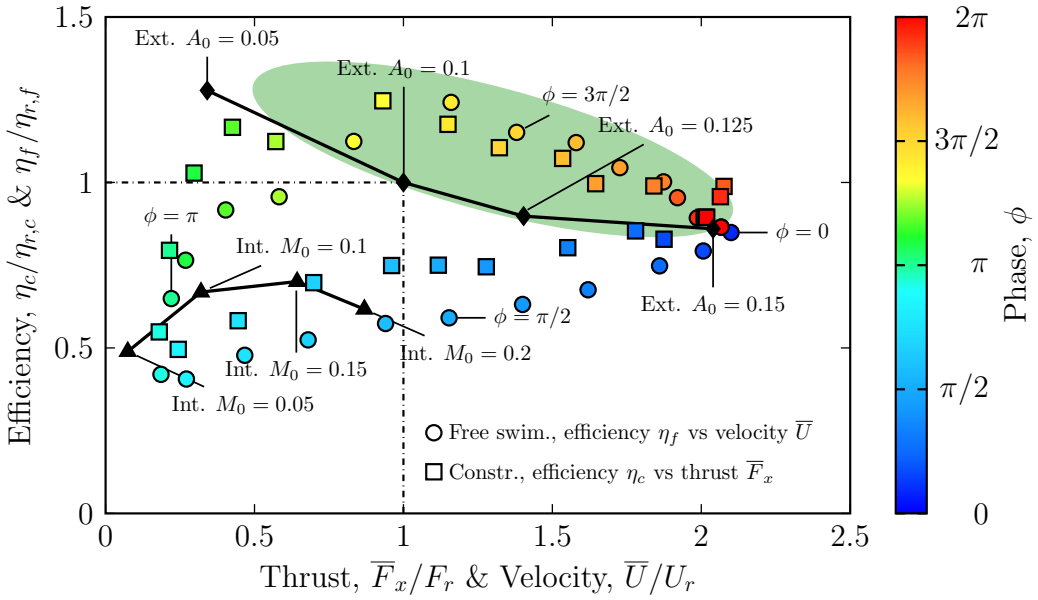

Figure 4.6: Dependence of the efficiencies η_c and η_f on the thrust $\overline{F}_x$ and velocity $\overline{U}$ for $M_0 = 0.1$. The solid lines with symbols show the constrained external (diamonds) and internal (triangles) actuation with different amplitudes of A_0 and M_0.

ing a propulsor that maximizes its efficiency or propulsion. Although the internally actuated plate performs poorly compared to the plate with the external actuation, the plate with a combination of the external and internal actuation yields a propulsors that significantly outperforms the externally actuated plate by both characteristics simultaneously, as indicated by the green ellipse in figure 4.6. Note that the combined actuation yields up to 60% greater propulsion for the same efficiency and is 25% more efficiency for the same propulsion output compared to the plate with the external actuation.

4.3 Bending Patterns

In figure 4.7, we examine the bending pattern and the hydrodynamics of plates with combined actuation at the maximum efficiency ($\phi = 4\pi/3$), maximum propulsion ($\phi = 0$) and minimum power ($\phi = 11\pi/12$). At the maximum propulsion the palate exhibits a typical bending pattern for actuation at resonance that maximizes the tip

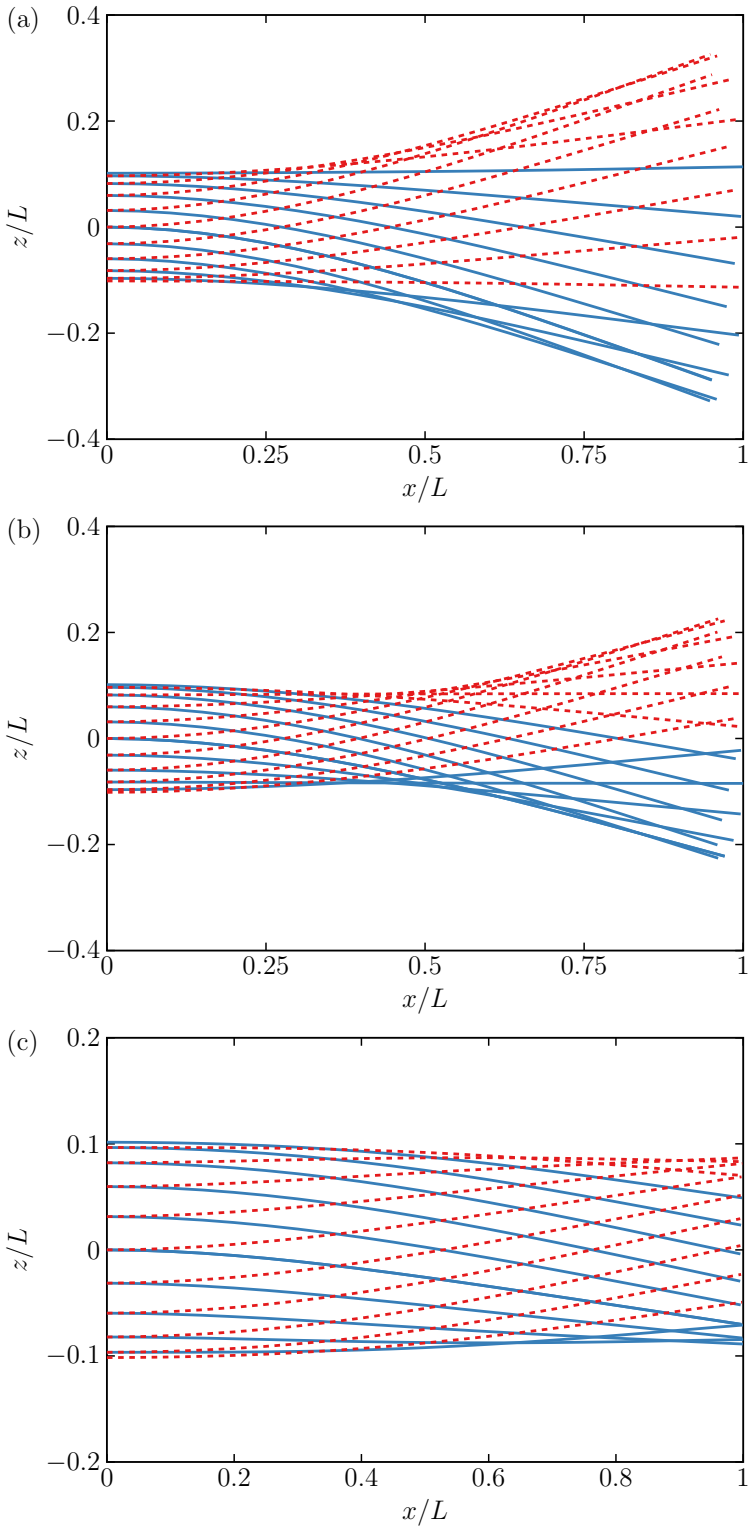

Figure 4.7: Bending pattern of a plate with combined actuation at the (a) maximum thrust ($\phi = 0$), (b) maximum efficiency ($\phi = 4\pi/3$) and (c) minimum power ($\phi = 11\pi/12$).

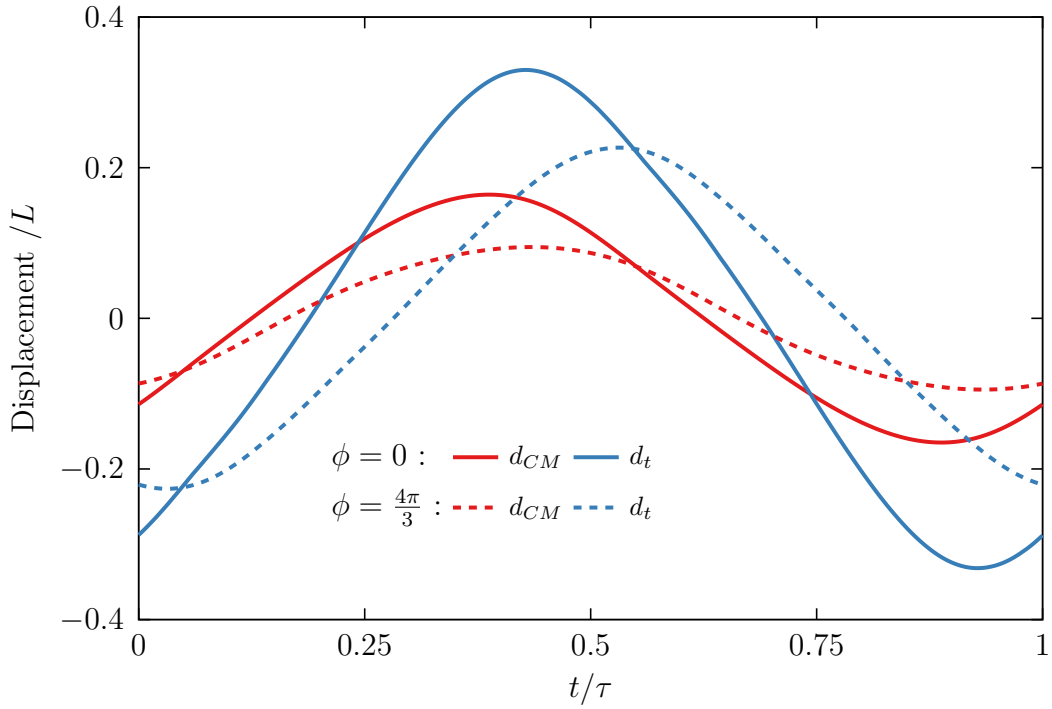

Figure 4.8: Time histories of the tip displacement d_t and the center of mass displacement d_{CM} at the maximum efficiency and the maximum thrust. The solid lines with symbols show the free swimming external (diamonds) and internal (triangles) actuation with different amplitudes of A_0 and M_0.

deflection (Figure 4.7a). At the maximum efficiency the bending pattern develops a dip near the middle of the plate reducing the displacement of the center of mass. At minimum power, the plate deflection is almost null along the entire length. In fact, in this configuration the actuation methods compensate each other almost perfectly. Consequently the plate deflects almost like a heaving rigid plate. This configuration minimizes the power consumption but in turn does not yield any significant propulsion.

The tip and CM displacements over an oscillation period are shown in figure 4.7c. For $\phi = 0$ the tip and CM move by nearly 50% more than for $\phi = 4\pi/3$. Furthermore, for $\phi = 4\pi/3$ the CM and tip are not in-phase which suggests higher bending mode contributions.

4.4 Flow Field

The difference in bending patterns results in different flow patterns generated by the oscillating plates with a significantly higher vorticity at $\phi = \pi/12$ than at $\phi \simeq 4\pi/3$ and even more so than at $\phi = 11\pi/12$. Indeed, when the actuation signals are in phase opposition not only the tip displacement is minimal, which results in poor thrust performance, but the CM as well. The minimal CM displacement is directly associated to lesser SEV generation. Conversely, when the actuation signals are in phase the high tip displacement yields significant thrust, however the important generation of SEV results in lower efficiency. When $\phi \simeq 4\pi/3$, there is substantial tip displacement accompanied with moderate SEVs, this in turn results in a highly efficient propulsion.

We use the mean enstropy $\mathcal{E}$ to quantify the vorticity generated by the plates [86]. We find that $\mathcal{E}$ is roughly proportional to d_{CM} (Figure 4.7e), indicating that the magnitude of CM displacement dictates to a large extent the amount of vorticity produced by the plate. The plates with solely internal and external actuation generate $\mathcal{E}$ similar to that of the combined actuation plate. Furthermore, when $\mathcal{E}$ is plotted against the power $\overline{\mathcal{P}}$ (Figure 4.7f), we find that the data for all actuation methods collapse into a single curve. Thus, the power is indeed proportional to amount of enstropy, which in turn is defined by the center of mass displacement.

4.5 Summary

In summary, we find that the hybrid internal-external actuation can be used to regulate the hydrodynamic performance of a propulsor by changing the phase difference between the actuation signals while maintaining high efficiency outperforming propulsors with a single actuation method. Our results suggest that the propulsion directly scales with the magnitude of the tip displacement, whereas the power is proportional to the displacement of the center of mass of the propulsor. The hybrid actuation

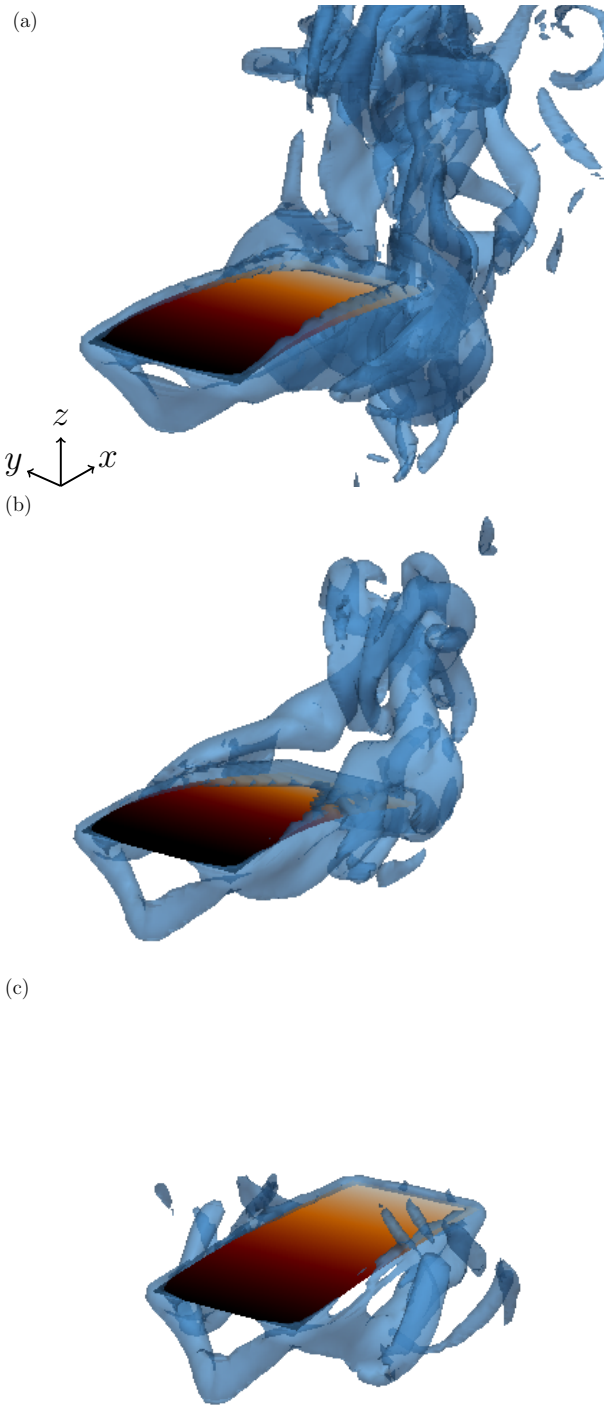

Figure 4.9: Contours of the normalized vorticity $\omega\tau = 10$ for (a) the maximum thrust, (b) the maximum efficiency and (c) the minimum power.

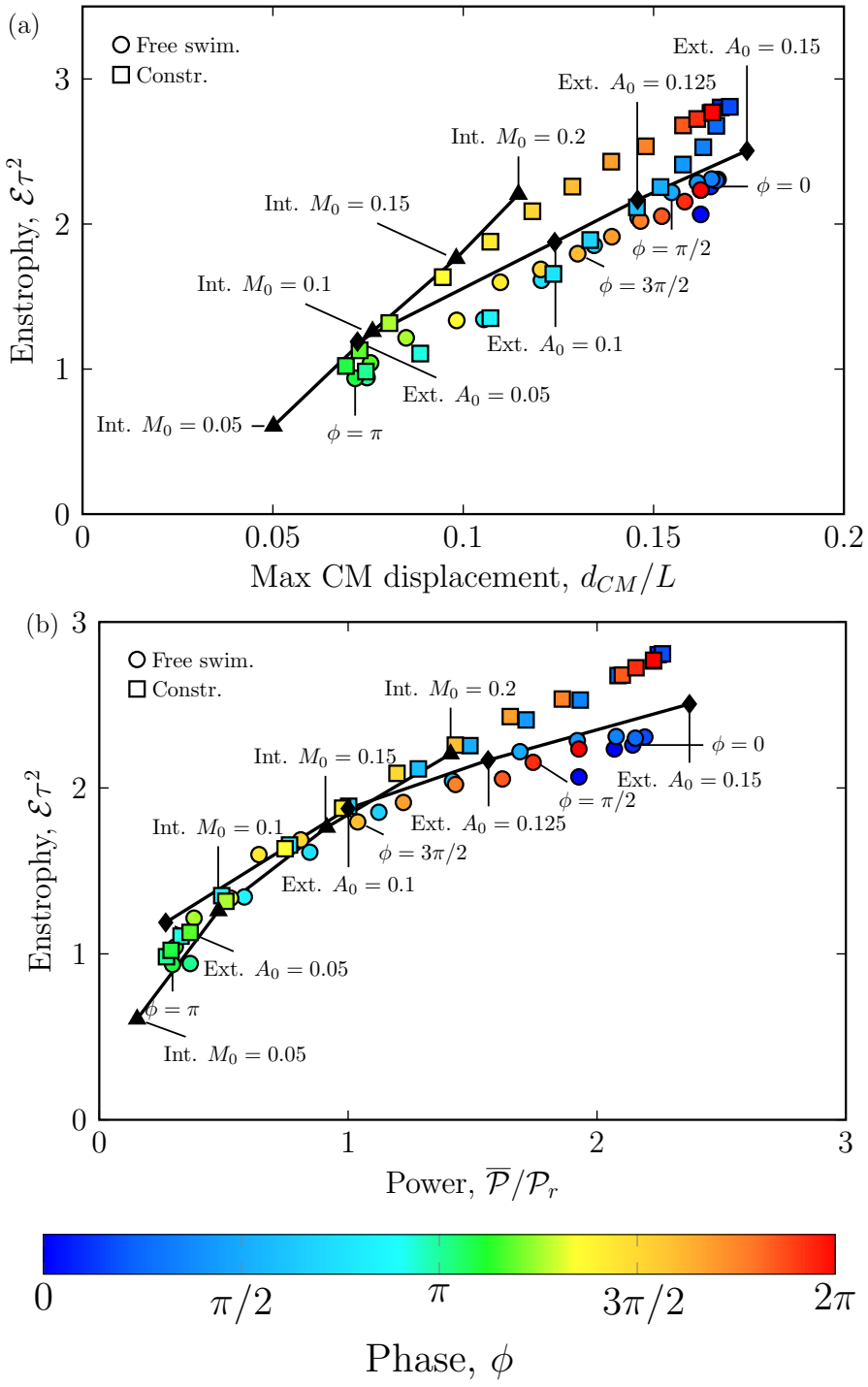

Figure 4.10: Dependence of the enstrophy $\mathcal{E}$ on the power $\overline{\mathcal{P}}$. The solid lines with symbols show for the constrained external (diamonds) and internal (triangles) actuation with different amplitudes of A_0 and M_0.

provides a unique way to regulate the balance between these two metrics, thereby yielding a propulsor with overall superior propulsion and efficiency performance.

CHAPTER 5
TAPERED ATTACHMENTS

5.1 Introduction

In previous chapters, we investigated the performance of externally and internally actuated plates as well as combined actuation methods for homogeneous elastic plates. Fish fins have undergone tremendous change in shape, function and mechanical properties through evolution. As a consequence, it is fundamental to understand the relationship between fin properties and hydrodynamic performance. In this chapter we consider internally and externally actuated plates augmented with a tapered passive attachment. The thickness, and therefore bending stiffness, is selected as a design parameter against which we measure the swimmer performance.

We study the swimmer performance at varying driving frequencies and thickness tapering and compare it against the performance of a uniformly thick plate. Our results show that the tapering is a critical design parameter for both the propulsion and swimming efficiency. Through wave theory arguments we characterize the effects of the thickness tapering and demonstrate that the nature of the wave propagation has a direct effect on the swimming performance. Furthermore, we demonstrate that the hydrodynamic performance scales directly with specific plate metrics. These metrics, inferred from our fully-coupled three dimensional model are then utilized in a simpler propulsor model which, coupled with an optimization procedure, allows us to explore an important part of the vast parameter space at a lower computational cost.

5.2 Fish Motion

From anguilliform fish whose motion is based on travelling waves to ostraciiform fish mainly using standing waves to propel, fish locomotion can be categorized by the type of wave propagation. In between, subcarangiform and carangiform fish use a combination of standing and travelling wave to achieve optimal swimming [88]. Gray [89] analyzed films of fish swimming in a tank and drew several qualitative conclusions from their study including a description of wave mechanisms creating forward thrust. Following this categorization of fish locomotion, Lighthill [34] showed that the nature of the propagating wave directly affects the swimming efficiency.

While fish use their muscles to dynamically change parameters such as the wave number, amplitude, velocity, or the ratio of standing to travelling wave [90], man-made devices are limited in generating and controlling complex bending patterns. Although travelling waves can improve the propulsion efficiency in fish locomotion, it is not trivial to generate travelling waves in a finite-sized swimmer. When a travelling wave is generated at one end of a plate, the reflection at the other end creates a backward-propagating wave. The summation of these two identical waves propagating in opposite directions creates a standing wave. However, it has been shown that there are several ways to generate a travelling wave in a finite-sized structure including active [91] and passive [40] solutions. Inspired by natural fish fin tapering, we use a novel passive approach to enhance propulsor hydrodynamics using tapered structures and the acoustic black hole effect.

5.3 Tapered Propulsor

We consider a homogeneous plate of constant thickness h_h and stiffness D_h with a tapered attachment of varying thickness h and stiffness D. The homogeneous part of the plate is either internally actuated with a distributed bending moment

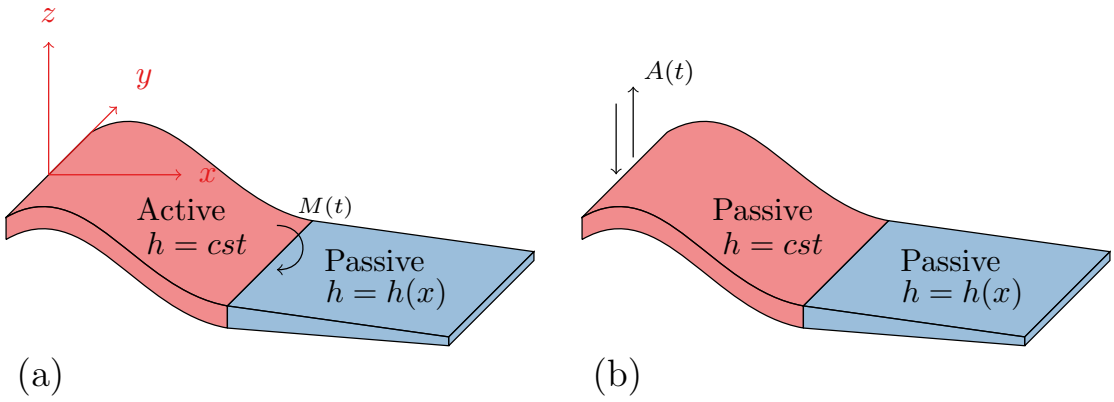

Figure 5.1: Schematics of the (a) internally and (b) externally actuated plate with a tapered attachment.

$M(t) = M_0 D \frac{L}{W} \sin \omega t$ or passive and driven by a heaving motion $A(t) = A_0 L \sin \omega t$ at the root. We illustrate these configurations in figure 5.1 where $M_0 = 0.1$ is the dimensionless moment and $A_0 = 0.1$ is the dimensionless heaving amplitude. The tapered attachment is completely passive in both instances, all sources of displacement come from either the motion of the internally actuated part or the external actuation. We additionally define L_h and L_t, respectively, the uniform and tapered section lengths so that $L_h + L_t = L$. The plate thickness can be expressed as a continuous piecewise-differentiable function ($h \in C^{\infty}_{pw}$).

$$h : x \longmapsto \begin{cases} h_h, & \text{for } x \in [0; L_h] \\ h_t(x), & \text{for } x \in]L_h; L] \end{cases}. \tag{5.1}$$

Here h_t is a general C^{∞} function setting the "shape" of the tapering. Five distinct cases are selected and referred to as : uniform, linear, parabolic convex, parabolic concave, and exponential. The corresponding functions are given by

$$\forall x \in]L_h; L] \ , \ h_t(x) = \begin{cases} h_h, & \text{uniform} \\ \frac{h_h}{r_h}\left[r_h + (1-r_h)\frac{x-L_h}{L_t}\right], & \text{linear} \\ \alpha\left(\frac{x-L_h}{L_t}\right)^2 + \beta\left(\frac{x-L_h}{L_t}\right) + \gamma, & \text{parabolic} \\ h_h \exp\left(-\frac{x-L_h}{L_t}\ln r_h\right) = h_h r_h^{-\frac{x-L_h}{L_t}}, & \text{exponential} \end{cases} . \quad (5.2)$$

Here, $r_h = h(0)/h(L)$ is the ratio of the root to the tip thickness referred to as the tapering ratio. In the case of the parabolic tapering, additional control parameters are defined as

$$\begin{cases} \alpha &= h_h\left(1 - \frac{1}{r_h}\right) + \theta \\ \beta &= 2h_h\left(\frac{1}{r_h} - 1\right) - \theta \\ \gamma &= h_h \end{cases} \quad (5.3)$$

where θ is the slope at the tip. In this case we define two distinct parabolic cases: the convex and concave parabolic shape as seen in figure 5.2. By examining the plots of the tapering shapes tested, we can sort each case from the less steep (closer to uniform) to the steepest in the following order : uniform, parabolic concave, linear, parabolic convex and finally exponential.

5.4 Acoustic Black Hole Theory

Mironov [92] showed that for tapered beams for which the thickness decreases following $h : x \longmapsto \varepsilon x^n, n \in \mathbb{N}^*$, the wave number goes to infinity, and consequently the phase and group velocity go to zero. When the wave number goes to infinity, any wave propagating needs an infinite time to reach the zero-thickness tip, resulting in a region where waves are trapped. This region is called an acoustic black hole (ABH) due to the analogy with celestial black holes. In practice, manufacturing a beam or

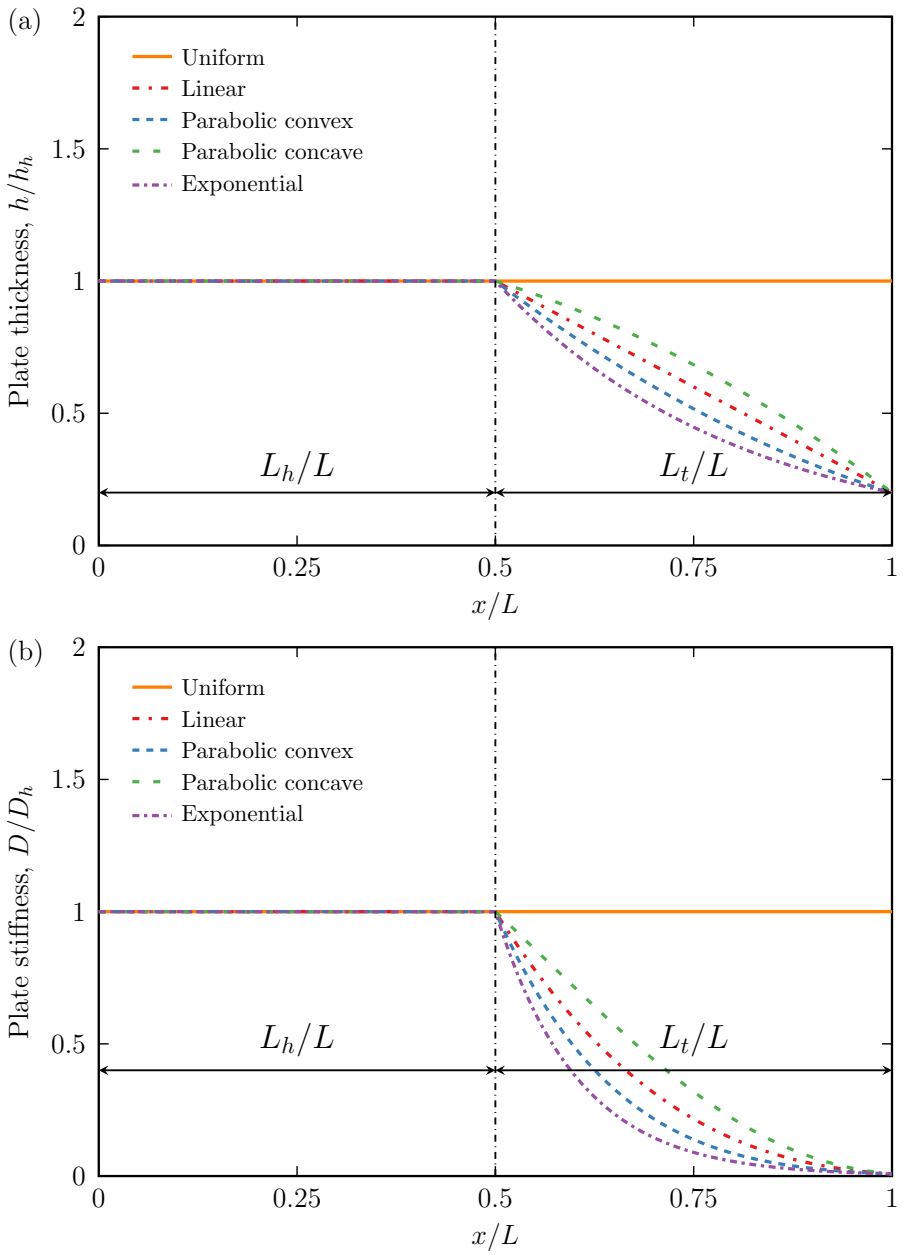

Figure 5.2: Plate (a) thickness and (b) stiffness distribution along the length for $r_h = 5$, $L_h/L = 0.5$ and several shapes normalized by the uniform section's properties.

plate with a zero-thickness tip is neither possible nor desirable due to physical limitations and structural integrity. When the plate thickness does not exactly reach zero, reflections occur at the end of the plate thus greatly weakening the acoustic black hole effect. Krylov [93] showed that applying absorbing thin layers to the beam surface compensated the loss of the ABH effect. In the literature, ABH devices have mainly been studied for their application to vibration control [94], [95], sound radiation control [96] and energy harvesting [97]. In this work we propose a new innovative way to take advantage of the ABH effect to enhance propulsion.

Consider a flexural wave propagating in a tapered plate of thickness h, the local wave number, phase, group velocities and total transit time from 0 to L are respectively given by

$$\begin{cases} k(x) & = \left(\frac{12\rho\omega^2}{Eh^2(x)}\right)^{\frac{1}{4}} \xrightarrow[h\to 0]{} \infty \\ c_p(x) & = \frac{\omega}{k} = \left(\frac{E\omega^2}{12\rho}\right)^{\frac{1}{4}} \sqrt{h(x)} \xrightarrow[h\to 0]{} 0 \\ c_g(x) & = \frac{\partial\omega}{\partial k} = 2\left(\frac{E\omega^2}{12\rho}\right)^{\frac{1}{4}} \sqrt{h(x)} = 2c_p(x) \xrightarrow[h\to 0]{} 0 \\ \mathcal{T}_{0\to L} & = \int_0^L \frac{dx}{c_g(x)} \xrightarrow[h\to 0]{} \infty \end{cases} . \tag{5.4}$$

From these expressions it is clear that a decreasing thickness leads to a decrease in the phase and group velocities and an increase in the wave number and total transit time. In the limiting case of a zero tapering at the tip, the wave number and total transit time become infinite and both velocities become zero. An infinite transit time means that waves are trapped at the end of the plate. In the realistic case where the tapering does not go to zero, we show in figure 5.3a the total transit time needed for a wave originating at the root to reach the tip. Evidently with a non-zero thickness the total transit time is finite; however, it increases with both the stiffness ratio and steepness of the tapering shape. For instance, with a tapering ratio $r_h = 5$ the total transit time increases by approximately $20 - 25\%$ for attachments of any tapering shape. Most of

the ABH theory presumes regularity conditions on the thickness, namely the Wentzel-Kramers-Brillouin-Liouville-Green (WKBLG) condition [98]–[102] assumes that the local wave number varies slowly over a distance of the order of the wavelength

$$\frac{1}{k^2}\frac{dk}{dx} \ll 1 \ . \tag{5.5}$$

In figure 5.3b, we plot the smoothness criterion for the linear and exponential tapering shapes covering a wide range of stiffness ratios. As expected, the interface between the plate and the tapered attachment displays a sharp jump in smoothness since the thickness is not differentiable at this point. In other words, the further the attachment deviates from uniform the less smooth the transition is. A poor smoothness could mean reflections at the interface between the plate and the attachment which could defeat the purpose of using the attachment. The main goal of this study is to investigate how impeding wave reflections at the free end using the ABH effect can affect the locomotion and improve the overall propulsion efficiency. In sections 5.5 to 5.9 we consider an internally actuated plate with tapered attachments. Conversely, in section 5.10 we examine the effects of the actuation method by considering both internally and externally actuated plates with tapered attachments. In this chapter, the mass ratio $\chi = 5$, overall length $L = 50$ LBU, aspect ratio $\mathcal{A}_R = 2.5$ and Reynolds number $Re = 2000$ are fixed.

5.5 Dynamic Response

Figure 5.4 shows the Bode diagram of the immersed internally actuated plate with a passive attachment of different tapering shapes and fixed tapering ratio $r_h = 5$. The solid markers represent the response of the uniform thickness part (internally actuated) of the plate while the empty makers represent the tapered (passive) part. Per definition, $r = 1$ corresponds to the resonance as shows the phase difference

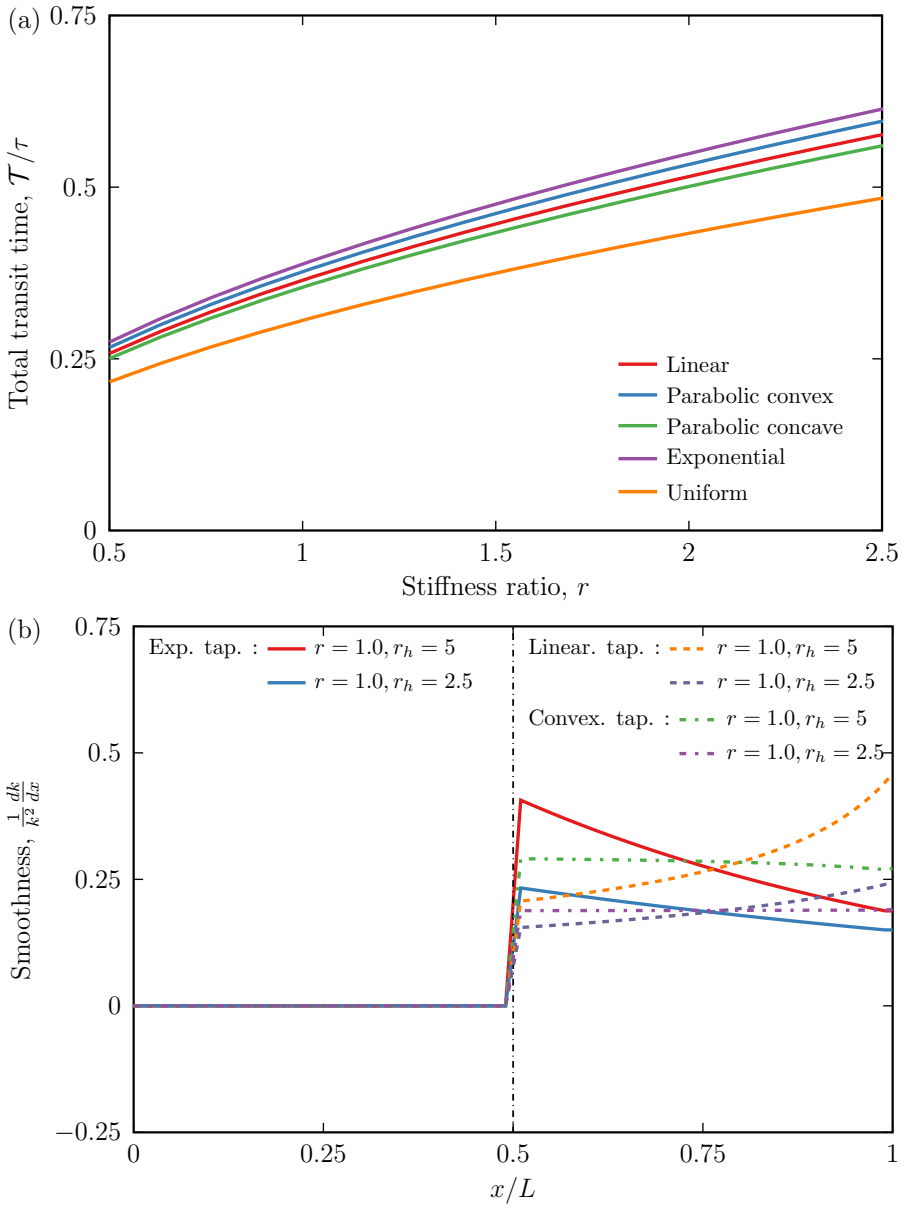

Figure 5.3: (a) Total transit time and (c) smoothness criterion for several tapering shapes, $r_h = 5$, $L_h/L = 0.5$ and several stiffness ratios.

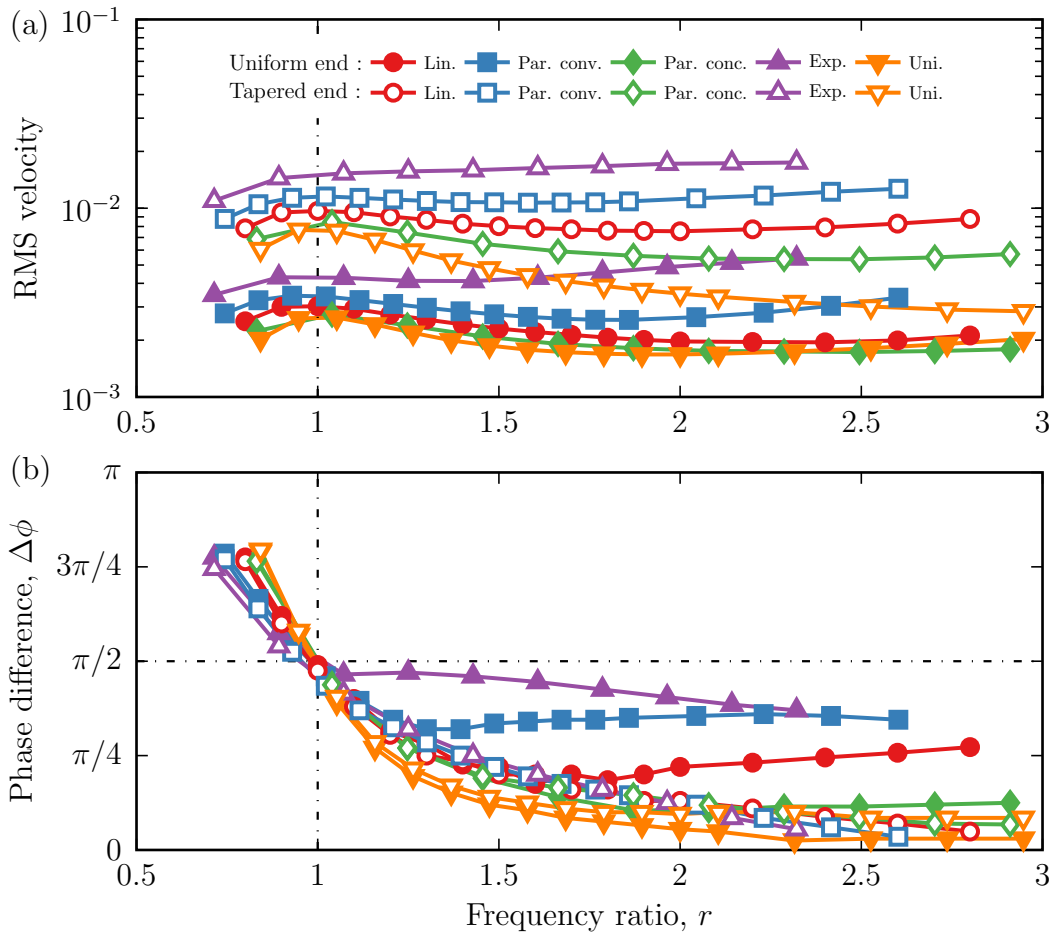

Figure 5.4: Bode diagram of the internally actuated plate with several tapered passive attachments for $r_h = 5$ and $L_h/L = 0.5$. Solid and empty markers respectively show the tapered and uniform end RMS velocity and phase difference.

$\Delta\phi = \pi/2$ on the phase plot. The phase difference $\Delta\phi$, defined as the phase difference between the input signal and the tip root mean square (RMS) velocity, is expected to asymptotically reach π or 0 away from resonance.

If we first examine the tip velocity (empty markers), we find that most attachments behave similarly near resonance ($r = 1$) with a characteristic local maximum. Furthermore, the parabolic concave attachment yields similar levels of tip velocity before and at resonance. Beyond that case, our results show that the "steeper" the tapering shape is, the higher the tip velocity at resonance. For instance, at resonance the exponential tapering yields almost twice as much tip velocity as the uniform plate.

More generally, our results indicate that the tip velocity gradually increases with the "steepness" of the tapered attachment. Off-resonance, any sort of tapering results in significant deviation from the uniform reference case. Indeed, past the resonance a uniform plate has its tip velocity and displacement significantly decrease, while in the case of a tapered attachment the decrease is attenuated. Again, the steeper the tapering the more attenuation until the limiting case of the exponential attachment, where the tip velocity monotonically increases even past the resonance. Moreover, our results clearly show a trend where the increase in tip velocity occurs at much lower frequency ratio r than that of the uniform plate. The uniform plate tip velocity decreases past $r > 3$ while even the parabolic concave and linear tapered attachments display a slight increase for $r \simeq 2.5$. The velocity at the interface between the uniform and tapered section (solid markers) mirrors the tip behavior with a slight difference, the linear and parabolic concave attachment curves are almost overlapping with the reference case.

For a uniform plate, $\Delta\phi$ is expected to abruptly change between 0 and π around the resonance, with the slope being a function of the overall damping. Interestingly, if we consider the tapered plate tip (empty markers), all phase lag curves overlap with minor discrepancies. Conversely, the phase difference at the interface between the uniform and tapered sections (solid markers) starts deviating and plateauing as the stiffness ratio increases for all tapering shapes; the steeper the tapering, the earlier the deviation from the uniform behavior. Overall, it appears that the dynamic response of the plate strongly depends on the tapering shape. Moreover, it evolves gradually with the thickness shape. It follows the "steepness" order from section 5.3: the parabolic concave attachment emulates the uniform attachment the closest, followed by the linear, parabolic convex, and finally exponential shape. Following the scaling laws derived in chapters 3 and 4, we can expect a significant improvement of the thrust performance, especially for the off-resonance frequencies.

5.6 Hydrodynamic Forces

In figure 5.5a we plot the thrust as a function of the stiffness ratio for an internally actuated plate with several tapered attachments and $r_h = 5$. As a reference case, we first examine the uniform passive attachment. We find that the thrust mirrors the tip velocity, it is maximized at resonance ($\overline{F}_x/F_c \simeq 0.025$) and rapidly decreases off-resonance. By examining all tapered attachments at resonance ($r = 1$), our results demonstrate that the steeper the thickness the more thrust generated with an overall maximum yielded by the exponential attachment ($\overline{F}_x/F_c \simeq 0.11$). Both parabolic concave and linear tapering mirror the uniform plate behavior with respect to the stiffness ratio; a local maximum at the resonance and a rapid decrease off-resonance. However, for all tapered attachments there is an increase off-resonance which is not observed for the uniform attachment. The thrust produced by the exponential and parabolic convex tapering significantly differs from all the other attachments. In the case of the exponential attachment, the local maximum thrust does not occur near the first resonance frequency, rather the thrust steadily increases with the stiffness ratio until it reaches a maximum ($\overline{F}_x/F_c \simeq 0.2$) off resonance for $r \simeq 1.8$. Similarly for the parabolic convex attachment, the maximum thrust ($\overline{F}_x/F_c \simeq 0.1$) is found for $r = 2.4$.

To understand the disparity in thrust generation we examine the maximum displacement d_t and d_h over a period at the tip of the tapered and uniform sections of the plate in figure 5.5b. A larger tip displacement translates into more fluid displaced backwards and therefore a higher thrust production. For both the tapered and uniform parts, the maximum displacement mirrors the thrust behavior, d_t and d_h are locally maximized near $r = 1$ with the exception of the exponential tapered attachment for which d_t increases steadily even past resonance. Note that the displacement of the linear and parabolic attachments similarly deviates from the uniform plate at

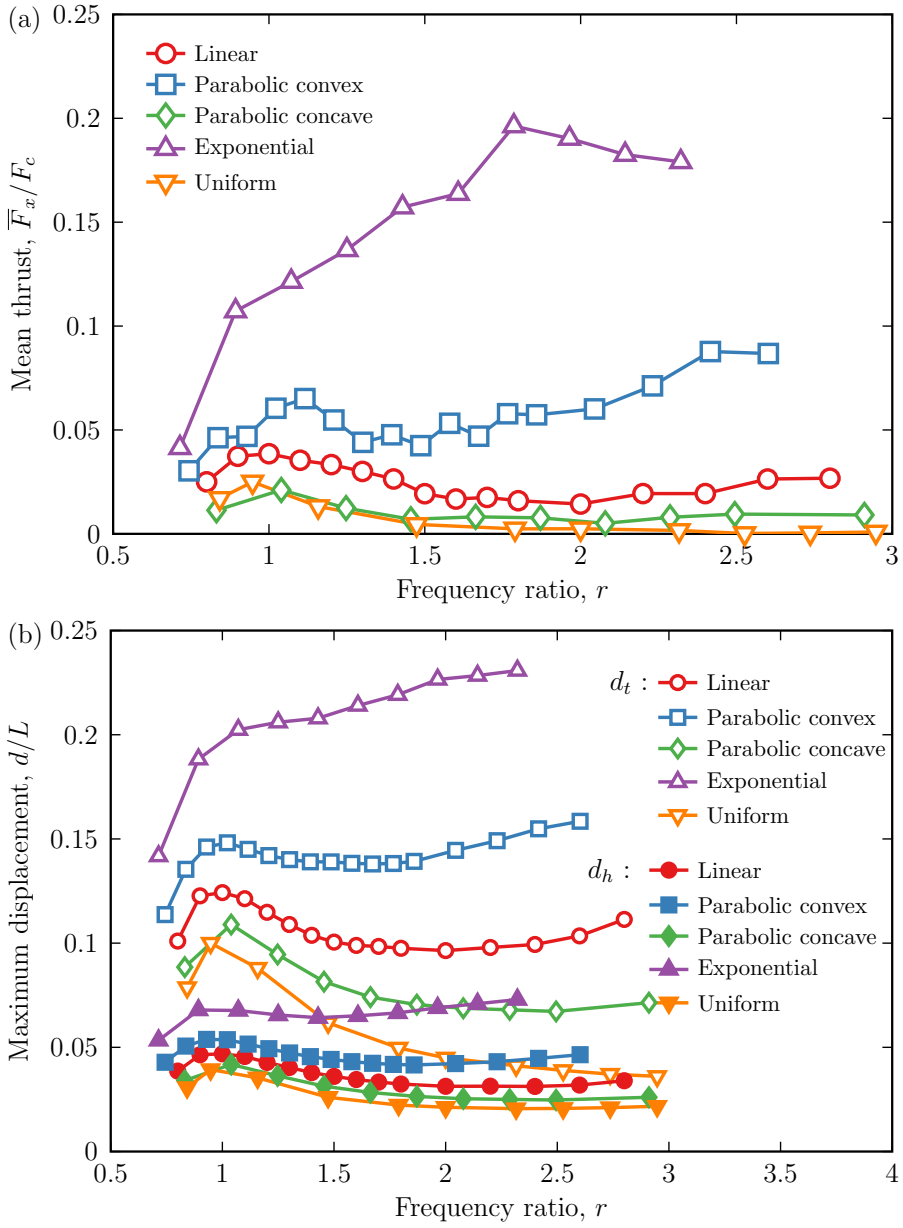

Figure 5.5: (a) Thrust and (b) maximum displacement at the tip of the tapered and uniform part of the internally actuated plate for several tapering shapes, $r_h = 5$ and $L_h/L = 0.5$. Empty and solid markers in (b) respectively show the tapered and uniform end tip displacement.

high r with a pronounced increase.

This behavior in tip displacement and ultimately thrust can be explained by re-examining uniform plates. For a uniform plate the gap between the first and second mode is about 6 times the first natural frequency. By definition, when driven at resonance, any actuation source is amplified by the plate which results in a maximum displacement and therefore thrust output as seen for the uniform attachment. Conversely, off-resonance the output is significantly smaller which explains the sudden drop in tip displacement shown in figure 5.5b. At first mode resonance, the tip displacement is locally maximal and it decays away from resonance with the rate depending on the mass ratio and fluid damping. Similarly, at the second mode resonance, the tip displacement displays another local maximum, and so on for higher modes. However, if the distance between resonance modes frequencies could be reduced, the tip displacement would not decay as significantly as it does for a uniform plate. Therein lays the advantage of tapered attachments : the mass and stiffness gradient results in a shift of higher mode resonance to lower frequencies which in turn yields in an overlap of the resonance bands [103]. This overlap translates into a reduced decrease of the tip displacement, ultimately leading to a steady increase with frequency for the exponential tapering. Consequently, our results show that adding tapering increases the displacement and therefore thrust of the plate, especially off-resonance.

5.7 Bending Patterns

By definition, at resonance, the first harmonic is selected and amplified by the plate; therefore, a travelling wave generated at the root should reflect at the tip to create a standing wave. However, a uniform plate driven off-resonance yields a mix of travelling and standing waves due to the richer nature of the spectrum. Furthermore, the non-uniform damping along the length of the plate due to viscous forces results

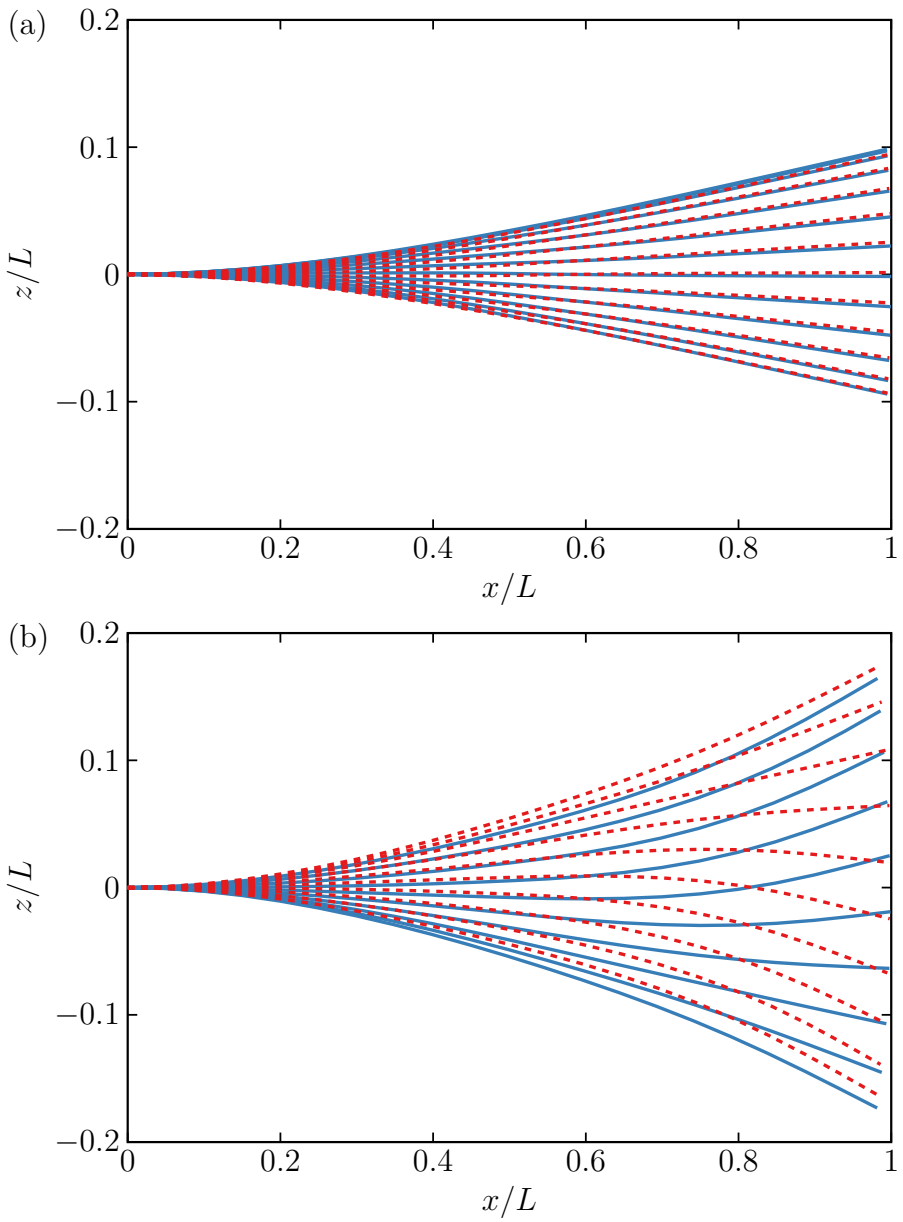

Figure 5.6: Instantaneous bending patterns of the internally actuated plate for the (a) uniform and (b) exponential passive attachment at resonance ($r = 1$) for $r_h = 5$ and $L_h/L = 0.5$.

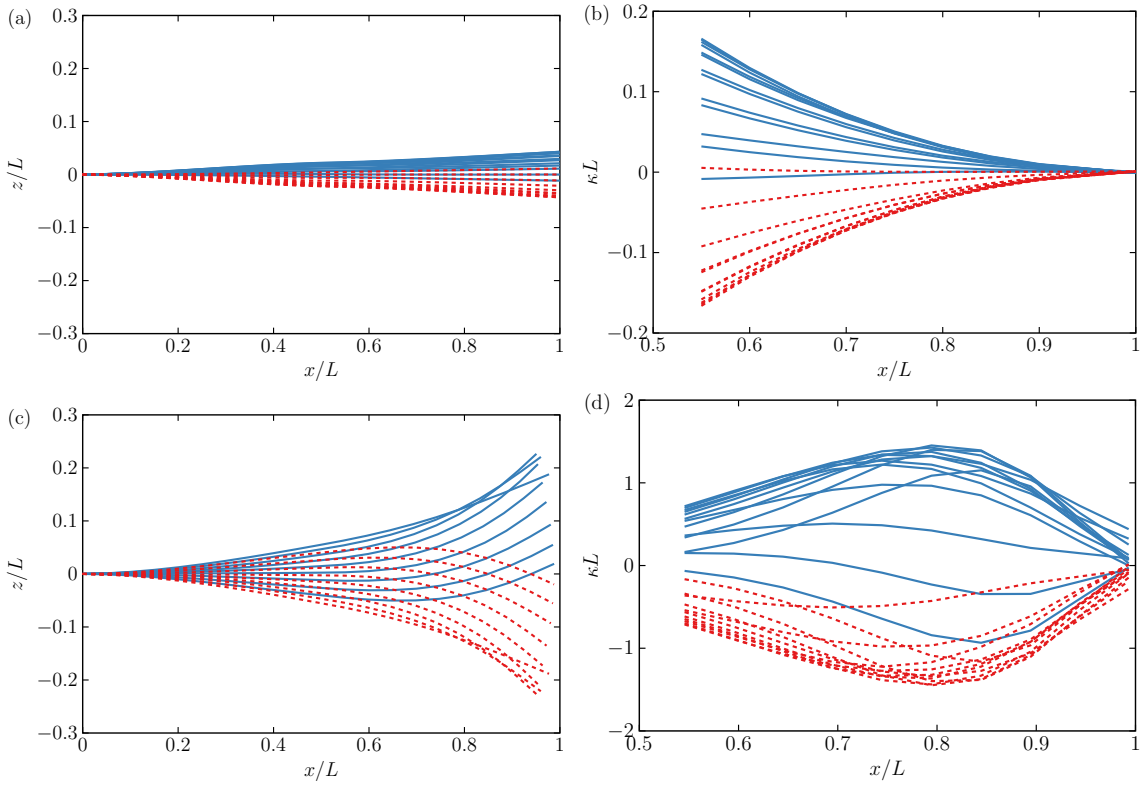

Figure 5.7: Bending and curvature patterns of the internally actuated plate for the (a-b) uniform and (c-d) exponential tapered attachments off-resonance ($r = 2$) for $r_h = 5$ and $L_h/L = 0.5$.

in a variation of the waves generating at the root as they travel down towards the tip and back to the root [40]. Due to the presence of other harmonics in the signal and varying damping, the superposition of the input wave and its reflection does not yield a pure standing wave. In figure 5.6a we show the instantaneous bending patterns for the internally actuated plate with a uniform passive attachment at resonance. As expected, at resonance the reflection at the tip creates a standing wave characterized by oscillations in phase at every point of the plate. Conversely, in figure 5.6b the internally actuated plate with an exponential passive attachment yields a noticeably different bending pattern. Although the plate is actuated at resonance, the dynamic response combines travelling and standing waves. Due to the ABH effect, the tapered attachment impedes waves from reflecting at the tip and thus results in a mix of standing and travelling waves.

We further address the tip displacement behavior off-resonance by examining instantaneous bending patternsn as shown in figure 5.7a and 5.7c, and curvature $\kappa(x) = z''(x)/\left[1 + z'^2(x)\right]^{3/2}$ profiles in the tapered passive attachment, in figure 5.7b and 5.7d, for both the uniform and exponential attachments off-resonance ($r = 2.0$). Both bending patterns in figures 5.7a and c are characteristic of off-resonance oscillations, a mix of travelling and standing waves resulting in non-overlapping curves. In agreement with results shown in figure 5.5b, the exponential attachment yields about four times more tip displacement than the uniform attachment as seen by comparing the displacement envelopes. Moreover, beyond the difference in maximum displacement, the choice of the attachment significantly impacts the form of the envelope as formally measured by the curvature in figures 5.7b and 5.7d.

By directly comparing the attachments, our results show that not only the amplitude of the curvature in the exponential attachment is about four to five times higher than in the uniform counterpart but the distribution of the curvature along the attachment differs significantly. For the uniform attachment, the maximum curvature is obtained at the interface between the plate and the attachment ($x/L = 0.5$) with a maximum $\kappa_{max}L \simeq 0.18$ while the exponential attachment displays a maximum $\kappa_{max}L \simeq 1.5$ around $x/L \simeq 0.8$. Due to the low bending stiffness at the tip, the same internal moment input leads to a larger curvature and therefore deformation in the tapered attachment compared to the uniform attachment. Moreover, the steeper the change in thickness the higher the curvature and deformation along the length of the attachment, which explains the increased thrust production shown in figure 5.5a. Note that for passive attachments the curvature at the tip is zero. The curvature at the tip of the exponential attachment slightly deviates from zero due to the approximation of the derivatives at the tip.

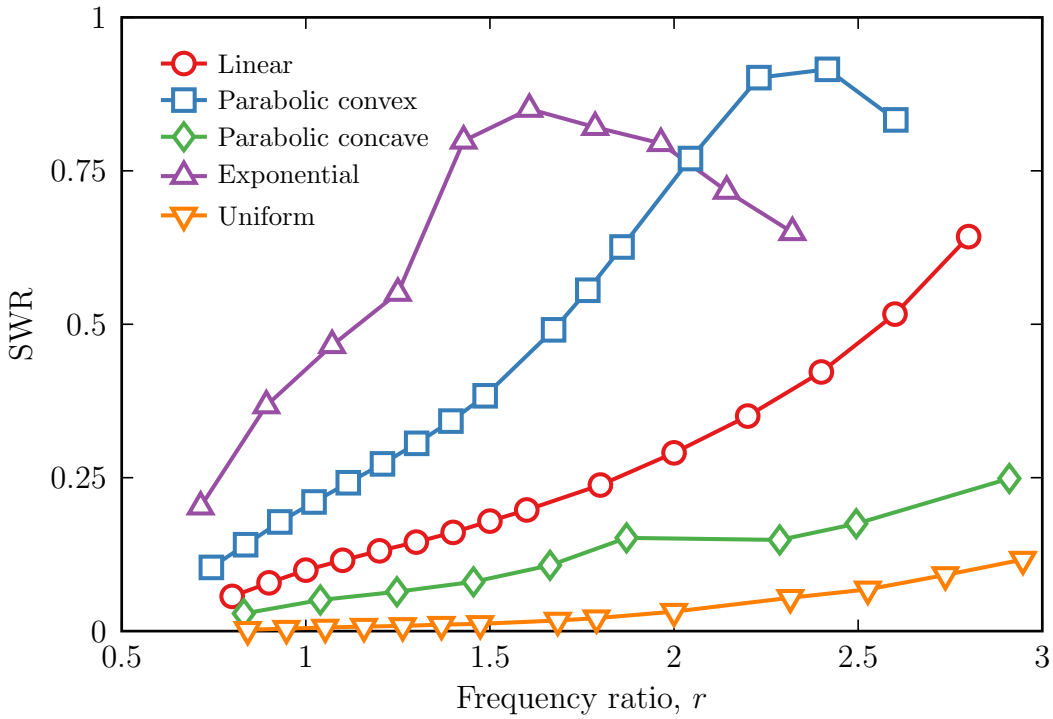

Figure 5.8: Standing wave ratio of the internally actuated plate with several tapered passive attachments for $r_h = 5$ and $L_h/L = 0.5$.

5.8 Standing Wave Ratio

In order to formally quantify the amount of travelling to standing waves resulting from the addition of a tapered attachment, we define a travelling to standing wave ratio (SWR). There are several ways to formally identify the SWR, practically its computation is based on fitting a Hilbert transform onto an ellipse in the complex plane [104]. We show in figure 5.8 the dependence of the SWR with the frequency ratio. We find that steeper tapering leads to a higher SWR. Furthermore, as the frequency ratio increases the SWR also increases with the rate depending on the tapering shape. For the exponential and parabolic convex shapes it reaches maxima for $r = 1.6$ and $r = 2.4$. Past these frequencies, the SWR decreases with a similar rate for both tapering shapes. We speculate that a similar phenomenon occurs for the less "steep" tapering shapes at higher frequencies. Although it is less "steep", the parabolic convex yields a slightly higher SWR (0.92) than the exponential taper-

ing (0.85). Similarly, the SWR due to linear tapering increases steadily and nearly surpasses the exponential SWR for $r > 2.5$, the maximum r considered in the simulations. These observations indicate that the higher tapering the sharper the increase in SWR, however the maximum value is not directly defined by the tapering sharpness. This can be explained by the lower smoothness of the exponential tapering with respect to the parabolic convex tapering. Nevertheless, the significant increase in SWR shows that tapered plates of non-vanishing thickness are an effective solution to maintain travelling waves in structures of finite size. Additionally, the shape of the tapering is an effective way to tune the SWR of the plate.

5.9 Hydrodynamic Efficiency

We first investigate the effects of the different tapered attachments on the power input $\mathcal{P}$. In figure 5.9a we plot the normalized power input as a function of r for different tapering shapes and $r_h = 5$. Once again every case displays a pattern similar to the uniform attachment, local maximum at the resonance with a decrease off resonance. While the uniform attachment yields $\overline{\mathcal{P}}/P_c \simeq 0.1$ for $r = 1$, every tapered attachment results in a higher power input at resonance. For instance, the exponential attachment yields more than four times the power input of the uniform attachment. Indeed, as seen by examining the bending patterns (figures 5.6 and 5.7) tapered attachments result in not only a higher tip displacement but generally a larger deformation envelope. A larger envelope in turn leads to an increased viscous dissipation resulting in additional power consumption.

In figures 5.5, 5.8 and 5.9a we quantified the effect of tapered attachments on the thrust and the power input. Therefore we now quantify the hydrodynamic efficiency of the plate. In figure 5.9b we plot the efficiency as a function of r for several attachments and $r_h = 5$. In the case of the uniform passive attachment the efficiency decreases until it reaches a local minimum for $r \simeq 1.7$. The efficiency then increases sharply

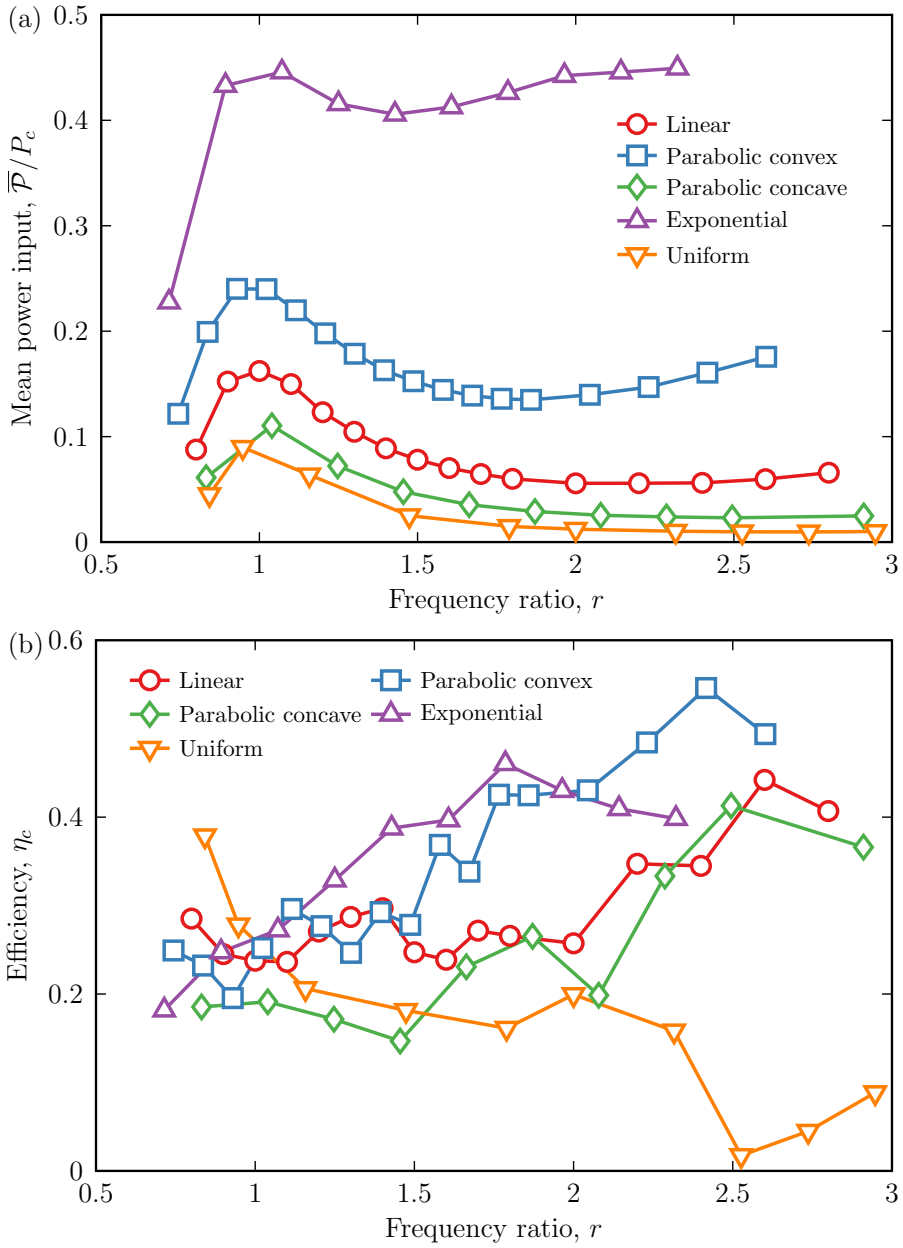

Figure 5.9: (a) Power consumption and thrust efficiency for internally actuated plates with several tapered passive attachments for $r_h = 5$ and $L_h/L = 0.5$.

with a local maximum at $r \simeq 2$ followed by a steep decrease. Overall in the case of the uniform passive attachment the actuation frequency needs to be accurately tuned to optimize the efficiency. For every tapered attachment tested, the efficiency is close to the minimum at the first resonance with the magnitude similar to that of the uniform plate. However, tapered attachments outperform the uniform attachment for the past resonance frequencies. For instance, the parabolic convex attachment yields $\eta \simeq 0.55$ for $r = 2.4$ or approximately 1.4 times the efficiency of the uniform attachment at its best. Interestingly the parabolic convex, while it is not the "steepest" tapering, outperforms the exponential attachment not only in the range of high-efficiency but also in peak efficiency.

This disparity in "steepness" and performance can be explained by re-examining the smoothness criterion of each attachment (figure 5.3c). Indeed among all shapes, the parabolic concave and convex attachments have the smoothest transition at the interface. A sharp jump at the interface might lead to spurious modes and reflections affecting the overall efficiency. Additionally, across most tapering shapes the efficiency is maximized when SWR $\sim 0.5 - 0.8$ which is comparable to results from Cui et al. [88].

5.10 Scaling Metrics

To this point, we observed and evaluated the swimming performance and various hydrodynamic metrics versus the frequency ratio r. Similarly to chapter 4, we investigate the effects of the passive tapered attachment on the relationships established between plate kinematics and the thrust, power, and efficiency. Furthermore, we investigate the impact of the tapering ratio r_h and actuation method on the performance of the plate.

In figure 5.10a we plot the relationship between the thrust and the tip displacement for various tapering shapes and two tapering ratios. Our results show a clear trend

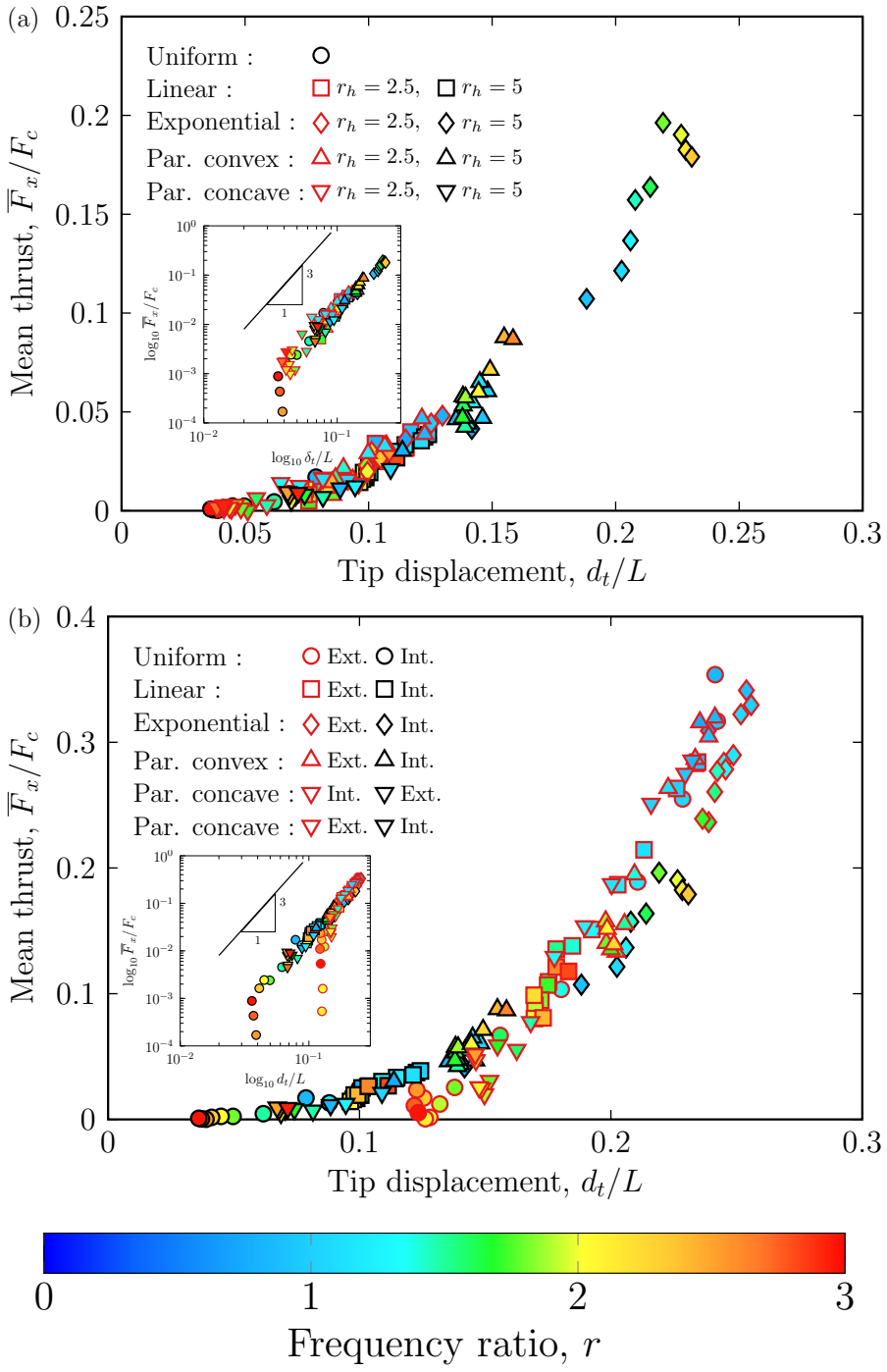

Figure 5.10: (a) Relationship between the thrust output, frequency ratio and tip displacement for internally actuated plates with a passive tapered attachment for $r_h \in \{2.5, 5\}$ and $L_h/L = 0.5$. (b) Relationship between the thrust output, frequency ratio and tip displacement for externally and internally actuated plates with several tapered passive attachments for $r_h \in \{2.5, 5\}$ and $L_h/L = 0.5$.

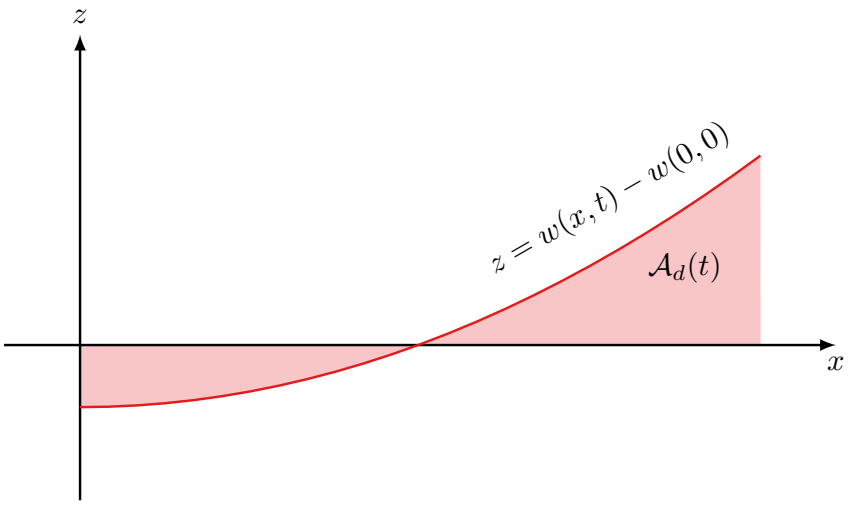

Figure 5.11: Illustration of the instantaneous displacement area $\mathcal{A}_d$.

between $\overline{F}_x$ and d_t. Similarly to chapter 3, the thrust scales directly with the tip displacement $\overline{F}_x \sim d_t^3$, independently of the tapering of the passive attachment or the tapering ratio r_h. The steeper the tapering, the higher the tip displacement and therefore the higher the thrust output.

In figure 5.10b we consider the effects of the actuation method by plotting $\overline{F}_x$ as a function of d_t for internally and externally actuated plates with a tapered passive attachment. Once more, the thrust scales directly with this metric, as can be seen in the log log inset $\overline{F}_x \sim d_t^3$, independently of the actuation method. Furthermore, the externally actuated plate with a passive tapered attachment produces significantly more thrust than the plate actuated internally with the same attachment. This observation confirms the results observed for the completely uniform plate in chapter 3 in which we concluded that externally actuated plates generated significantly more thrust than internally actuated plates due to a difference in bending patterns. Overall, we can establish a first metric, maximizing the tip displacement, that is needed for optimizing the performance of a tapered propulsor.

Nevertheless, maximizing the tip displacement alone leads to poor performance

due to a saturation at high tip displacements (fluid is not pushed in the propulsion direction) as well as poor energetic performance. As a consequence, a second metric is needed that can be related to the power consumption. In chapter 4, our results showed that the power scaled directly with the center of mass displacement. This criterion was inferred from examining the vortex structure generated by the oscillating plate. A lower enstrophy (measure of vorticity) accompanies a lower power consumption, that is due to lower losses through viscous dissipation. In chapter 4 we directly related the enstrophy, and therefore viscous dissipation, to the lesser relative motion between the fluid and the plate. Here, the mass gradient in the tapered tail shifts the center of mass depending on the tapering shape and tapering ratio. Therefore, instead of using the center of mass displacement, we examine the period-maximum area displaced by the plate $\mathcal{A}_{d,m}$ computed as

$$\mathcal{A}_d(t) = \frac{1}{L^2} \int_0^L [w(x,t) - w(0,0)]\, dx \tag{5.6}$$

$$\mathcal{A}_{d,m} = \max_t \mathcal{A}_d(t) \tag{5.7}$$

where z is the displacement of the plate along the centerline as illustrated in figure 5.11. For instance, consider the limiting case of a rigid plate. It produces limited thrust, however the power input is minimal as is $\mathcal{A}_{d,m}$. The lower $\mathcal{A}_{d,m}$, the lower the relative motion between the fluid and the plate which is conjectured to result in a lower power consumption.

In figure 5.12a we plot the mean power as a function of the maximum displacement area. The results indicate that the "steeper" the tapering shape the greater the power is. Similarly, the higher the taper ratio r_h, the more power. As hypothesized, there is a direct relationship between the power and the displacement area $\overline{\mathcal{P}} \sim \mathcal{A}_{d,m}^3$, as shown by the log log inset. The lower the displacement area, the lower is the power

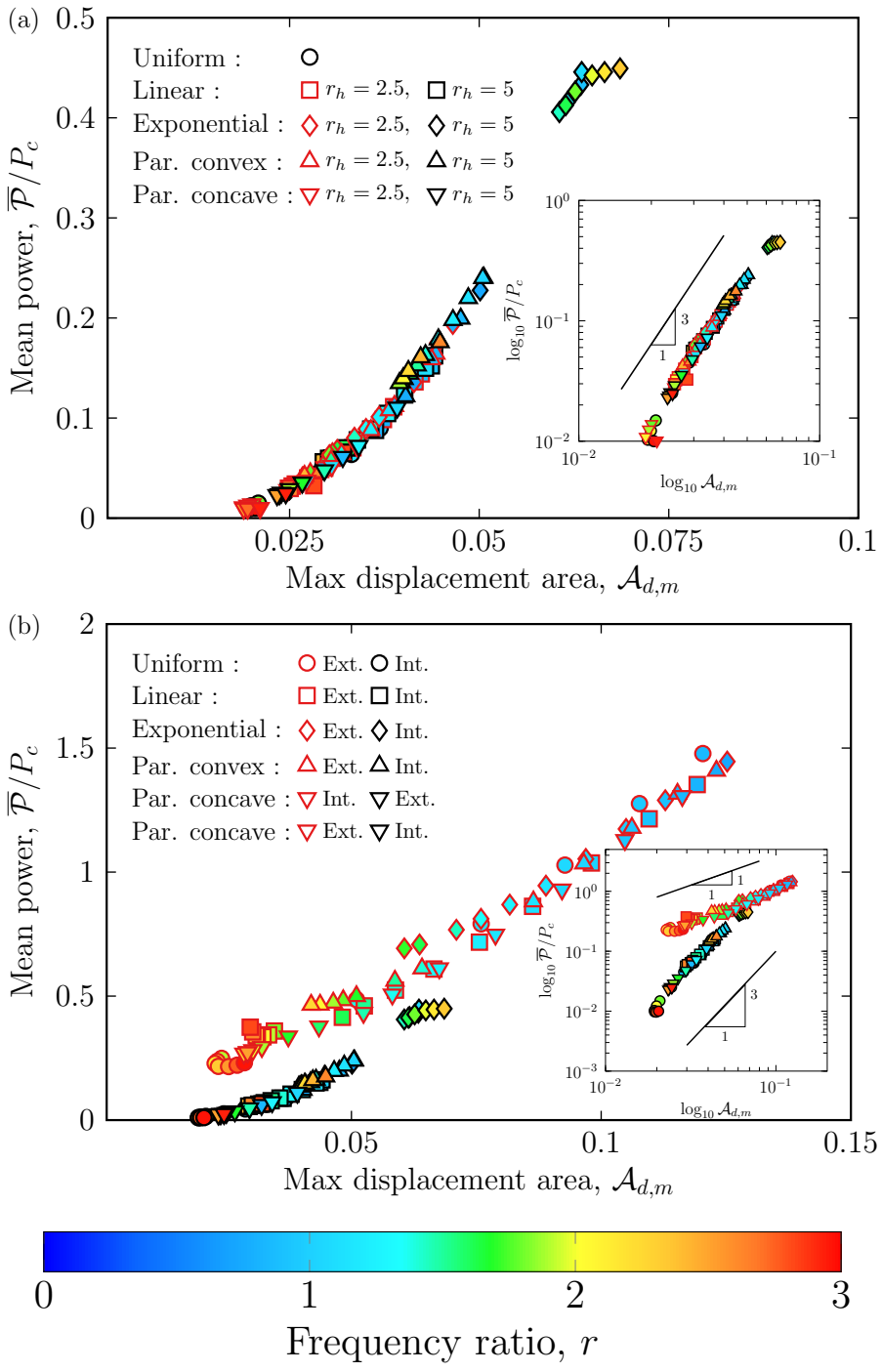

Figure 5.12: (a) Relationship between the power, frequency ratio and maximum displacement area for internally actuated plates with a passive tapered attachment for $r_h \in \{2.5, 5\}$ and $L_h/L = 0.5$. (b) Relationship between the power, frequency ratio and maximum displacement area for externally and internally actuated plates with several tapered passive attachments for $r_h \in \{2.5, 5\}$ and $L_h/L = 0.5$.

and vice versa. Therefore, minimizing the maximum displacement area is equivalent to minimizing the power input. In figure 5.12b we investigate the impact of the actuation method by plotting the power as a function of the maximum displacement area for internally and externally actuated plates augmented with passive tapered attachments. Our results demonstrate that the power scales directly with the maximum displacement area independently of the actuation method. However, similarly to the phenomena observed in chapter 3, the power of internally actuated plates differs from the external counterpart. Indeed, while for internally actuated plates $\overline{\mathcal{P}} \sim \mathcal{A}_{d,m}^3$, we find that $\overline{\mathcal{P}} \sim \mathcal{A}_{d,m}$ for externally actuated plates. However, in the range tested, the same $\mathcal{A}_{d,m}$ results in lower power consumption for internally actuated plates when compared to externally actuated plates. Conversely in chapter 3, we found that fully internally actuated plates without tapered attachments required slightly more power for similar plate kinematics. This observation demonstrates that passive tapered attachments can significantly enhance the energetic performance of internally actuated plates.

Maximizing the efficiency is then a trade-off between maximizing the tip displacement and minimizing the displacement area. In figure 5.13 we plot η as a function of $\mathcal{A}_{d,m}/d_t$. We find that the efficiency is strongly correlated to $\mathcal{A}_{d,m}/d_t$. The lower this ratio, the higher the efficiency. A lower $\mathcal{A}_{d,m}$ results in lower power while a high d_t translates into high propulsion. The first resonance frequency is an excellent candidate to maximize the tip displacement as the resonance is defined by the maximum tip displacement. However, if we reason in terms of $\mathcal{A}_{d,m}$, then the first mode bending is not optimal. Indeed, the first mode bending patterns are characterized by monotonically increasing (or decreasing) displacement along the length of the plate. This in turn, results in a maximum $\mathcal{A}_{d,m}$ since every position of the plate contributes to the integration with the same sign. Therefore, although first mode is interesting when considering thrust, it has a poor energetic performance as demonstrated in

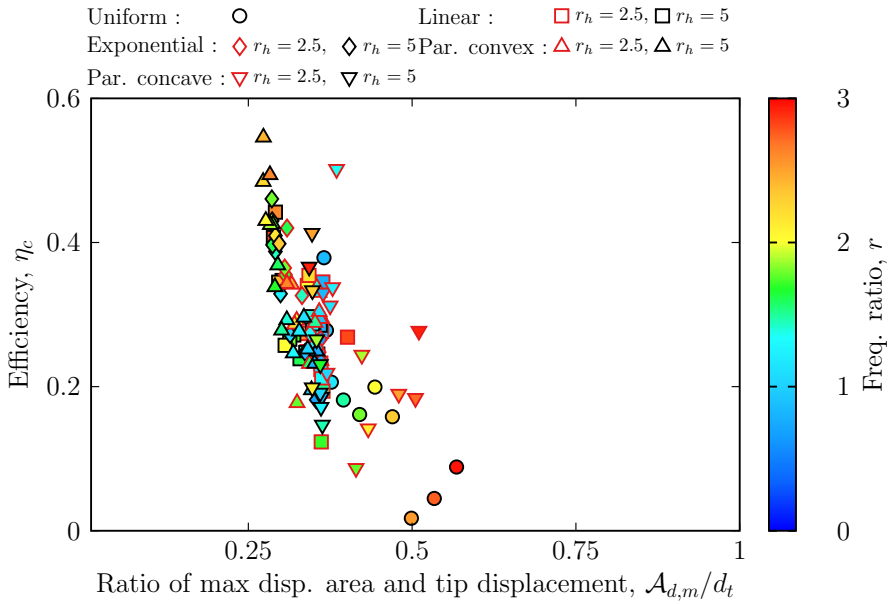

Figure 5.13: Efficiency as a function of the ratio of displacement area to tip displacement $\mathcal{A}_{d,m}/d_t$ for internally actuated plates with a passive tapered attachments for $r_h \in \{2.5, 5\}$ and $L_h/L = 0.5$.

figures 5.12, 5.9a and 5.9b. Conversely, at higher frequencies, the incorporation of higher modes in the bending patterns may decrease the displacement area with sections of the plate compensating for the displacement of others therefore resulting in lower relative motion between the fluid and solid. However, off-resonance actuation results in lower tip displacement which is why the uniform plate is not performing particularly well. Nevertheless, in the case of a tapered attachment, the displacement off-resonance is amplified due to the overlap between first mode and higher mode resonance frequencies thereby creating a region of high tip displacement and low $\mathcal{A}_{d,m}$ which results in high efficiency as seen in figure 5.9b. Therein lays the advantage of tapered attachments, the stiffness and mass gradient allows maximizing the tip displacement while maintaining relatively low $\mathcal{A}_{d,m}$ levels off-resonance.

This conclusion is visually striking when examining the flow field and more particularly the vorticity generated by the plates with tapered attachments. In figures 5.14 we show the vorticity fields generated by internally actuated plates with three

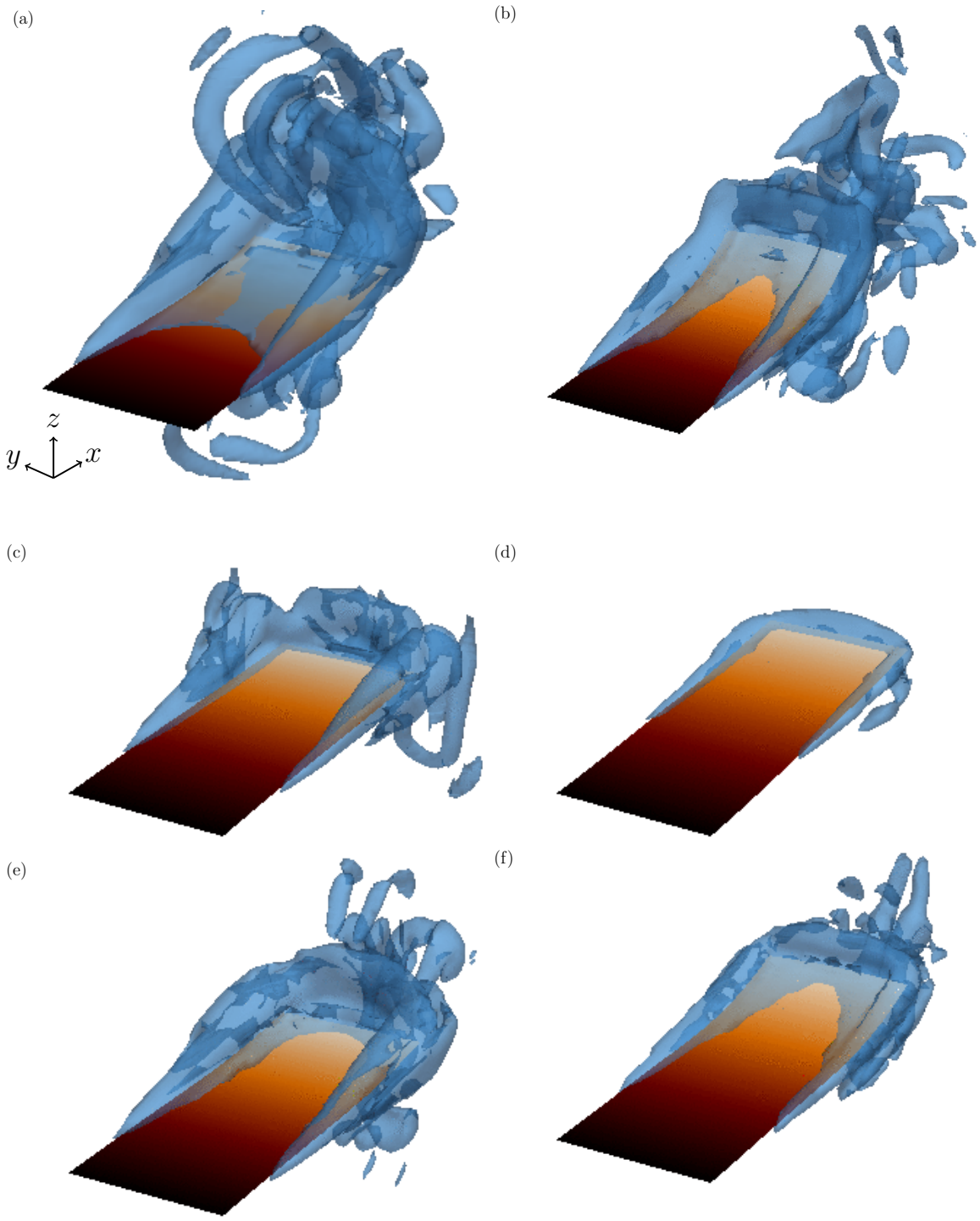

Figure 5.14: Normalized vorticity contours $\omega\tau = 20$ of the numerically simulated internally actuated plate with passive (a-b) exponential, (c-d) parabolic concave and (e-f) parabolic convex tapered attachments at maximum thrust and efficiency respectively for $r_h = 5$ and $L_h/L = 0.5$.

different types of passive tapered attachments. In figure 5.14a, we show the vorticity generated by the exponential tapered attachment at maximum thrust output. Due to the high tip displacement (figure 5.5) the plate produces a significant thrust; however, the significant side edge vortical structures demonstrate the poor energetic performance of this configuration. As can be seen by comparing the vorticity levels generated by the other attachments (5.14c and e), a high d_t is accompanied by a large $\mathcal{A}_{d,m}$, which results in significant $\mathcal{P}$. On the other hand, when we compare the vorticity contours at maximum efficiency (5.14b, d and f), the parabolic convex and concave attachments strongly stand out. The parabolic convex generates significantly more thrust due to a higher d_t with comparable $\mathcal{A}_{d,m}$ as illustrated by the comparable amount of SEV.

To further discriminate the performance between tapered attachments, we can rely on wave arguments. A "steeper" tapering leads to more time for the waves generated at the root to reach the tip of the tapered attachment, which is measured through the SWR. In figure 5.15a we plot the efficiency as a function of the SWR. There are two clear trends, at low SWR the spread of efficiency is significant, especially for the uniform attachment. Conversely, the efficiency scales directly with the SWR for SWR > 0.25. Indeed, when the SWR is low, any of the thrust, power or efficiency do not result from the acoustic black hole effect. For instance, if we consider the uniform passive attachment, the thrust, power and efficiency are mainly functions of the frequency ratio. Since the frequency ratio does not affect the SWR for the uniform and less pronounced tapering shapes, the SWR is not a good measure of the efficiency for these cases. On the other hand, as soon as the acoustic black hole effect is not negligible, the SWR is a good metric to predict high efficiency. At high enough SWR, the efficiency scales as $\eta \sim \text{SWR}^{0.15}$. This is further confirmed on figure 5.15b where we plot the relationship between η and the SWR for internally and externally actuated plates. In both instances, the SWR ratio remains an accurate measure of

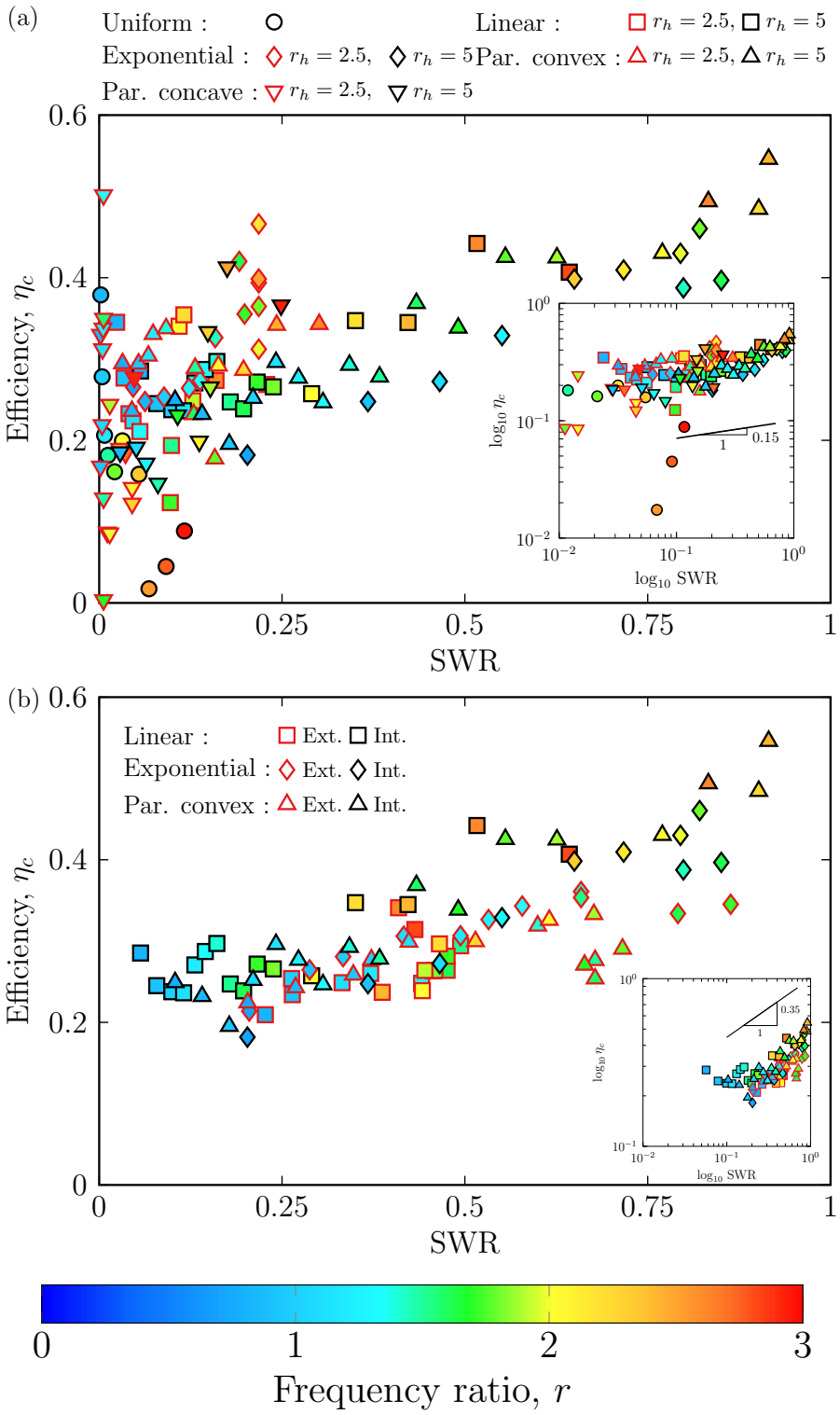

Figure 5.15: Relationship between the efficiency, frequency ratio r and SWR for (a) exclusively internally actuated plates with a passive tapered attachment for $r_h \in \{2.5, 5\}$ and (b) externally and internally actuated plates with a passive tapered attachment for $r_h = 5$ and $L_h/L = 0.5$.

the efficiency. Additionally, in opposition to the uniform plate in chapter 3, here the efficiency is not a strong function of the actuation method. This further demonstrates that the ABH is the principal mechanism defining the hydrodynamic performance. To summarize, optimizing the swimming performance requires maximizing the tip displacement, minimizing the displacement area and maximizing the SWR.

5.11 Optimization

To optimize the performance, the swimmer should maximize the efficiency and propulsion. Therefore, let us formally define the multi-objective function $\underline{J} = \left(-\eta_c - \overline{F}_x\right)^t$. The multi-objective optimization problem is then defined as

$$\min_{\substack{\underline{x}\in\mathcal{S} \\ \underline{g}(\underline{x})\leq 0 \\ \underline{h}(\underline{x})=0}} \underline{J}(\underline{x}) \tag{5.8}$$

where S is the set of feasible features and $\underline{g}$ and $\underline{h}$ are constraints. To evaluate $\underline{J}$ requires solving the FSI problem for each individual $\underline{x}$. This approach would be very costly computationally. Rather than solve the full FSI problem, we can take advantage of the knowledge on the scaling of the propulsion metrics with the plate's kinematics. Although the criteria presented in this chapter allow to estimate principal swimming metrics, we do not anticipate the tip displacement, displacement area and SWR to completely characterize the swimming performance. One can consider additional criteria such as the tip angle. Fortunately, additional criteria can be easily incorporated with the following optimization framework. Let us reformulate this problem as

$$\min_{\substack{\underline{x}\in\mathcal{S} \\ \underline{g}(\underline{x})\leq 0 \\ \underline{h}(\underline{x})=0}} \underline{G}(\underline{x}) \tag{5.9}$$

where $\underline{G} \in \mathbb{R}^m$ is another multi-objective function and m is the number of objectives. Here $\underline{G} = (-d_t \ \mathcal{A}_{d,m} \ - \text{SWR})^t$ is defined solely from the metrics previously established. Although at first glance it appears this optimization problem is more complex than the previous one with more criteria to optimize, $\underline{G}$ can be significantly cheaper to evaluate than $\underline{J}$. Indeed, rather than solving the full FSI problem, the plate kinematics can be computed with a simplified one-dimensional model. For an isotropic rectangular plate, the plate displacement can be approximated by the centerline displacement, in which case the reduced accuracy is compensated by the ability to explore a wide parameter space. The best design candidates are then validated by the three-dimensional model to confirm their performance *a posteriori*.

The one-dimensional model is based on the FD discretization of the Euler-Bernoulli beam equation

$$M_l \frac{\partial^2 w}{\partial t^2} = -\frac{\partial^2}{\partial x^2}\left(EI\,(x)\,\frac{\partial^2 w}{\partial x^2}\right) - \frac{1}{2}\rho W C_d \frac{\partial w}{\partial t}\left|\frac{\partial w}{\partial t}\right| \tag{5.10}$$

where $EI : x \longmapsto \frac{EWh^3}{12}$, C_d is a drag coefficient inferred from the three-dimensional model and h is constructed as in equation 5.1. Finally, since this is a multi-objective optimization problem different weights can be attributed to different criteria. Here, we keep the same unitary weight for each criterion.

5.11.1 Genetic Algorithm

An evolutionary genetic algorithm (EGA) is particularly tailored for this multi-objective optimization problem given the size of the parameter space. First, let us briefly discuss the principle of EGA. EGAs rely on mechanisms that mimic biological evolution such as crossover, mutation and selection. In the context of EGAs, features are referred to as genes. We select the tapering shape, tapering ratio, tip slope (for the parabolic cases), tapered length and frequency ratio as genes. Each gene can be

constrained to a feasible range. We define the following gene constraints

$$\begin{cases} h_{\text{shape}} & \in \{\text{uniform, linear, parabolic, exponential}\} \\ r_h & \in [0.1, 10] \\ \theta & \in [-0.5, 0.5] \\ L_h & \in [0, 1] \\ r & \in [0.1, 10] \end{cases} . \tag{5.11}$$

The vector containing the genes of an individual is called a chromosome $\underline{\mathcal{C}} = (h_{\text{shape}}\ r_h\ \theta\ L_h\ r)^t$. Any generic EGA follows this template :

1. Generate an initial population : $P_\mu = \{\underline{x}_1, \ldots, \underline{x}_\mu\}$ set of individuals with chromosome $\mathcal{C}_i$
2. Generate λ offspring forming the set $\widetilde{P}_\lambda = \{\widetilde{\underline{x}}_1, \ldots, \widetilde{\underline{x}}_\mu\}$. Each offspring $\widetilde{\underline{x}}$ is generated as follows :
   (a) Select ρ parents from P_μ
   (b) Recombine ρ parents to form an offspring
   (c) Mutate parts of the offspring's chromosome
3. Select new parent population from the offspring $\widetilde{P}_\lambda$ and parent P_μ population ($\mu + \lambda$ evolution strategy)
4. Repeat from step 2 until termination criterion fulfilled.

Selection is one of the most critical parts of an EGA. Before giving more details on the selection strategy, let us introduce a few additional concepts. In single-objective optimization, the superiority of a solution is easily determined by evaluating the objective function and comparing the cost function for an individual. In multi-objective

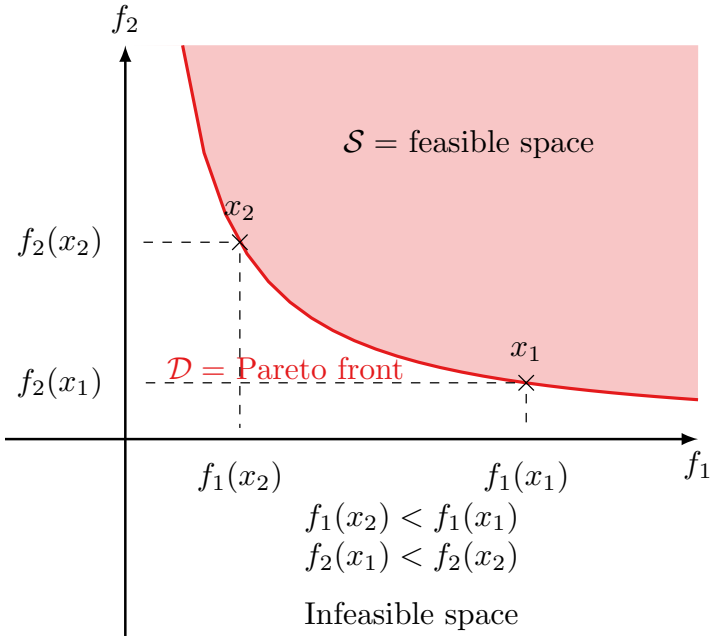

Figure 5.16: Illustration of Pareto dominance

optimization, the fitness of a solution is determined by dominance. An individual $\underline{x}_1$ dominates another individual $\underline{x}_2$ ($\underline{x}_1 \preceq \underline{x}_2$) if any of the objectives cannot be improved without worsening at least one of the other objectives or in mathematical terms:

$$\begin{cases} \forall\ i \in [\![1; m]\!]\ ,\ G_i\left(\underline{x}_1\right) \leq G_i\left(\underline{x}_2\right) \\ \exists\ j \in [\![1; m]\!] \setminus G_j\left(\underline{x}_1\right) < G_j\left(\underline{x}_2\right) \end{cases} \tag{5.12}$$

The set $\mathcal{D}$ formed of all non-dominated points is called the Pareto optimal set. The boundary defined by this set is called the Pareto front. We illustrate this concept in figure 5.16, if the goal is to minimize both f_1 and f_2 there is no global optimum but rather a set of solutions dominating any other feasible solution.

The goal of EGA is to best approach this Pareto front (PF). Here we used the NSGA-II [105] (non-dominated sorting genetic algorithm), a fast elitist algorithm, through the DEAP framework [106]. In an elitist algorithm, elites (best individuals)

Parameter	Symbol	Value
Number of generations	N_{gen}	$10^1 - 10^4$
Size of the population	N_{pop}	$10 - 10^2$
Number of individuals to select for next gen.	μ	N_{pop}
Number of offspring generated at each gen.	λ	N_{pop}
Probability of crossover	p_{cross}	0.5
Probability of mutation	p_{mut}	0.4
Standard deviation of mutation	σ_{mut}	0.1

Table 5.1: Genetic algorithm parameters

have a chance to be carried over each generation. Furthermore, NSGA-II preserves diversity through a mechanism called crowding distance. EGA parameters are summarized in table 5.1.

In this section we will only consider externally actuated plates with tapered attachments. Regarding the other simulation parameters, the mass ratio $\chi = 5$, overall length $L = 50$ LBU, aspect ratio $\mathcal{A}_R = 2.5$, Reynolds number $Re = 2000$ and actuation amplitude $A_0/L = 0.05$ are fixed. In figure 5.17 we plot the different Pareto fronts found by the EGA for various generations in the $d_t - \mathcal{A}_{d,m} - \text{SWR}$ space. The three-dimensional nature of the decision space somewhat impedes the interpretation of the EGA results.

To alleviate this problem, we show projections of the decision space in figures 5.18a and 5.19a. In figure 5.18a we plot d_t as a function of $\mathcal{A}_{d,m}$. The results from the multi-objective optimization shows an interesting trend. One would expect that a high d_t is inherently tied to a high $\mathcal{A}_{d,m}$. Indeed, this candid observation can be observed in the EGA results across diverse generations. For a limited number of iterations, the EGA struggles to find candidates with high d_t while minimizing $\mathcal{A}_{d,m}$. The majority of the population plateaus around $d_t/L = 0.05$ with a relatively low $\mathcal{A}_{d,m} \simeq 0.7$. Nevertheless, there is one individual yielding significant tip displacement ($d_t/L = 0.1$) for a low displacement area ($\mathcal{A}_{d,m} = 0.2$). As the number of generations increases, the number of individuals in the region of high d_t and low $\mathcal{A}_{d,m} = 0.2$

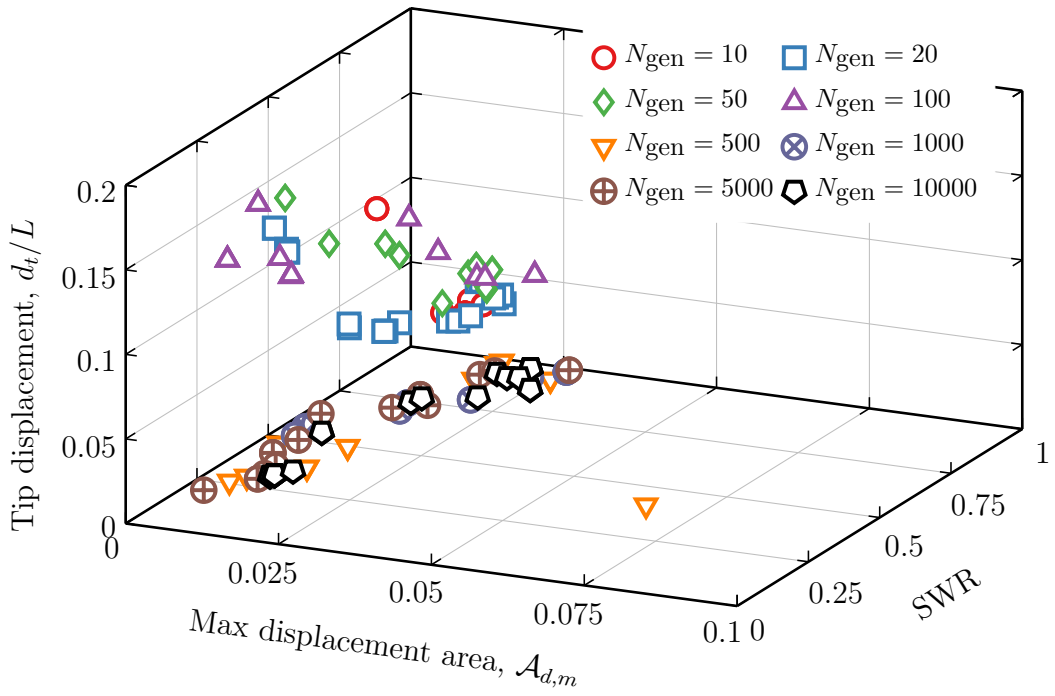

Figure 5.17: Pareto fronts resulting from the EGA in the $d_t - \mathcal{A}_{d,m} -$ SWR space across various generations for externally actuated plates.

increases significantly with more than 50% of the population yielding $d_t/L > 0.1$ and $\mathcal{A}_{d,m} \lesssim 0.5$. In figure 5.18b we plot the thickness profile of three of the best individuals in the $\mathcal{A}_{d,m} - d_t$ plane in addition to a sub-optimal candidate as a reference. The best individuals share common characteristics in their genome: a high tapering ratio $5 < r_h < 7$ in conjunction with steeper tapering shapes (exponential and parabolic convex) as well as a high frequency ratio $r > 3$. Interestingly, the individual sub-performing has a very similar genome, with only two significant deviations. Namely, the tapered length is almost twice as important as the optimal cases but more importantly the frequency ratio is three to four times smaller.

Let us cast aside thickness and wave theory arguments for a moment. First mode bending ($r \leq 1$) can maximize the tip displacement at resonance ($r = 1$); however, due to the nature of the bending patterns, it is inherently impossible to minimize the displacement area. Indeed, for first mode bending the plate displacement along the length increases (or decreases) monotonically along the length with a maximum

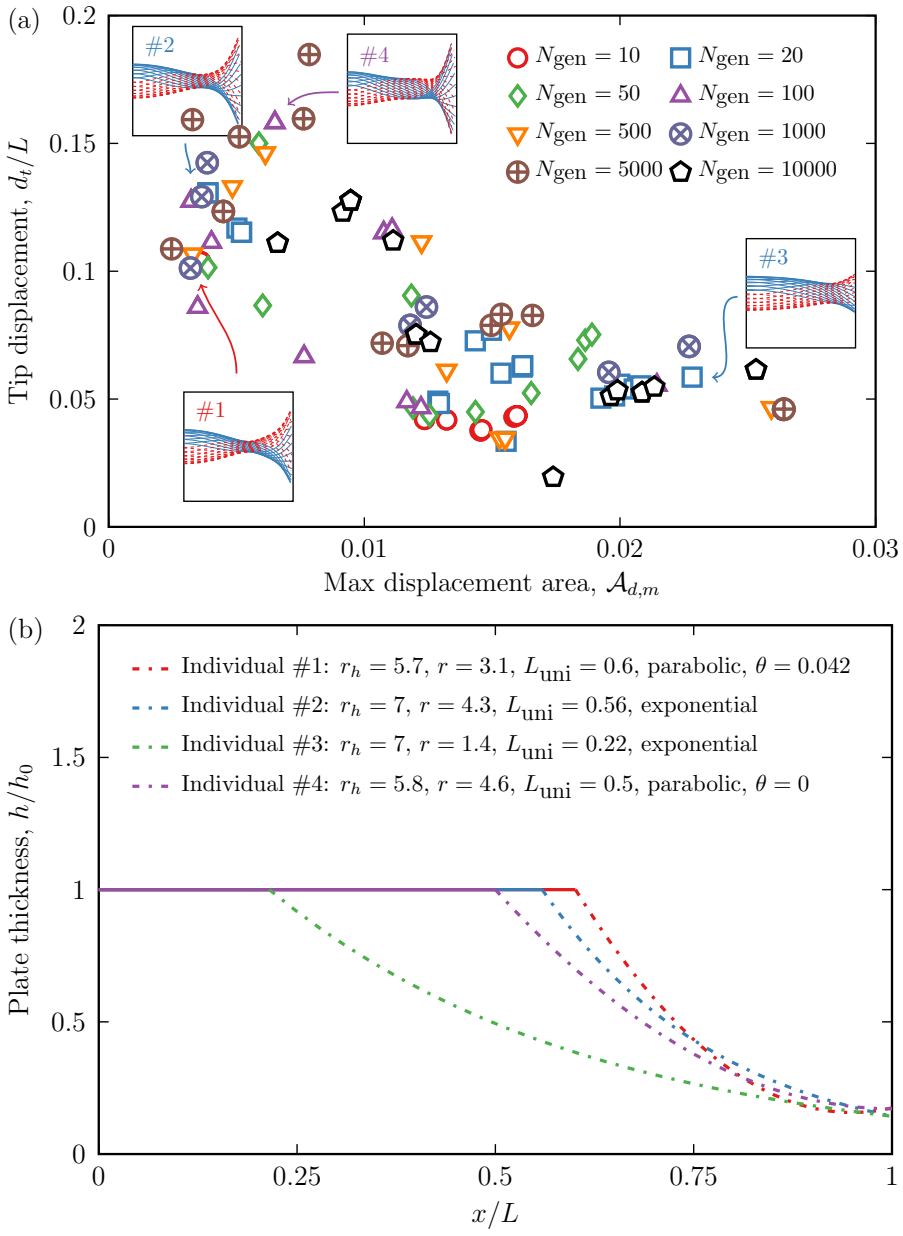

Figure 5.18: (a) Pareto fronts resulting from the EGA in the $\mathcal{A}_{d,m} - d_t$ plane across various generations for externally actuated plates. Insets show bending patterns of individuals 1 to 4. (b) Thickness profile of corresponding individuals.

at the tip; therefore, every segment of the plate adds up when integrated without compensation. As a consequence the displacement area $\mathcal{A}_{d,m}$ is maximum. This simple argumentation explains why the majority of individuals generated by the EGA have frequency ratios greater than 1, the tip displacement can be maximized but at the cost of maximizing the displacement area which we characterized as inefficient with our scaling laws.

Now, let us consider the effects due to the change in thickness. As shown in figure 5.5, plates with a decreasing stiffness effectively shift the higher mode resonance to lower frequencies which leads to an overlap of neighboring modes. This overlap results in a tip displacement increase off-resonance when compared to uniform plates and even a global maximum in the case of the exponential tapering shape. The bending patterns resulting from higher mode complexion are characterized by a non-monotonic variation of the displacement along the length, which in turn leads to a lower maximum displacement area, as can be seen in the patterns of individuals 1 to 4 in the insets in figure 5.18.

In figure 5.19a we plot the results of the EGA in the $d_t - \text{SWR}$ plane. For lower number of generations, the EGA maximizes the SWR however the tip displacement is limited. As the number of generations increases, the EGA manages to find individuals with higher tip displacement while maintaining a higher SWR. The insets in figure 5.19a show the bending patterns associated to particular individuals generated by the EGA. For instance, individual 1 from the tenth generation is a good candidate with a relatively high tip displacement ($d_t/L = 0.11$) and SWR ($\text{SWR} = 0.75$). Generally, higher SWR candidates such as individuals 1, 2 and 4 display similar bending patterns. As can be seen in figure 5.19b, all individuals have similar thickness profiles with the exception of individual 4 which displays a change of convexity. Nonetheless, the tapering ratio as well as the tapered length are comparable across all cases. Once more, the main differentiator is the frequency ratio r. Individuals 1, 2 and 4 (higher

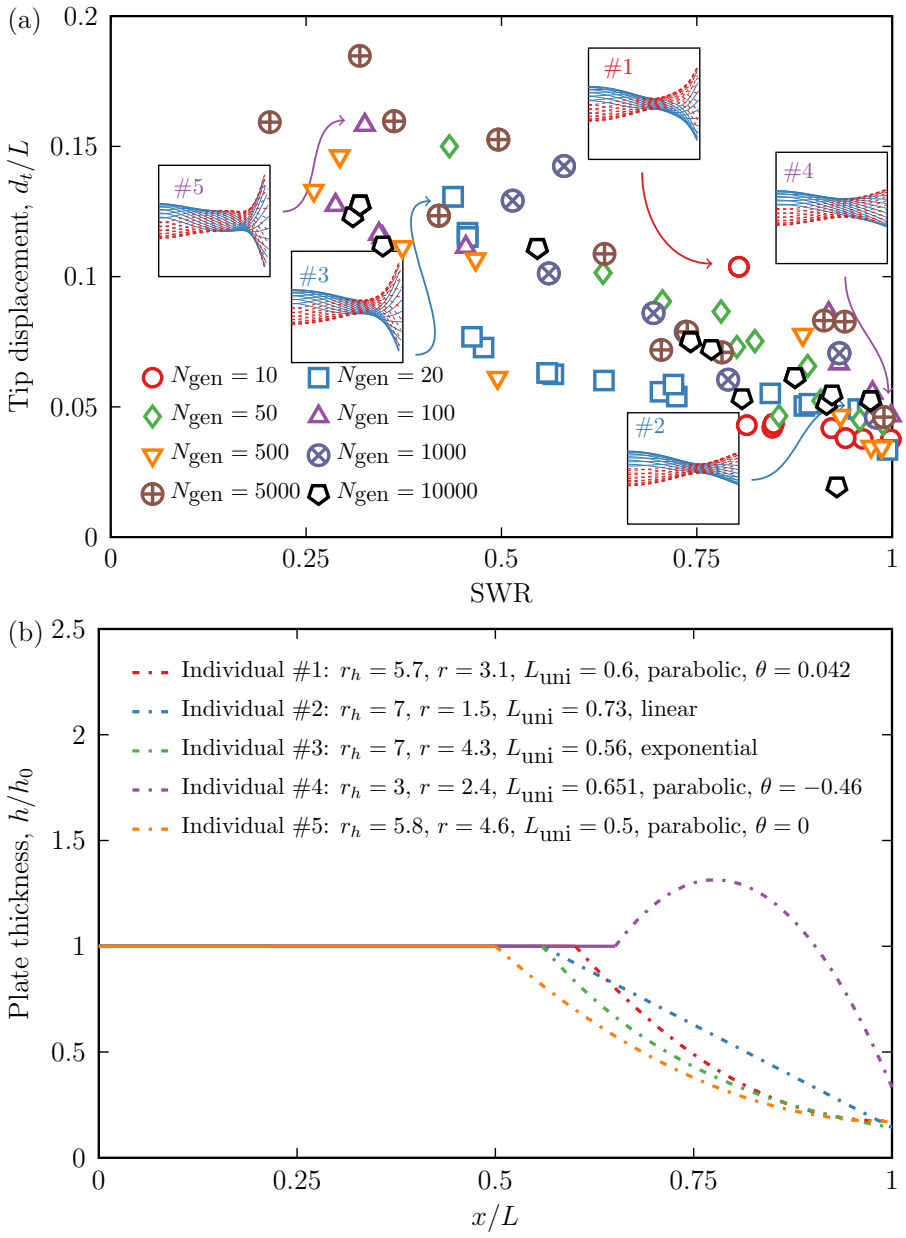

Figure 5.19: (a) Pareto fronts resulting from the EGA in the $d_t - \text{SWR}$ plane across various generations for externally actuated plates. Insets show bending patterns of individuals 1 to 5. (b) Thickness profile of corresponding individuals.

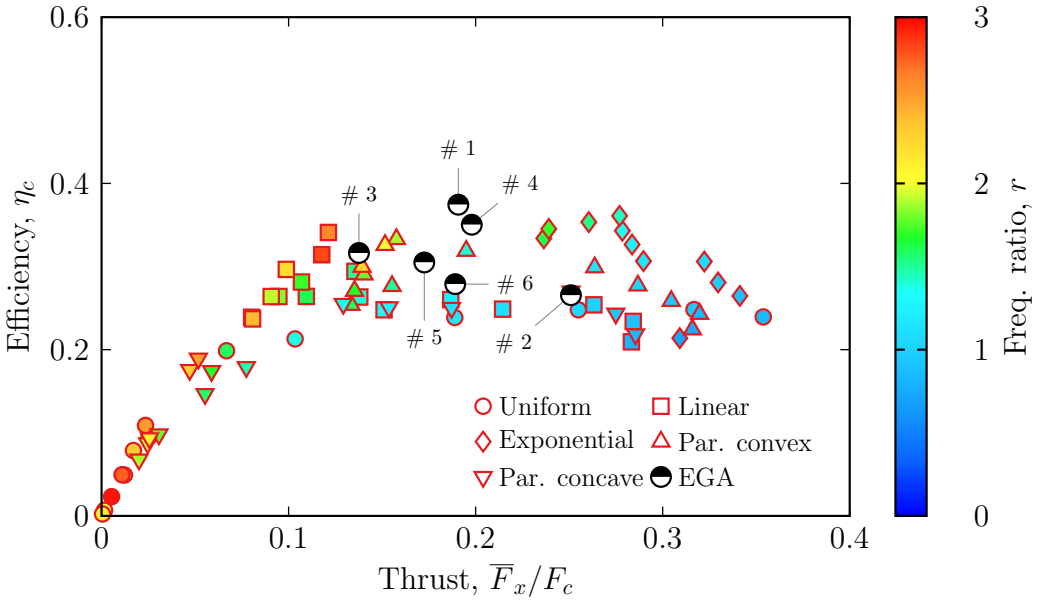

Figure 5.20: Comparison of various EGA individuals' performance (black half circles) versus non-optimized population in the $\eta_c - \overline{F}_x$ plane for externally actuated plates.

SWRs) have a moderate frequency ratio $1.3 < r < 3.1$, while poorer performers have higher r ($r > 4.3$). This observation is consistent with our previous simulations, the SWR increases with frequency ratio but there is a maximum at moderate $r \simeq 2 - 3$ depending on the tapering shape and ratio. Past this value the SWR decreases as the plate is closing to the second mode resonance.

So far, a one-dimensional model was optimized with modeled FSI. Although the optimization process is based on scaling laws derived from fully-coupled three-dimensional results, it is necessary to verify *a posteriori* the applicability of this simplified approach. In figure 5.20 we plot the efficiency as a function of the thrust for externally actuated plates with passive tapered attachments of various tapering shapes and some of the best individuals from the EGA. Although the EGA evaluates individuals with a modeled FSI, it produces highly efficient individuals producing significant thrust compared to the fully coupled FSI sequential approach. Moreover, individual 1 from the EGA actually outperforms every other data point with $\eta_c = 0.4$ and $\overline{F}_x/F_c = 0.2$. Overall, We draw a conclusion similar to our previous sequential

approach, however only a fraction of the parameter space could be explored. Here, solving this well-posed optimization problem further demonstrates that the balance between the tip displacement and displacement area, a key to achieve efficient propulsion, is intrinsically linked to the thickness tapering.

5.12 Summary

In summary, we find that elastic plates with passive tapered attachments can be tuned to offer a significant performance increase in both thrust and efficiency. We find that this enhanced performance is intrinsically connected to the nature of the wave propagating in the plate. We formally characterized this propagation through the standing wave ratio. Our results show that uniformly thick plates yield standing waves (low standing wave ratio) for a wide frequency range. By studying fish locomotion, standing wave-based propulsion is known to be generally less efficient than travelling wave propulsion. However, by introducing a tapering in the passive attachment, the plate can be tuned to shift from purely standing waves to almost purely travelling waves, especially for off-resonance actuation, thereby significantly increasing the propulsion efficiency. Indeed, the mass and stiffness gradients in the tapered attachment result in a shift of higher mode resonance to lower frequencies. Without the stiffness and mass gradients, the thrust and power input are low for post-resonance frequencies due to a minimal tip displacement. In the case of tapered attachments, the first and second resonance bands overlap which in turn increases the off-resonance tip displacement. The steeper the tapering, the more pronounced the overlap is. Therefore, not only the energetic performance but also the thrust can both be optimized past the first mode resonance which results in highly efficient propulsion.

Furthermore, by exploring the consequent parameter space we demonstrate that the thrust and power directly scale with the tip displacement and maximum displacement area, respectively. The thrust scaling can be seen as a direct consequence of

Lighthill's theory [35] who showed that the thrust is completely characterized by the tip kinematics for the oscillation of a beam in an inviscid fluid. However, we show that this observation holds true for plate oscillating in a viscous fluid at moderate Re. Accordingly, the efficiency defined as the ratio of the thrust and power is found to scale directly with the ratio of maximum displacement area to tip displacement $\mathcal{A}_{d,m}/d_t$, the lower this ratio the higher is the efficiency.

Deriving these scaling laws is primordial to evaluating propulsor designs at low computational cost. Indeed, the cost of evaluating the performance of a plate candidate with a fully-coupled three-dimensional FSI simulation prevents a thorough exploration of the vast parameter space. However, by solving a simpler problem and using the knowledge inferred by fully coupled simulations through scaling laws, the cost of evaluating the fitness of a propulsor significantly decreases with an insignificant decrease of the accuracy. As a proof of concept, we show that a simple 1D tapered beam model associated to an evolutionary genetic algorithm allows for efficient and accurate exploration of the parameter space. The accuracy of this process is validated *a posteriori* by evaluating candidates with the full-fledged three-dimensional approach. With this simple approach, the EGA is able to find designs outperforming every counterpart obtained through the conventional "blind" approach.

CHAPTER 6
CONCLUDING REMARKS AND OUTLOOK

In this work, we used a three-dimensional fully-coupled fluid-structure interaction framework to study the hydrodynamics of a bio-inspired propulsor. The bio-inspired propulsor, which represents the motion of a fish fin to certain level of abstraction, is modeled by an elastic plate oscillating in a Newtonian fluid. We conducted several studies with different actuation methods, non-uniform properties, various Reynolds numbers, mass and aspect ratios, to probe how to maximize certain swimming metrics such as the propulsion and efficiency and to develop an understanding of the underlying physics.

We first investigated the effects of two different actuation methods: an external actuation based on conventional heaving propulsors and an internal actuation based on a muscle-like activation. This internal moment represents the functioning of macro-fiber composites, a smart material based on piezo-electric actuators which has been found to offer great balance between actuation and deformation levels. We identified differences in the bending patterns yielded by these two actuation methods. Namely, the internal actuation results in a cupping towards the tip of the plate which we formally characterized by examining the plate curvature. This cupping results in less fluid pushed backwards which in turns yields less thrust. Moreover, the cupping generates more viscous dissipation resulting in an overall less efficient propulsion. We further explored the effects of the flow regime by varying the Reynolds number. We found that the propulsion efficiency is an increasing function of the Reynolds number. In addition to differences in swimming metrics, we found that the actuation methods have a direct impact on the inertia coefficient, an empirical coefficient defined by Morison [84] and used to design flexible structures immersed in a fluid. While the

inertia coefficient is known to be a function of the Reynolds number, mass and aspect ratio, we showed that it is a strong function of the actuation method which is a critical result for the design of underwater swimmers.

After systematically studying the impact of these two actuation methods on the propulsor performance, we probed the effects of combining the external and internal actuation. Results showed that the principal swimming metrics could be modulated by introducing a phase lag between the external and internal actuation signals. Moreover, we found that the performance of the combined actuation significantly outperforms either internal or external actuation in both propulsion and efficiency. This enhanced performance is due to the unique capacity of the hybrid actuation to balance the tip and center of mass, which are found to directly scale with the propulsion and power respectively.

Finally, we investigated the effects of non-homogeneous mechanical properties by adding passive tapered attachments to internally and externally actuated plates of constant thickness. Our results showed that augmenting a uniform plate with a tapered passive attachment significantly enhances the thrust and efficiency performance over a wide range of driving frequencies. The thrust was found to be maximized by the exponential passive attachment with up to six times the nominal value of a uniform plate while driven at 1.7 times the first resonance frequency. Similarly, the efficiency was found to be maximum for a parabolic convex tapered attachment driven at 2.4 times the first resonance frequency. We found that the enhanced performance is directly linked to two concepts. First, the mass and stiffness gradient in the tapered attachment results in a shift of higher mode resonance frequencies which in turn yields an overlap between first and second mode resonance. This overlap leads to higher tip displacement and thrust while maintaining a low maximum beat area, a measure of the virtual mass displaced by the plate and found to scale directly with the power. In addition to this consideration, we found the plate performance to be intrinsically

characterized by the nature of the waves propagating in the plate. Indeed, travelling wave-based propulsion has been known to be more efficient than its standing wave counterpart. We formally demonstrated that this observation is due to a well-known acoustic phenomenon, the acoustic black hole. The stiffness gradient in the tapered attachment results in an increased time for waves generated at the root of the plate to reach the tip of the tapered attachment. This in turn results in non-overlapping incident and reflected waves which is how travelling waves are maintained. In order to efficiently explore the colossal parameter space, we derived scaling laws from our fully-coupled FSI model to feed into a simpler beam model coupled to an evolutionary genetic algorithm. With this simple approach, the EGA succeeded in finding plate designs outperforming every candidate found by the sequential "blind" approach at a significantly lower computational cost.

The results from this research are important for the design of small to moderate scale bio-inspired swimmers using elastic elements to create propulsion. Although several strategies were explored for improving propulsion and swimming efficiency, an investigation of strategies to perform turning maneuvers is still far from being completed. Indeed, the ability to change the direction of the force resultant makes smart materials, and particularly MFCs, a great candidate to achieve fast and efficient turning. Furthermore, in this work we solely focused on steady-state propulsion, an important part of fish swimming lays on fast bursts, which are inherently transient phenomena, such a C-starts. Furthermore, our numerical model is confined to solely represent the swimmer fins, the inclusion of the swimmer body needs to be considered for better understanding of swimmer propulsion. Although our results apply mainly to the design of simple bio-inspired propulsors, they provide insight on why fish in nature rely on various swimming modes as well as non-homogeneous properties and their impact on the waves propagating through their elastic bodies.

REFERENCES

[1] F. Fish and G. V. Lauder, "Passive and active flow control by swimming fishes and mammals," *Annu. Rev. Fluid Mech.*, vol. 38, pp. 193–224, 2006.

[2] B. C. Jayne and G. V. Lauder, "Speed effects on midline kinematics during steady undulatory swimming of largemouth bass, micropterus salmoides," *Journal of Experimental Biology*, vol. 198, no. 2, pp. 585–602, 1995.

[3] G. V. Lauder and E. D. Tytell, "Hydrodynamics of undulatory propulsion," *Fish physiology*, vol. 23, pp. 425–468, 2005.

[4] M. J. McHenry, C. A. Pell, and J. Long, "Mechanical control of swimming speed: Stiffness and axial wave form in undulating fish models," *Journal of Experimental Biology*, vol. 198, no. 11, pp. 2293–2305, 1995.

[5] M. Sfakiotakis, D. M. Lane, and J. B. C. Davies, "Review of fish swimming modes for aquatic locomotion," *IEEE Journal of oceanic engineering*, vol. 24, no. 2, pp. 237–252, 1999.

[6] S. A. Combes and T. L. Daniel, "Shape, flapping and flexion: Wing and fin design for forward flight," *Journal of Experimental Biology*, vol. 204, no. 12, pp. 2073–2085, 2001. eprint: `https://jeb.biologists.org/content/204/12/2073.full.pdf`.

[7] H Liu and H. Aono, "Size effects on insect hovering aerodynamics: An integrated computational study," *Bioinspiration & Biomimetics*, vol. 4, no. 1, p. 015 002, 2009.

[8] D. Kolomenskiy, H. K. Moffatt, M. Farge, and K. Schneider, "The lighthill–weis-fogh clap–fling–sweep mechanism revisited," *Journal of Fluid Mechanics*, vol. 676, 572–606, 2011.

[9] S. Alben, C. Witt, T. V. Baker, E. Anderson, and G. V. Lauder, "Dynamics of freely swimming flexible foils," *Physics of Fluids*, vol. 24, no. 5, p. 051 901, 2012.

[10] J. Yu, M. Tan, S. Wang, and E. Chen, "Development of a biomimetic robotic fish and its control algorithm," *IEEE Transactions on Systems, Man, and Cybernetics, Part B (Cybernetics)*, vol. 34, no. 4, pp. 1798–1810, 2004.

[11] S. Marras and M. Porfiri, "Fish and robots swimming together: Attraction towards the robot demands biomimetic locomotion," *Journal of The Royal Society Interface*, vol. 9, no. 73, pp. 1856–1868, 2012.

[12] H. Hu, J. Liu, I. Dukes, and G. Francis, "Design of 3d swim patterns for autonomous robotic fish," in *2006 IEEE/RSJ International Conference on Intelligent Robots and Systems*, 2006, pp. 2406–2411.

[13] V. Kopman, J. Laut, F. Acquaviva, A. Rizzo, and M. Porfiri, "Dynamic modeling of a robotic fish propelled by a compliant tail," *IEEE Journal of Oceanic Engineering*, vol. 40, no. 1, pp. 209–221, 2015.

[14] Z. Chen, T. I. Um, J. Zhu, and H. Bart-Smith, "Bio-inspired robotic cownose ray propelled by electroactive polymer pectoral fin," in *ASME 2011 international mechanical engineering congress and exposition*, American Society of Mechanical Engineers Digital Collection, 2011, pp. 817–824.

[15] M. Philen and W. Neu, "Hydrodynamic analysis, performance assessment, and actuator design of a flexible tail propulsor in an artificial alligator," *Smart Materials and Structures*, vol. 20, no. 9, p. 094 015, 2011.

[16] M. S. Triantafyllou and G. S. Triantafyllou, "An efficient swimming machine," *Scientific american*, vol. 272, no. 3, pp. 64–70, 1995.

[17] J. Anderson, K Streitlien, D. Barrett, and M. Triantafyllou, "Oscillating foils of high propulsive efficiency," 1998.

[18] Z. Su, J. Yu, M. Tan, and J. Zhang, "Implementing flexible and fast turning maneuvers of a multijoint robotic fish," *IEEE/ASME Transactions on Mechatronics*, vol. 19, no. 1, pp. 329–338, 2014.

[19] G. V. Lauder and J. L. Tangorra, "Fish locomotion: Biology and robotics of body and fin-based movements," in *Robot Fish: Bio-inspired Fishlike Underwater Robots*, R. Du, Z. Li, K. Youcef-Toumi, and P. Valdivia y Alvarado, Eds. Berlin, Heidelberg: Springer Berlin Heidelberg, 2015, pp. 25–49, ISBN: 978-3-662-46870-8.

[20] C. J. Esposito, J. L. Tangorra, B. E. Flammang, and G. V. Lauder, "A robotic fish caudal fin: Effects of stiffness and motor program on locomotor performance," *Journal of Experimental Biology*, vol. 215, no. 1, pp. 56–67, 2012. eprint: `https://jeb.biologists.org/content/215/1/56.full.pdf`.

[21] B. E. Flammang and G. V. Lauder, "Caudal fin shape modulation and control during acceleration, braking and backing maneuvers in bluegill sunfish, lepomis

macrochirus," *Journal of Experimental Biology*, vol. 212, no. 2, pp. 277–286, 2009. eprint: `https://jeb.biologists.org/content/212/2/277.full.pdf`.

[22] Z. Chen, S. Shatara, and X. Tan, "Modeling of biomimetic robotic fish propelled by an ionic polymer–metal composite caudal fin," *IEEE/ASME transactions on mechatronics*, vol. 15, no. 3, pp. 448–459, 2009.

[23] Y. Cha, H. Kim, and M. Porfiri, "Energy harvesting from underwater base excitation of a piezoelectric composite beam," *Smart materials and Structures*, vol. 22, no. 11, p. 115 026, 2013.

[24] O. Rediniotis, L. Wilson, D. C. Lagoudas, and M. Khan, "Development of a shape-memory-alloy actuated biomimetic hydrofoil," *Journal of Intelligent Material Systems and Structures*, vol. 13, no. 1, pp. 35–49, 2002.

[25] J. J. Hubbard, M. Fleming, V. Palmre, D. Pugal, K. J. Kim, and K. K. Leang, "Monolithic ipmc fins for propulsion and maneuvering in bioinspired underwater robotics," *IEEE Journal of Oceanic Engineering*, vol. 39, no. 3, pp. 540–551, 2013.

[26] X. Tan, D. Kim, N. Usher, D. Laboy, J. Jackson, A. Kapetanovic, J. Rapai, B. Sabadus, and X. Zhou, "An autonomous robotic fish for mobile sensing," in *2006 IEEE/RSJ International Conference on Intelligent Robots and Systems*, IEEE, 2006, pp. 5424–5429.

[27] Z. Wang, G. Hang, Y. Wang, J. Li, and W. Du, "Embedded SMA wire actuated biomimetic fin: A module for biomimetic underwater propulsion," *Smart Materials and Structures*, vol. 17, no. 2, p. 025 039, 2008.

[28] N. Shinjo and G. W. Swain, "Use of a shape memory alloy for the design of an oscillatory propulsion system," *IEEE Journal of Oceanic Engineering*, vol. 29, no. 3, pp. 750–755, 2004.

[29] S. Guo, Y. Ge, L. Li, and S. Liu, "Underwater swimming micro robot using ipmc actuator," in *2006 International Conference on Mechatronics and Automation*, IEEE, 2006, pp. 249–254.

[30] L Cen and A Erturk, "Bio-inspired aquatic robotics by untethered piezohydroelastic actuation," *Bioinspiration & Biomimetics*, vol. 8, no. 1, p. 016 006, 2013.

[31] S. Heo, T. Wiguna, H. C. Park, and N. S. Goo, "Effect of an artificial caudal fin on the performance of a biomimetic fish robot propelled by piezoelectric actuators," *Journal of Bionic Engineering*, vol. 4, no. 3, pp. 151–158, 2007.

[32] H. Li, C. Tian, J. Lu, M. J. Myjak, J. J. Martinez, R. S. Brown, and Z. D. Deng, "An energy harvesting underwater acoustic transmitter for aquatic animals," *Scientific reports*, vol. 6, no. 1, pp. 1–9, 2016.

[33] A. Erturk and G. Delporte, "Underwater thrust and power generation using flexible piezoelectric composites: An experimental investigation toward self-powered swimmer-sensor platforms," *Smart materials and Structures*, vol. 20, no. 12, p. 125 013, 2011.

[34] M. J. Lighthill, "Note on the swimming of slender fish," *Journal of Fluid Mechanics*, vol. 9, no. 2, 305–317, 1960.

[35] ——, "Aquatic animal propulsion of high hydromechanical efficiency," *Journal of Fluid Mechanics*, vol. 44, no. 2, 265–301, 1970.

[36] M. J. Lighthill, "Large-amplitude elongated-body theory of fish locomotion," *Proceedings of the Royal Society of London. Series B. Biological Sciences*, vol. 179, no. 1055, pp. 125–138, 1971. eprint: `https://royalsocietypublishing.org/doi/pdf/10.1098/rspb.1971.0085`.

[37] T. Y.-T. Wu, "Swimming of a waving plate," *Journal of Fluid Mechanics*, vol. 10, no. 3, 321–344, 1961.

[38] F.-J. Elmer and M. Dreier, "Eigenfrequencies of a rectangular atomic force microscope cantilever in a medium," *Journal of Applied Physics*, vol. 81, no. 12, pp. 7709–7714, 1997. eprint: `https://doi.org/10.1063/1.365379`.

[39] C. A. Van Eysden and J. E. Sader, "Resonant frequencies of a rectangular cantilever beam immersed in a fluid," *Journal of Applied Physics*, vol. 100, no. 11, p. 114 916, 2006. eprint: `https://aip.scitation.org/doi/pdf/10.1063/1.2401053`.

[40] S. Ramananarivo, R. Godoy-Diana, and B. Thiria, "Passive elastic mechanism to mimic fish-muscle action in anguilliform swimming," *Journal of The Royal Society Interface*, vol. 10, no. 88, p. 20 130 667, 2013.

[41] M Aureli, M. Basaran, and M. Porfiri, "Nonlinear finite amplitude vibrations of sharp-edged beams in viscous fluids," *Journal of sound and vibration*, vol. 331, no. 7, pp. 1624–1654, 2012.

[42] A. L. Facci and M. Porfiri, "Analysis of three-dimensional effects in oscillating cantilevers immersed in viscous fluids," *Journal of Fluids and Structures*, vol. 38, pp. 205–222, 2013.

[43] D. B. Quinn, G. V. Lauder, and A. J. Smits, "Scaling the propulsive performance of heaving flexible panels," *Journal of fluid mechanics*, vol. 738, pp. 250–267, 2014.

[44] A. P. Hoover, R. Cortez, E. D. Tytell, and L. J. Fauci, "Swimming performance, resonance and shape evolution in heaving flexible panels," *Journal of Fluid Mechanics*, vol. 847, pp. 386–416, 2018.

[45] I. Borazjani and F. Sotiropoulos, "Numerical investigation of the hydrodynamics of carangiform swimming in the transitional and inertial flow regimes," *Journal of experimental biology*, vol. 211, no. 10, pp. 1541–1558, 2008.

[46] A. P. S. Bhalla, R. Bale, B. E. Griffith, and N. A. Patankar, "A unified mathematical framework and an adaptive numerical method for fluid–structure interaction with rigid, deforming, and elastic bodies," *Journal of Computational Physics*, vol. 250, pp. 446–476, 2013.

[47] H. Dai, H. Luo, P. J. F. de Sousa, and J. F. Doyle, "Thrust performance of a flexible low-aspect-ratio pitching plate," *Physics of Fluids*, vol. 24, no. 10, p. 101 903, 2012.

[48] C. Eloy and L. Schouveiler, "Optimisation of two-dimensional undulatory swimming at high reynolds number," *International Journal of Non-Linear Mechanics*, vol. 46, no. 4, pp. 568–576, 2011.

[49] P. D. Yeh and A. Alexeev, "Free swimming of an elastic plate plunging at low reynolds number," *Physics of Fluids*, vol. 26, no. 5, p. 053 604, 2014.

[50] P. D. Yeh and A. Alexeev, "Biomimetic flexible plate actuators are faster and more efficient with a passive attachment," *Acta Mechanica Sinica*, vol. 32, no. 6, pp. 1001–1011, 2016.

[51] P. D. Yeh and A. Alexeev, "Effect of aspect ratio in free-swimming plunging flexible plates," *Computers & Fluids*, vol. 124, pp. 220–225, 2016.

[52] A. Alexeev, R. Verberg, and A. C. Balazs, "Modeling the motion of microcapsules on compliant polymeric surfaces," *Macromolecules*, vol. 38, no. 24, pp. 10 244–10 260, 2005. eprint: `https://doi.org/10.1021/ma05161`.

[53] A. Alexeev and A. C. Balazs, "Designing smart systems to selectively entrap and burst microcapsules," *Soft Matter*, vol. 3, no. 12, pp. 1500–1505, 2007.

[54] A. Ladd and R Verberg, "Lattice-boltzmann simulations of particle-fluid suspensions," *Journal of statistical physics*, vol. 104, no. 5-6, pp. 1191–1251, 2001.

[55] Y.-H. Dong, P. Sagaut, and S. Marie, "Inertial consistent subgrid model for large-eddy simulation based on the lattice boltzmann method," *Physics of Fluids*, vol. 20, no. 3, p. 035 104, 2008.

[56] S. Timoshenko and S. Woinowsky-Krieger, *Theory of Plates and Shells*, ser. Engineering mechanics series. McGraw-Hill, 1959.

[57] G. Kirchhoff, *Über das Gleichgewicht und die Bewegung einer elastischen Scheibe.* 1850.

[58] W. Mao, "Modeling particle suspensions using lattice boltzmann method," Ph.D. dissertation, Georgia Institute of Technology, 2013.

[59] S. Alben, A. A. Gorodetsky, D. Kim, and R. D. Deegan, "Semi-implicit methods for the dynamics of elastic sheets," *Journal of Computational Physics*, vol. 399, p. 108 952, 2019.

[60] J. Wu and C. K. Aidun, "Simulating 3d deformable particle suspensions using lattice boltzmann method with discrete external boundary force," *International journal for numerical methods in fluids*, vol. 62, no. 7, pp. 765–783, 2010.

[61] M. Desbrun, P. Schröder, and A. Barr, "Interactive animation of structured deformable objects," in *Graphics Interface*, vol. 99, 1999, p. 10.

[62] Y.-M. Kang, J.-H. Choi, H.-G. Cho, and C.-J. Park, "Fast and stable animation of cloth with an approximated implicit method," in *Proceedings Computer Graphics International 2000*, IEEE, 2000, pp. 247–255.

[63] A. Guckenberger, M. P. Schraml, P. G. Chen, M. Leonetti, and S. Gekle, "On the bending algorithms for soft objects in flows," *Computer Physics Communications*, vol. 207, pp. 1–23, 2016.

[64] G. Guennebaud, B. Jacob, *et al.*, *Eigen v3*, http://eigen.tuxfamily.org, 2010.

[65] H. Masoud and A. Alexeev, "Resonance of flexible flapping wings at low reynolds number," *Phys. Rev. E*, vol. 81, p. 056 304, 5 2010.

[66] ——, "Modeling magnetic microcapsules that crawl in microchannels," *Soft Matter*, vol. 6, no. 4, pp. 794–799, 2010.

[67] Z. G. Mills, B. Aziz, and A. Alexeev, "Beating synthetic cilia enhance heat transport in microfluidic channels," *Soft Matter*, vol. 8, no. 45, pp. 11 508–11 513, 2012.

[68] W. Mao and A. Alexeev, "Motion of spheroid particles in shear flow with inertia," *Journal of Fluid Mechanics*, vol. 749, 145–166, 2014.

[69] P. D. Yeh, Y. Li, and A. Alexeev, "Efficient swimming using flexible fins with tapered thickness," *Phys. Rev. Fluids*, vol. 2, p. 102 101, 10 2017.

[70] P. D. Yeh, E. Demirer, and A. Alexeev, "Turning strategies for plunging elastic plate propulsor," *Phys. Rev. Fluids*, vol. 4, p. 064 101, 6 2019.

[71] T. Engels, "Numerical modeling of fluid-structure interaction in bio-inspired propulsion," Ph.D. dissertation, Aix-Marseille, 2015.

[72] U. Küttler and W. A. Wall, "Fixed-point fluid–structure interaction solvers with dynamic relaxation," *Computational mechanics*, vol. 43, no. 1, pp. 61–72, 2008.

[73] A. Quaini and A. Quarteroni, "A semi-implicit approach for fluid-structure interaction based on an algebraic fractional step method," *Mathematical models and methods in applied sciences*, vol. 17, no. 06, pp. 957–983, 2007.

[74] S. Dong and G. E. Karniadakis, "Dns of flow past a stationary and oscillating cylinder at re= 10000," *Journal of fluids and structures*, vol. 20, no. 4, pp. 519–531, 2005.

[75] R. Gopalkrishnan, "Vortex-induced forces on oscillating bluff cylinders," Woods Hole Oceanographic Institution MA, Tech. Rep., 1993.

[76] W. Weaver Jr, S. P. Timoshenko, and D. H. Young, *Vibration problems in engineering*. John Wiley & Sons, 1990.

[77] S. Michelin and S. G. Llewellyn Smith, "Resonance and propulsion performance of a heaving flexible wing," *Physics of Fluids*, vol. 21, no. 7, p. 071 902, 2009.

[78] S. Alben, "On the swimming of a flexible body in a vortex street," *Journal of fluid mechanics*, vol. 635, pp. 27–45, 2009.

[79] J. C. Nauen and G. V. Lauder, "Hydrodynamics of caudal fin locomotion by chub mackerel, scomber japonicus (scombridae)," *Journal of Experimental Biology*, vol. 205, no. 12, pp. 1709–1724, 2002.

[80] F. Paraz, L. Schouveiler, and C. Eloy, "Thrust generation by a heaving flexible foil: Resonance, nonlinearities, and optimality," *Physics of Fluids*, vol. 28, no. 1, p. 011 903, 2016.

[81] J. Weiss, "The dynamics of enstrophy transfer in two-dimensional hydrodynamics," *Physica D: Nonlinear Phenomena*, vol. 48, no. 2-3, pp. 273–294, 1991.

[82] V Raspa, S Ramananarivo, B Thiria, and R Godoy-Diana, "Vortex-induced drag and the role of aspect ratio in undulatory swimmers," *Physics of Fluids*, vol. 26, no. 4, p. 041 701, 2014.

[83] G. G. Stokes *et al.*, *On the effect of the internal friction of fluids on the motion of pendulums*. Pitt Press Cambridge, 1851, vol. 9.

[84] J. Morison, M. O'brien, J. Johnson, and S. Schaaf, *The force exerted by surface waves on piles, petroleum transactions, a. 1*, 1950.

[85] S. Shahab, D. Tan, and A. Erturk, "Hydrodynamic thrust generation and power consumption investigations for piezoelectric fins with different aspect ratios," *The European Physical Journal Special Topics*, vol. 224, no. 17-18, pp. 3419–3434, 2015.

[86] E. Demirer, Y.-C. Wang, A. Erturk, and A. Alexeev, "Effect of actuation method on hydrodynamics of elastic plates oscillating at resonance," *Journal of Fluid Mechanics*, vol. 910, 2021.

[87] S. Ramananarivo, R. Godoy-Diana, and B. Thiria, "Rather than resonance, flapping wing flyers may play on aerodynamics to improve performance," *Proceedings of the National Academy of Sciences*, vol. 108, no. 15, pp. 5964–5969, 2011. eprint: `https://www.pnas.org/content/108/15/5964.full.pdf`.

[88] Z Cui, Z. Yang, L. Shen, and H. Jiang, "Complex modal analysis of the movements of swimming fish propelled by body and/or caudal fin," *Wave motion*, vol. 78, pp. 83–97, 2018.

[89] J Gray, "Studies in animal locomotion: I. the movement of fish with special reference to the eel," *Journal of experimental biology*, vol. 10, no. 1, pp. 88–104, 1933.

[90] G. Bowtell and T. Williams, "Anguilliform body dynamics: Modelling the interaction between muscle activation and body curvature," *Philosophical Transactions of the Royal Society of London. Series B: Biological Sciences*, vol. 334, no. 1271, pp. 385–390, 1991.

[91] H. Hariri, Y. Bernard, and A. Razek, "A traveling wave piezoelectric beam robot," *Smart Materials and Structures*, vol. 23, no. 2, p. 025 013, 2013.

[92] M. Mironov, *Propagation of a flexural wave in a plate whose thickness decreases smoothly to zero in a finite interval*, 1988.

[93] V. Krylov and F. Tilman, "Acoustic 'black holes' for flexural waves as effective vibration dampers," *Journal of Sound and Vibration*, vol. 274, no. 3-5, pp. 605–619, 2004.

[94] P. A. Feurtado, S. C. Conlon, and F. Semperlotti, "A normalized wave number variation parameter for acoustic black hole design," *The Journal of the Acoustical Society of America*, vol. 136, no. 2, EL148–EL152, 2014.

[95] S. C. Conlon, J. B. Fahnline, and F. Semperlotti, "Numerical analysis of the vibroacoustic properties of plates with embedded grids of acoustic black holes," *The Journal of the Acoustical Society of America*, vol. 137, no. 1, pp. 447–457, 2015.

[96] E. Bowyer and V. V. Krylov, "Experimental study of sound radiation by plates containing circular indentations of power-law profile," *Applied Acoustics*, vol. 88, pp. 30–37, 2015.

[97] L. Zhao, S. C. Conlon, and F. Semperlotti, "An experimental study of vibration based energy harvesting in dynamically tailored structures with embedded acoustic black holes," *Smart Materials and Structures*, vol. 24, no. 6, p. 065 039, 2015.

[98] J. Liouville, "Mémoire sur le développement des fonctions ou parties de fonctions en séries dont les divers termes sont assujétis à satisfaire à une même équation différentielle du second ordre, contenant un paramètre variable.," *Journal de mathématiques pures et appliquées*, pp. 253–265, 1836.

[99] G. Green *et al.*, "On the motion of waves in a variable canal of small depth and width," *Transactions of the Cambridge Philosophical Society*, vol. 6, p. 457, 1838.

[100] G. Wentzel, "Eine verallgemeinerung der quantenbedingungen für die zwecke der wellenmechanik," *Zeitschrift für Physik*, vol. 38, no. 6-7, pp. 518–529, 1926.

[101] L. Brillouin, "La mécanique ondulatoire de schrödinger; une méthode générale de résolution par approximations successives," *Compt. Rend. Hebd. Seances Acad. Sci.*, vol. 183, pp. 24–26, 1926.

[102] H. A. Kramers, "Wellenmechanik und halbzahlige quantisierung," *Zeitschrift für Physik*, vol. 39, no. 10-11, pp. 828–840, 1926.

[103] D. Floryan and C. W. Rowley, "Distributed flexibility in inertial swimmers," *Journal of Fluid Mechanics*, vol. 888, 2020.

[104] A. Minikes, R. Gabay, I. Bucher, and M. Feldman, "On the sensing and tuning of progressive structural vibration waves," *IEEE transactions on ultrasonics, ferroelectrics, and frequency control*, vol. 52, no. 9, pp. 1565–1576, 2005.

[105] K. Deb, A. Pratap, S. Agarwal, and T. Meyarivan, "A fast and elitist multiobjective genetic algorithm: Nsga-ii," *IEEE transactions on evolutionary computation*, vol. 6, no. 2, pp. 182–197, 2002.

[106] F.-A. Fortin, F.-M. De Rainville, M.-A. Gardner, M. Parizeau, and C. Gagné, "DEAP: Evolutionary algorithms made easy," *Journal of Machine Learning Research*, vol. 13, pp. 2171–2175, 2012.